SYNTHESIS AND CHARACTERIZATION OF HYBRID NANOCOMPOSITES USING POLYVINYLCARBAZOLE AND METAL SELENIDES TO DEMONSTRATE PHOTOVOLTAIC PROPERTIES

A thesis submitted to the Faculty of Science, University of the Witwatersrand in partial fulfilment of the requirement for the degree

Doctor of Philosophy (PhD) in Chemistry

By

STEFAN GOVINDRAJU

Student number:

0712070J

Signed by

_____on this_____ day of _____

Student: Mr S.J. Govindraju

Signed by

_____on this _____ day of _____

Supervisor: Prof N. Moloto

Co-Supervisors: Prof M.J. Moloto

Dr L.M. Sikhwivhilu

DECLARATION

I declare that this thesis, which is hereby submitted for a Doctor of Philosophy degree at the Faculty of Science, University of Witwatersrand Johannesburg is my own unaided work that has not been submitted for examination at any institution.

Signed by

Mr. S.J. Govindraju on this 01 day of June 2017

ABSTRACT

Due to a high global demand for energy, research groups have been focusing a lot of energy into finding alternative and cleaner energy sources. Solar power has all the attributes to be the energy of the future. Solar power is abundantly available and is a cleaner form of energy as compared to the market-leading fossil fuels.

In this thesis, we consider new materials that can be used in hybrid solar cells. These new materials combine the properties of inorganic nanomaterials and polymers. The nanomaterials possess unique properties that can be exploited and the polymers allow for the thin films to potentially be light weight and flexible.

Copper selenide was synthesized and characterized to produce particles with different sizes as a function of time. These size variations are shown to emit a spectrum of different colours. In addition the particles synthesized at various temperatures are reported. Temperature had an effect on the size of the particles with bigger sizes obtained as the temperature was increased. Also shown in the results is that Cu_2Se nanocrystals were quite resistant to changes with the sizes marginally increasing with increasing time and temperature. A hybrid material using a conductive polymer polyvinylcarbazole (PVK) and copper selenide was synthesized and used as the active layer via a spin coating technique to fabricate a solar cell. Varying amounts (10% - 50%) of Cu_2Se nanocrystals were used in the polymer nanocomposites. The 10% weight loading resulted in the highest efficiency of 0.74% whilst successive addition of the nanocrystals affected the polymeric structure of PVK thus resulting in solar cells with even lower efficiencies.

Niobium selenide was synthesized via the colloidal method using TOP/HDA combination for the first time. The effect of time on the particles synthesized using a 1:1 mole ratio of Nb:Se was negligible with particles showing similar properties. The XRD of the samples revealed that they were amorphous thus making it difficult to conclusively say that niobium selenide was synthesized successfully. The samples were then annealed however only small improvements were observed. The concentration of the selenium was then increased in order to form the more common $NbSe_2$ and $NbSe_3$. The XRD showed the formation of $NbSe_2$ and $NbSe_3$ for 1:2 and 1:3 Nb:Se ratios respectively. In addition, the particles resembled 2D nanostructures readily observed in layered materials such as $NbSe_2$ and $NbSe_3$. However, some impurities in the form of oxides were still observed. Hybrid solar cells prepared from the amorphous 1:1, 1:2 and 1:3 Nb:Se samples were fabricated. The $NbSe_3$ composite had the best performing solar cell with the power conversion efficiency of 3.234% with the amorphous particles generating no current.

DEDICATION

TO MY PARENTS:

SAMUEL AND ROSEMARY GOVINDRAJU

AND MY GRANDPARENTS

WHO HAVE SACRIFICED IN THEIR PAST

TO GIVE ME THIS PRESENT

ACKNOWLEDGEMENTS

- I would like to thank my supervisor Prof N. Moloto for everything that she has helped me achieve under her guidance over these past years. Without Prof Moloto's belief in my abilities I would not be in the position that I am in today. I cannot thank her enough for the opportunity that she has given me and I will be forever grateful.
- Thanks also go to my co-supervisors for their support in the background.
- To my fellow group members of the solar group I would like to thank everyone for their help during this project. We started off as individual students but by the end we all have ended up being friends.
- I would like to thank the School of Chemistry, the CATOMAT group and the University of the Witwatersrand.
- I would like to acknowledge the Wits Microscopy Unit. A special thanks goes to Prof Alexander Ziegler and his team for the assistance that they have given and the opportunity to use these microscopes.
- With the funding from the NRF, MERG, MINTEK, ESKOM, THRIP and the faculty of Science this project would not have been possible therefore immense amount of credit needs to go to these organisations.
- Thanks goes to Mr. Rob Steward for giving me a second chance at my academics back when I was in first year. At that time, he was the Deputy Dean in the Faculty of science.
- And finally, thanks to my family, my fiancé Dhe and friends for their support over the years.

PRESENTATIONS

- Erice energy summer school (Italy) 2016.
- Oral: **Novel semiconductor nanocrystals for third generation solar cells** -MERG (Materials and Energy Research Group) 2014 Gauteng, Parais.
- Oral: **Effects of Cu_xSe_y on polymer material for the use in solar cells**- SANI Nano Africa 2014 VUT (Vaal University of Technology) Gauteng, Vaal.
- Poster: **Synthesis and characterisation of electrochromic $CuSe_2$ and $CuSe_2$/PVK polymer nanocomposites for application in solar cells** – SACI (South African Chemical Institution) Inorganic Chemistry 2013 Kwa-Zulu Natal, Durban.
- Oral: **Synthesis and characterisation of electrochromic Cu_xSe_y and synthesise of conductive polymer nanocomposites for the application in bulk heterojunction solar cells** – IBSA (India Brazil South Africa) 2013 Gauteng, Pretoria.
- Oral: **Synthesis and characterisation of CuSe hybrid nanostructures** – SANI (South African Nanotechnology initiative) 2012 NYRS (Nanotechnology Young Researchers Symposium) Gauteng, Johannesburg - 2nd place.
- Oral: **Synthesis and characterization of CdSe and CuSe/conductive polymer nanocomposites for application in bulk heterojunction solar cells** – IBSA 2012 Gauteng, Johannesburg.
- Poster: **Synthesis and characterization of CdSe and CdSe/PVK polymer nanocomposites for application in solar cells** – Nano Africa 2012 Free State, Bloemfontein.

PUBLICATIONS

[1] Synthesis and characterization of MnS and MnSe nanoparticles: Morphology, optical and magnetic properties; N. Moloto, M.J. Moloto, M. Kalenga, **S. Govindraju**, M. Airo; Optical Materials, 36(1) , **2013**, 31-35.

[2] Schottly solar cells: Anisotropic versus isotropic CuSe nanocrystals; N. Moloto, H. Puggens, **S. Govindraju**, B. Rakgalakane, M. Kalenga; Thin Solid Films, 531, **2013**, 446-450.

[3] Fabrication of a Schottly device using CuSe nanoparticels: Colloidal versus microwave digestive synthesis; M. Kalenga, **S. Govindraju**, M. Airo, M.J Moloto, L.M. Sikhwivhilu, N. Moloto; Journal of Nanoscience & Nanotechnology, 15 (6), **2015**, 4480-4486.

[4] Size quantization in Cu_2Se nanocrystals; **S. Govindraju**, M.P. Kalenga, M. Airo, M.J. Moloto, L.M. Sikhwivhilu, N. Moloto; Optical Materials, 38, **2014**, 310-313.

[5] Synthesis and characterization of indium monoselenide nanosheets: A proposed pseudo top-down mechanism; M. Airo, S. Gqoba, M.P. Kalenga, **S. Govindraju**, M.J. Moloto, N. Moloto; Journal of Crystal Growth, 406, **2014**, 1-7.

[6] Co-crystals and molecular salts of carboxylic acid/pyridine complexes: Can calculated *p*K_a's predict proton transfer? A case study of nine complexes; A. Lemmerer, **S. Govindraju**, M. Johnston, X. Motloung, K.L. Savig; Crystal Engineering Communication, 17, **2015**, 3591-3595.

[7] The effects of structural properties of Cu_2Se/Polyvinylcarbazole nanocomposites on the performance of hybrid solar cells; **S. Govindraju**, N. Ntholeng, K. Rangathan, M.J. Moloto, L.M. Sikhwivhilu, N. Moloto; Journal of Nanomaterials, 90, **2016**, 1-9**.**

[8] Colloidal synthesis of pure CuInTe2 crystallites based on the HSAB theory; N. Ntholeng, B. Mojela, S. Gqoba, M. Airo, **S. Govindraju**, M.J. Moloto, J. Van Wyk, N. Moloto, New Journal of Chemistry, 40, **2016**, 10259.

TABLE OF CONTENTS

DECLARATION iii

ABSTRACT iv

DEDICATION v

ACKNOWLEDGEMENTS vi

PRESENTATIONS vii

PUBLICATIONS viii

LIST OF FIGURES xiii

LIST OF TABLES xv

LIST OF ABBREVIATIONS xvi

SYNOPSIS 21

CHAPTER 1 23

GENERAL BACKGROUND 23

1.1 Introduction 23

1.2 Motivation and rationale of the study 27

1.3 Aims and objectives of the study 28

References 29

CHAPTER 2 30

LITERATURE REVIEW 30

2.1 Introduction 30

2.2 Semiconductor nanocrystals 33

2.3 Conductive polymers 46

2.4 Polymer nanocomposites 49

2.5 Principles and characterization of solar cells 52

2.6 Hybrid solar cells 54

References 59

CHAPTER 3 67

SIZE QUANTIZATION IN Cu_2Se NANOCRYSTALS 67

3.1 Introduction 67

3.2 Experimental section 70

3.2.1 Materials 70

3.2.2 Synthesis of the Cu_2Se nanocrystals 70

3.2.3 Instrumentation 71

3.3 Results and discussion 71

3.3.1 Size quantization in Cu_2Se nanocrystals 71

3.3.2 Effect of temperature on the properties of copper selenide 76

3.4 Conclusion 81

CHAPTER 4 85

THE EFFECT OF STRUCTURAL PROPERTIES OF Cu_2Se /POLYVINYLCARBAZOLE NANOCOMPOSITES ON THE PERFORMANCE OF HYBRID SOLAR CELLS 85

4.1 Introduction 85

4.2 Experimental section 87

4.2.1 Materials 87

4.2.2 Synthesis of the Cu_2Se nanocrystals 87

4.2.3 Synthesis of Cu_2Se/PVK nanocomposites 88

4.2.4 Fabrication of the hybrid solar cells 88

4.2.5 Instrumentation 89

4.3 Results and discussion 89

4.4 Conclusion 99

References.....100

CHAPTER 5 102

COLLOIDAL SYNTHESIS AND CHARACTERIZATION OF AMORPHOUS NIOBIUM SELENIDE 102

5.1 Introduction.....102

5.2 Experimental section 104

5.2.1 Materials 104

5.2.2 Synthesis of the niobium selenide particles 104

5.2.3 Instrumentation.....105

5.3. Results and discussion 106

5.3.1 Effect of time on the properties of niobium selenide 106

3.2 Annealing to improve crystallinity of niobium selenide.....113

3.3 Effect of increasing the selenium concentration on the properties of niobium selenide.....120

5.4 Conclusion 125

References.....125

CHAPTER 6 128

SYNTHESIS AND CHARACTERIZATION OF NIOBIUM SELENIDE/POLYVINYLCARBAZOLE NANOCOMPOSITES AND THEIR USE AS ACTIVE LAYERS IN HYBRID SOLAR CELLS 128

6.1 Introduction.....128

6.2 Experimental Section.....130

6.2.1 Materials 130

6.2.2 Synthesis of niobium selenide/PVK nanocomposites.....130

6.2.3 Fabrication of the hybrid solar cells.....131

6.2.4 Instrumentation.....131

6.3 Results and discussion 132

6.4 Conclusion 142

References.....143

CHAPTER 7 146

CONCLUSION AND RECOMMENDATIONS 146

7.1 Conclusion 146

7.1.1 Synthesis and characteristic of copper selenide nanocrystals and copper selenide nanocomposites 146

7.1.2 Synthesis and characterization of niobium selenide and niobium selenide nanocomposites 147

7.1.3 Fabrication of solar devices using nanocomposites 148

7.2 Recommendations.....148

APPENDIX.....150

LIST OF FIGURES

Fig. 1.1: Global values for annual solar irradiance. 25

Fig. 2.1: Global PV market in 2015. 31

Fig. 2.2: Discretization of density of states due to quantum confinement. 34

Fig. 2.3: Tunable band gap and absorption. 35

Fig. 2.4: UV-Vis absorption and photoluminescence spectra of CdSe showing the size quantization effect [25]. 37

Fig. 2.5: Intra-band relaxation [29]. 38

Fig. 2.6: Radiative recombination. 39

Fig. 2.4: Multiple exciton generation in semiconductor nanocrystals. 41

Fig. 2.8: Hot carrier extraction. 42

Fig. 2.9: Lamer and Dinegar growth mechanism. 44

Fig. 2.10: Nanocrystal phase behaviour in polymeric matrix. 50

Fig. 2.11: Grafting-to and grafting-from synthesis of polymer nanocomposites. 51

Fig. 2.12: Basic structure of a solar cell. 53

Fig. 2.13: I-V curve showing the important parameters. 54

Fig. 2.14: Active layer architecture in OPVs. 56

Fig. 2.15: Mechanism of a BHJ solar cell. 57

Fig. 3.1: Stoichiometry and space group of copper-selenium. 68

Fig. 3.2: Phase diagram of copper-selenium. 69

Fig. 3.3.: Size quantization effect in Cu_2Se nanocrystals depicted by the change in colour with an increase in time, A being an aliquot at 2 min through to H and aliquot at 60 min. 72

Fig. 3.4: UV-Vis absorption and photoluminescence of spectra of samples A, C, E and H. 73

Fig. 3.5: PXRD patterns of samples A to H. 75

Fig. 3.6: TEM images of samples A to H. 76

Fig. 3.7: UV-Vis absorption and photoluminescence spectra of copper selenide nanocrystals synthesized at different temperatures.....77

Fig. 3.8: X-ray diffraction of copper selenide nanocrystals synthesized at different temperatures where * signifies Se. 79

Fig. 3.9: TEM images of copper selenide nanocrystals synthesized at different temperatures. 80

Fig. 3.10: Size distribution plots of copper selenide nanocrystals synthesized at different temperatures. 81

Fig. 4.1: (a) TEM micrograph of Cu_2Se nanoparticles and (b) SEM micrograph of PVK, (c) SEM micrograph of 10% Cu_2Se/PVK nanocomposite (d) SEM micrograph of 50% Cu_2Se/PVK nanocomposite, (e) TEM micrograph of 10% Cu_2Se/PVK nanocomposite and (f) TEM micrograph of 50% Cu_2Se/PVK nanocomposite. 91

Fig. 4.2: (a) EDX spectrum of PVK, (b) 10% Cu_2Se/PVK nanocomposite and (c) 50% Cu_2Se/PVK nanocomposite. 92

Fig. 4.3: (a) FTIR spectrum of PVK, (b) 10% Cu_2Se/PVK nanocomposite and (c) 50% Cu_2Se/PVK nanocomposite. 93

Fig. 4.4: TGA curve of (a) PVK, (b) 10% Cu_2Se/PVK nanocomposite and (c) 50% Cu_2Se/PVK nanocomposite. 94

Fig. 4.5: UV-Vis absorption spectra and photoluminescence spectra with excitation at 300 nm for Cu_2Se, PVK, 10% Cu_2Se/PVK nanocomposite and 50% Cu_2Se/PVK nanocomposite.....96

Fig. 4.6: Selected peaks of (a) UV-Vis absorption and (b) photoluminescence spectra of 50% Cu_2Se/PVK nanocomposite. 97

Fig. 4.7: Device architecture and J-V curves of the 10, 20, 30 and 50% Cu_2Se/PVK nanocomposites in the dark and under illumination. 98

Fig. 5.1: Various compounds of niobium selenide. 103
Fig. 5.2: UV-Vis absorption and PL spectra of niobium selenide particles synthesized at (a) 45 min, (b) 60 min, (c) 75 min, (d) 90 min, (e) 105 min and (f) 120 min. 107
Fig. 5.3: XRD patterns of niobium selenide particles synthesized at (a) 45 min, (b) 60 min, (c) 75 min, (d) 90 min, (e) 105 min and (f) 120 min. 109
Fig. 5.4: SEM micrographs of niobium selenide particles synthesized at different times.....110
Fig. 5.5: TEM micrographs of niobium selenide particles synthesized at different times. ...112
Fig. 5.6: XRD patterns of (a) pristine niobium selenide synthesized at 45 min, (b) annealed 45 min sample at 700 °C for 60 min, (c) pristine niobium selenide synthesized at 105 min, and (d) annealed 105 min sample at 700 °C for 60 min. 114
Fig. 5.7: TGA spectra of (a) niobium selenide synthesized at 45 min and (b) niobium selenide synthesized at 105 min done in nitrogen atmosphere. 115
Fig. 5.8: SEM micrographs of the pristine and annealed niobium selenide particles synthesized at 45 min, 105 min and annealed at 700 °C for 60 min respectively. 117
Fig. 5.9: TEM micrographs of the pristine and annealed niobium selenide particles synthesized at 45 min, 105 min and annealed at 700 °C for 60 min respectively. 118
Fig. 5.10: UV-Vis absorption and PL spectra of the pristine and annealed niobium selenide particles, synthesized at (a) 45 min, (b) 105 min and annealed at 700 °C for 60 min (c) and (d) respectively. 119
Fig. 5.11: UV-Vis absorption and PL spectra of niobium selenide synthesized at different Nb:Se mole ratios, (a) 1:1, (b) 1:2 and (c) 1:3. 121
Fig. 5.12: XRD diffractograms of niobium selenide synthesized at different Nb:Se mole ratios, (a) 1:1, (b) 1:2 and (c) 1:3 where ♦ denotes Nb_2O_5. 122
Fig. 5.13: SEM micrograms of niobium selenide synthesized at different Nb:Se mole ratios, 1:1, 1:2 and 1:3. 123

Fig. 5.14: TEM micrograms of niobium selenide synthesized at different Nb:Se mole ratios, 1:1, 1:2 and 1:3. 124

Fig. 6.1: SEM micrographs of (a) amorphous $NbSe_y$ nanospheres, (b) $NbSe_2$, (c) $NbSe_3$ (d) amorphous $NbSe_y$/PVK nanocomposite, (e) $NbSe_2$/PVK nanocomposite and (f) $NbSe_3$/PVK nanocomposite. 133

Fig. 6.2: EDX spectra of (a) PVK, (b) amorphous $NbSe_y$/PVK nanocomposite, (c) $NbSe_2$/PVK nanocomposite and (d) $NbSe_3$/PVK nanocomposite. 135

Fig. 6.3: FTIR spectra of (a) PVK, (b) amorphous $NbSe_y$/PVK nanocomposite, (c) $NbSe_2$/PVK nanocomposite and (d) $NbSe_3$/PVK nanocomposite. 136

Fig. 6.4: TGA of (a) PVK, (b) amorphous $NbSe_y$/PVK nanocomposite, (c) $NbSe_2$/PVK nanocomposite and (d) $NbSe_3$/PVK nanocomposite. 137

Fig. 6.5: UV-Vis absorption and PL spectra of (a) PVK, (b) amorphous $NbSe_y$/PVK nanocomposite, (c) $NbSe_2$/PVK nanocomposite and (d) $NbSe_3$/PVK nanocomposite (excitation wavelength = 300 nm). 139

Fig. 6.6: Device architecture and band structure of the hybrid solar cell. 140

Fig. 6.7: J-V curves of (a) amorphous $NbSe_y$/PVK nanocomposite, (b) $NbSe_2$/PVK nanocomposite, (c) $NbSe_3$/PVK nanocomposite and the corresponding semi-log plot.....141

LIST OF TABLES

Table 2.2: List of common conductive polymer backbone [87] 47

Table 3.1: UV-Vis absorption band edges and emission maxima for samples A to H..... 74

Table 3.2: Summary of the optical properties of copper selenide particles synthesized at different temperatures 78

Table 4.1: Device properties of the nanocomposites 99

Table 5.1: Optical data for niobium selenide particles synthesized at 15 min intervals from 45 min to 120 min 108

Table 5.2: Summary of the TGA data 116

Table 6.1: Device properties of the nanocomposites 142

LIST OF ABBREVIATIONS

LCOE: Levelized cost of electricity

P3HT: Poly(3-hexylthiophene-2,5-diyl)

PVK: Polyvinylcarbazole

PV: Photovoltaic

DOS: Density of states

PL: Photoluminescence

MEG: Multi-exciton generation

HOMO: Highest occupied molecular orbitals

LUMO: Lowest occupied molecular orbitals

UV-Vis: Ultraviolet-visible

VRH: Variable range hopping

ATPR: Atom transfer radical polymerization

V_{OC}: Open circuit voltage

J_{SC}: Short circuit current

FF: Fill factor

Pmax: Maximum power

OPV: Organic photovoltaic

PCBM: [6,6]-phenyl C61-butyric acid methyl ester

BHJ: Bulk heterojunction

D-A: Donor-acceptor

PCP-DTBT: [2, 6-(4,4-bis-(2-ethylhexyl)-4H-cyclopenta[2, 1-*b*; 3, 4-*b*']dithiophene)-*alt*-4, 7-(2, 1, 3-benzothiadiazole)]

PCE: Power conversion efficiency

EQE: External quantum efficiency

AM: Air mass

TOP: Trioctylphosphine

HDA: Hexadecylamine

XRD: X-ray diffraction

TEM: Transmission electron microscopy

JCPDS: Joint committee on powder diffraction standards

FWHM: Full width half maximum

PEDOT-PSS: (poly(3,4-ethylenedioxythiophene):poly(styrenesulfonate)

EDX: Energy dispersive X-ray

FTIR: Fourier transformed infrared

SEM: Scanning electron microscopy

TGA: Thermogravimetric analysis

1D: One dimension

2D: Two dimension

ITO: Indium tin oxide

J-V: Current density-voltage

SYNOPSIS

The aim of the study was to synthesize copper and niobium selenide semiconductor nanocrystals and incorporate them into a conductive polymer to form polymer nanocomposites. The polymer nanocomposites were to then be used to demonstrate their application as active layers in hybrid solar cells. The thesis is therefore presented in the format below:

Chapter 1: is the general background, motivation and rational for the study as well as aims and objectives.

Chapter 2: is the literature review of semiconductor nanocrystals, conductive polymers, polymer nanocomposites, operation and characterization of solar cells and application of polymer nanocomposites in hybrid solar cells.

Chapter 3: reports on the synthesis and characterization of copper selenide nanocrystals

Chapter 4: reports on the synthesis of copper selenide/polyvinlycarbazole nanocomposites and demonstrates their application in hybrid solar cells

Chapter 5: reports on the synthesis and characterization of niobium selenide nanocrystals

Chapter 6: reports on the synthesis of niobium selenide/polyvinlycarbazole nanocomposites and demonstrates their application hybrid solar cells

Chapter 7: critically looks at the conclusions and suggests possible future studies

CHAPTER 1

GENERAL BACKGROUND

1.1 Introduction

Energy is one of the most priced commodities today. Energy production and consumption has had a significant impact on the world's development, political spheres, the environment as well as international relations. It has been established that the Millennium Development Goals are not achievable without access to sufficient energy. Although energy is a catalyst and stimulant for growth in every country, regrettably it has been ignored as a development strategy by most African governments. Africa's impeded economic development; political instability and exacerbated poverty are a direct repercussion of the energy challenges. Africa's population of about 1 billion people (one sixth of the world's population) is estimated to use a mere 4% of global electricity [1]. Most African countries continue to struggle to build their infrastructure leaving masses of people with no means and access to clean, safe and convenient energy. It is therefore apparent that the current energy demands of Africa far outstrip the production capacities.

Africa derives most of its energy from the burning of biomass such as wood and animal waste [2], with an exception of North Africa and South Africa which are largely dependent on oil and gas (North Africa) and coal (South Africa) [3]. Utilization of biomass alone cannot meet the energy demands of Africa. Fossil fuels such as petroleum and coal cannot be a viable option for Africa as these resources have depleting reserves and environmental implications. The steady decline of these resources results in increased global competitiveness which inevitably results in high cost. Petroleum and coal can also have serious implications for the environment.

Oil exploration and coal mining can have a negative impact on the people, wildlife and the general environment. More and more oil spills have been occurring causing vast damage and deaths on the marine wildlife and environment. Acid mine drainage, interference with the underground water levels and the water table as well as the impact on land use are some examples of the effect of coal mining. Furthermore, these sources should undergo the combustion process to produce useable energy. The combustion process usually produces waste products due to impurities, especially particulates and various gases. These gases are collectively known as greenhouse gases and they are the primary cause of the greenhouse effect. The greenhouse effect result in global warming which in turn can result in climate changes. New cost effective, clean and sustainable sources of electricity are therefore imperative.

Africa is indeed a home to the world's poorest and least developed countries yet Africa as a continent is far from poor, that is in terms of resources. Africa is rich in renewable resources that could drive its development. From the dozens of rivers and tributaries that could run micro-hydro systems to geothermal heat within its rift valleys; there is wind to be harvested on all its coasts, to the tons of bio-waste that could be digested and utilized as well as miles and miles of desserts and semi-arid areas with some of the world's most potent solar radiation that is enough to meet the entire world's energy needs. Given the lack of infrastructure for the traditional energy generation methods and the abundance of renewable resources, Africa can therefore surge forward by looking at new models for generating energy.

The use of solar radiation for energy therefore becomes quite an attractive alternative. Large parts of Africa, as shown in Fig. 1.1 receive good amount of solar radiation and hence this can be utilized in the form of energy producing technologies such as photovoltaics. While this is a

viable technology, several advantages and disadvantages of implementing this technology exist.

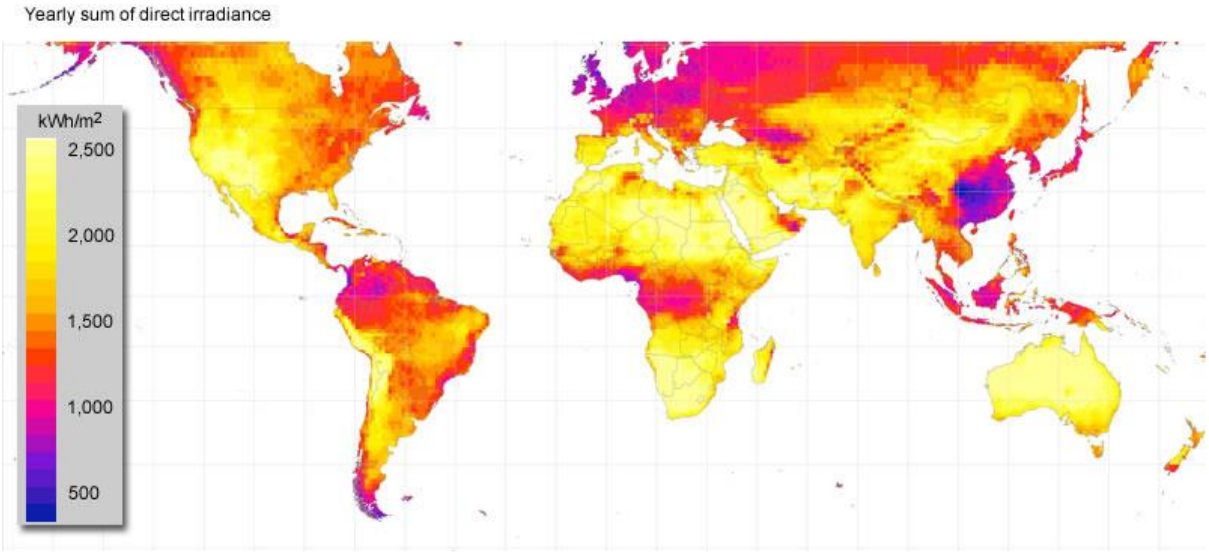

Fig. 1.1: Global values for annual solar irradiance.

In electrical power generation, the distinct ways in which electricity is generated incurs different costs. Calculations of these costs at the point of connection to a load or to the electricity grid can be made. The cost is typically given per kilowatt-hour or megawatt-hour. It includes the initial capital, discount rate, as well as the costs of continuous operation, fuel, and maintenance [4]. These types of costs can be calculated for each technology and a comparative study can be made. There are a number of costs factors that can be considered in accessing the overall costs of the technology such as capital costs, waste disposal costs and etc. These can be summed up into a calculation known as the leveled cost of electricity (LCOE). The LCOE is given by the following equation 1 [5]:

$$LCOE = \frac{Sum\ of\ costs\ over\ \ lifetime}{Sum\ of\ electrical\ energy\ produced\ over\ lifetime} = \sum_{t=1}^{n} \frac{\frac{I_t + M_t + F_t}{(1+r)^t}}{\frac{E_t}{(1+r)^t}} \qquad \text{(eq. 1.1)}$$

Where,

I_t: investment expenditures in the year t

M_t: operations and maintenance expenditures in the year t

F_t: fuel expenditures in the year t

E_t: electrical energy generated in the year t

r: discount rate

n: expected lifetime of system or power station.

There are flaws to the LCOE calculation and a number of other modifications have been proposed [6]. Nevertheless, the costs of electricity generated from fossil fuels are lower than for renewable energy technologies including photovoltaics [7]. This is due primarily to the low power conversion efficiency of photovoltaics that is their ability of converting solar energy from the sun into usable electricity. Apart from the cost, photovoltaics offer a number of advantages such as the use of non-depleting energy source, the impact on the environment and most importantly for Africa, the reduced costs of infrastructural requirements. Photovoltaics can be installed in the form of power stations which are commonly referred to as solar parks or through localized usage such as individual building installation. The difference between solar parks and localized usage is that solar parks are designed for the supply of merchant power into the electricity grid and the power is supplied at the utility level. This choice therefore makes photovoltaics a viable option for Africa where depending on the location, the grid option or the localized installation can used. This will therefore ensure that the poorest of the poor and the most remote and disenfranchised people can have access to basic energy in the form of electrification.

1.2 Motivation and rationale of the study

Photovoltaics are grouped into three generations. The 1st generation is based on single crystalline silicon solar cells whilst the 2nd generation is based on thin film processing technology and has solar cells which comprised of materials such as amorphous silicon, cadmium telluride and copper indium gallium selenide. The 3rd generation of solar cells which is currently under intensive research, is based on emerging technologies and encompasses inorganic nanocrystal solar cells, organic solar cells, dye sensitized solar cells and so on. The 1st generation solar cells have the highest power conversion efficiency for a single-layer device and have the highest market footprint in the photovoltaic commercial industry, however due to the high cost of production; this technology has had very little impact on the overall energy market. Consequently the 2nd generation cells were made. These utilizes a cheaper processing technology and materials; however these materials have produced less efficient devices resulting in the overall cost of the panels to be as expensive as the 1st generation silicon based panels.

Hybrid solar cells are a modification of the 3rd generation organic solar cells (bulk heterojunction solar cells). Bulk heterojunction solar cells comprise of an organic conductive polymer typically polyhexylthiophene (P3HT) as an electron donor, in a blend with fullerenes that act as electron acceptors. These devices while they have an advantage of being cost effective as they can be fabricated through solution techniques and thus can be up-scaled through roll-to-roll and ink-jet fabrication techniques, they suffer from low efficiency, low stability and low strength. To combat some of these challenges, alternative materials to fullerenes should be explored. Herein, fullerenes are replaced by semiconductor nanocrystals. Semiconductor nanocrystals because of quantum confinement effect have been shown to have high absorption coefficients, tunable bandgaps and long excitation lifetime as well as capable

of generating multiple excitons. This therefore can potentially increase the efficiency of the organic solar cells. In addition, these materials are more stable than the fullerene counterparts.

1.3 Aims and objectives of the study

The aims of the study were therefore to find alternative materials to fullerenes. Herein, metal chalcogenide semiconductor nanocrystals were explored as electron acceptors in hybrid solar cells. These materials were synthesized and characterized to establish their properties. Polymer nanocomposites of conductive polyvinylcarbazole (PVK) (an alternative to P3HT as a cost measure) and metal selenides were also synthesized. The polymer nanocomposites were then demonstrated as possible candidates for application as active layers in hybrid solar cells. It is important to emphasize that full optimization of the solar cells was not undertaken as the aim was to merely demonstrate the application of these materials in hybrid solar cells.

Hence the following objectives were to be achieved:

- Synthesis, characterization and optimization of copper selenide nanocrystals
- Synthesis, characterization and optimization of copper selenide/PVK polymer nanocomposites
- Fabrication and characterization of copper selenide/PVK hybrid solar cells
- Synthesis, characterization and optimization of niobium selenide nanocrystals
- Synthesis, characterization and optimization of niobium selenide/PVK polymer nanocomposites
- Fabrication and characterization of niobium selenide/PVK hybrid solar cells

References

[1] N. Gronewold, Scientific American, 24, **2009**.

[2] AFREPEN, 2001:1.

[3] S. Karekezi, Energy Policy, 30(11-12), **2002**, 1059-1069.

[4] A Review of Electricity Unit Cost Estimates Working Paper, December 2006 - Updated May 2007 Archived January 8, **2010**.

[5] Nuclear Energy Agency/International Energy Agency/Organization for Economic Cooperation and Development Projected Costs of Generating Electricity, **2005**.

[6] K. Branker, M.J.M Pathak, J.M. Pearce, Renewable and Sustainable Energy Reviews. 15 (9), **2011**, 4470–4482.

[7] P.L. Joskow, Comparing the Costs of Intermittent and Dispatchable Electricity-Generating, **2011**.

CHAPTER 2

LITERATURE REVIEW

2.1 Introduction

Energy is arguably the most important challenge facing the world today. Most of the world's major problems such as poverty, food security, climate change, wars etc. are directly influenced by energy. Traditional energy sources such as fossil fuels are today still available in abundance however this will not be the case forever as they are non-renewable. In addition, they pose an environmental threat. The push is therefore for renewable energy and solar being one of the most viable options. Nanotechnology is the ground-breaking technology of the 21st century that has made it possible to improve on existing technologies and to pursue new ones. The application of nanotechnology in the energy sector, particularly in photovoltaics has opened a door to offer electrification solutions to the least developed places with marginal cost implications.

The photovoltaic (PV) market has evolved over time from an expensive niche market in the 1990s to the recent large scale deployment and competitiveness. The photovoltaic market has seen year on year growth in terms of installations, for example 50.7 GW additional global installed capacity was seen in 2015 as compared to 2014, marking a 26.5% growth [1]. The global distribution of the approximately 51 GW installed PV systems is shown in Fig. 2.1. Evident from the statistics is that Africa though having the best solar irradiance over large areas of land has little or no representation over the PV market.

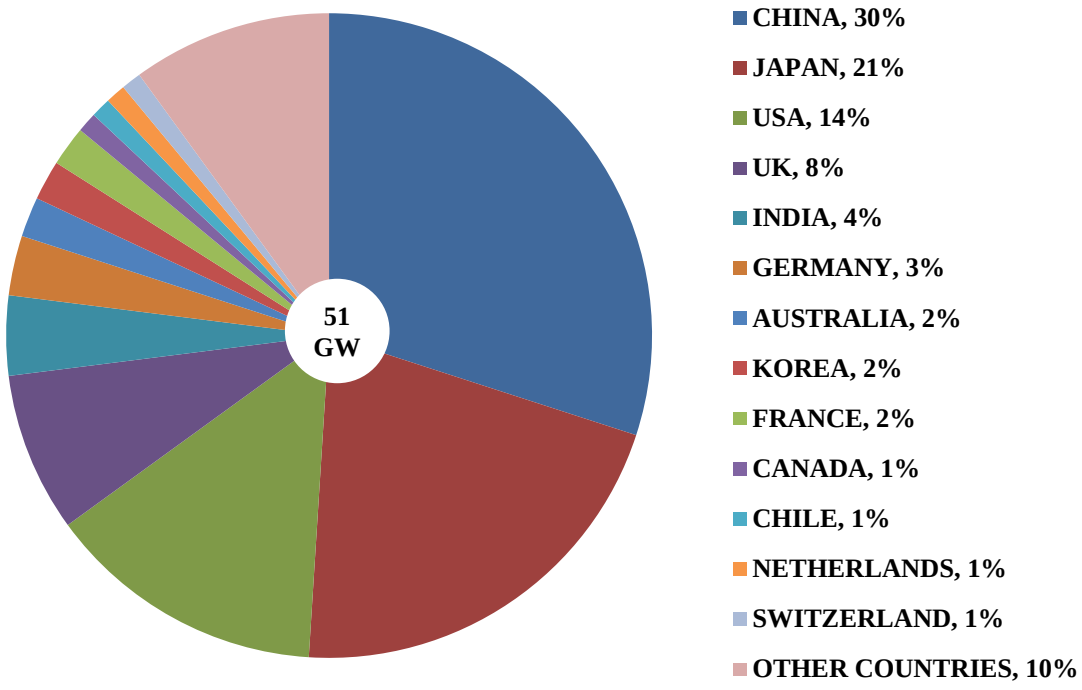

Fig. 2.1: Global PV market in 2015.

Nevertheless, there are small strides made by Africa, in particular South Africa. Table 1.1 shows the evolution of top 10 PV markets over a period of three years. The only African country featuring in the top 10 over this period is South Africa. South Africa has been engaged in a number of programs aimed at increasing their PV installations such as the Jasper Solar Energy Project which is a 96 MW power station located in Kimberly and a number of others projected for the future [2]. The South African government through the Department of Energy has a policy in place regarding renewable energy and they have stimulated the PV market through subsidizes like the other leading countries [3, 4].

Table 2.1: Evolution of TOP 10 PV markets

Ranking	2013	2014	2015
1	CHINA	CHINA	CHINA
2	JAPAN	JAPAN	JAPAN
3	USA	USA	USA
4	GERMANY	UK	UK
5	ITALY	GERMANY	INDIA
6	UK	FRANCE	GERMANY
7	ROMANIA	KOREA	AUSTRALIA
8	INDIA	AUSTRALIA	KOREA
9	GREECE	SOUTH AFRICA	FRANCE
10	AUSTRALIA	INDIA	CANADA
MARKET LEVEL TO ACCESS THE TOP 10			
	810 MW	779 MW	675 MW

While there are endeavours to use PV systems globally however the uptake and investment into PV is still relatively low compared to other electricity generating technologies. This is due to the high initial costs associated with PV systems hence forcing governments to partially subsidies the installations. This can however be circumvented by drastically reducing the price of the PVs. This can only be achieved by designing new systems that use cheaper materials, have low manufacturing costs and are highly efficient. This is where nanotechnology comes in. Nanotechnology has a potential of providing solutions of lowering the costs of PVs. Firstly, by using abundant and cheaper materials as well as using little amounts of materials. By reducing the size of materials from bulk to nanoscale; there is an increase in the surface area

thus allowing one to use less material. Secondly, by employing cheaper processing techniques; using nanoparticles in the manufacture of solar cells has the following benefits:

- reduced manufacturing costs because of using a low temperature process like printing instead of the high temperature vacuum deposition process typically used to produce conventional cells made with crystalline semiconductor material;
- reduced installation costs achieved by producing flexible rolls instead of rigid crystalline panels.

Cells made from semiconductor thin films will also have this characteristic. Employing nanotechnology can therefore help the realization of low cost solar cells with increased efficiency due to their unique properties.

2.2 Semiconductor nanocrystals

Semiconductor nanocrystals are promising candidates for photovoltaic applications. They are defined as crystalline structures composed of a few hundred to a few thousand atoms and have diameters ranging from 1 - 100 nm. Their importance in photovoltaic applications stems from the combination of superior optical and electronic properties. These properties are unique compared to their bulk materials due to quantum confinement effects. Quantum confinement can be observed once the diameter of a material is of the same magnitude as the de Broglie wavelength of the electron wave function [1]. Quantum confinement results in the discretization of energy states in semiconductors, consequently; a gradual reduction in the density of states (DOS) is experienced when transitioning from a bulk system to a quantum confined state.

The DOS is defined as the number of different states at a energy level that electrons are allowed to occupy, i.e. the number of electron states per unit volume per unit energy. Bulk properties

such as specific heat, paramagnetic susceptibility, and other transport phenomena of conductive solids depend on this function. DOS calculations can be used to determine the general distribution of states as a function of energy and can also determine the spacing between energy bands in semiconductors [2]. The DOS of semiconductors confined in different dimensions such as quantum wells, quantum wires and quantum dots can be calculated using a "particle in a box model" [3]. Using the Schrödinger wave equation, the DOS in the different dimensions can be solved.

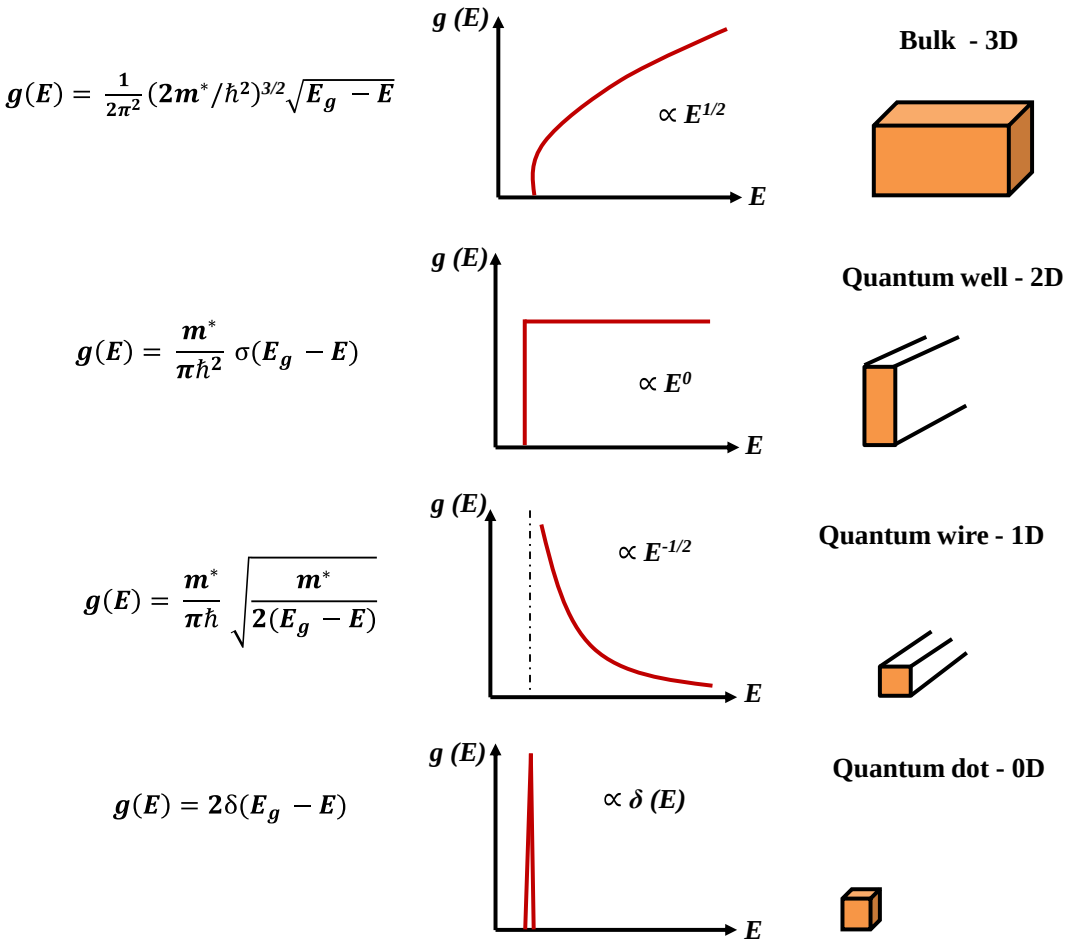

Fig. 2.2: Discretization of density of states due to quantum confinement.

Fig. 2.2 shows the DOS diagrams and solved equations for the different systems where Eg is the band gap energy, m* is the effective mass of the electron and $\hbar$ is the reduced Planck's constant [4]. Evident from the graph is that quantization of energy results in the discretization of the energy bands. The discretization of energy bands can result in interesting electronic properties in nanomaterials.

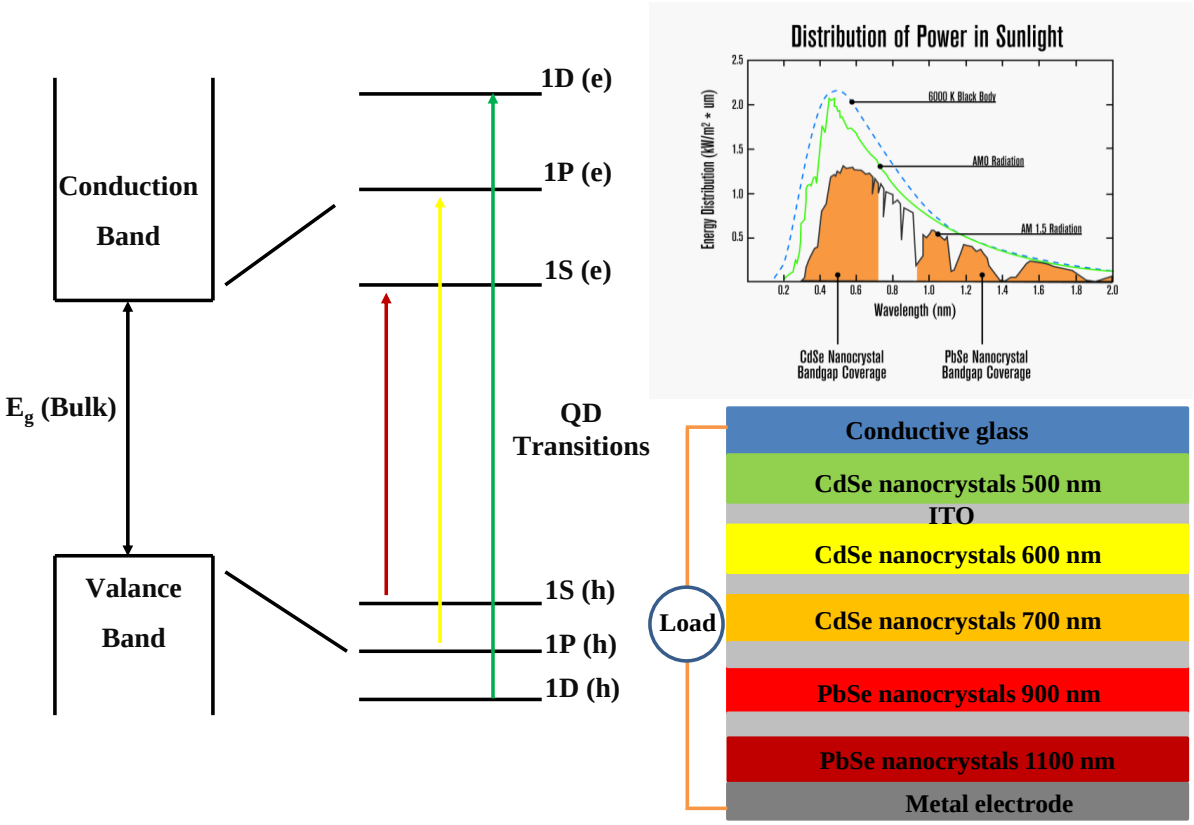

Fig. 2.3: Tunable band gap and absorption.

Understanding the electronic properties of semiconductor nanocrystals can aid one in designing solar cells that are more efficient. One of the defining features of semiconductor nanocrystals is the tuneable band gap, a property that has been widely investigated via optical spectroscopy and theoretical frameworks [5-8]. The electronic and consequently the optical properties of semiconductor nanocrystals can be determined by the absorption wavelength which is

characteristic of the band gap. This has been readily shown in quantum dots of group II-VI semiconductors such as CdSe, CdS and ZnSe [9-20]. Nanocrystalline materials that conserve the electronic wave function are called direct band gap materials while indirect band gap materials are those where the lowest electronic transition between valence band and conduction band is forbidden and they have very small absorption coefficients [21]. Upon absorption of a photon, an electron is promoted from the valence band to the conduction band thereby creating an electron-hole pair. A decrease in the size of the semiconductor nanocrystal such that it is comparable to or smaller than the Bohr exciton radius, result in quantum confinement effects and leads to atom-like optical behaviour in nanocrystals as the bulk bands become quantized as shown in Fig. 2.3. When nanocrystals are small compared to the Bohr exciton radius, their electronic wave functions experience three-dimensional quantum confinement. This results in the formation of quasiparticles due to the dot boundary. Consequently, both linear and nonlinear optical properties of small semiconductor nanocrystals arise as a result of transitions between electron and hole quantum-size levels. Thus, in a spherical nanocrystal (quantum dot) surrounded by an infinite potential barrier, the energy of the electron and hole quantum-size levels, characterized by angular momentum quantum number *l*, can be written in parabolic approximation as expressed in equation 2.1 [22-24];

$$E_{l,n}^{e,h} = \frac{\hbar^2 \phi_{l,n}^2}{2m_{e,h}a^2} \qquad \text{eq. (2.1)}$$

where $m_{e,h}$ is the electron and hole effective mass respectively, a is the crystal radius, $\Phi_{l,n}$ is the *n*th root of the spherical Bessel function. Based on equation 2.1, it is evident that the total energy of the optical band edge transitions will increase with a decrease in the size of the nanocrystal; as a result of quantized size levels of the electron and the hole. For example, model CdSe nanocrystals have been used to confirm this characteristic such that its energy can be tuned to cut across almost the whole optical spectrum. That is, their band gap energies can be

tuned from 1.8 eV, the bulk value, all the way to 3.0 eV simply by changing the size of the CdSe nanocrystal [25] as depicted in Fig. 2.4.

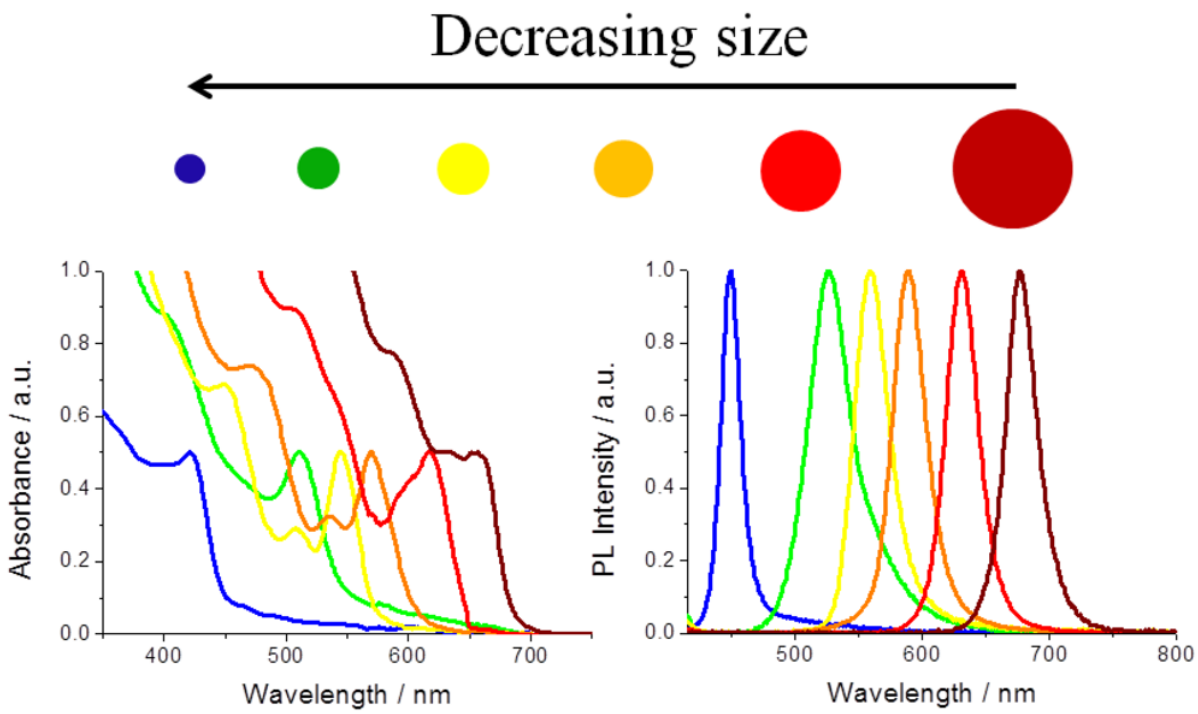

Fig. 2.4: UV-Vis absorption and photoluminescence spectra of CdSe showing the size quantization effect [25].

When a nanocrystal absorbs a photon of energy equal or larger than the band gap, an absorption spectrum can be measured. As a result of the quantum confinement effect, reducing the size of the semiconductor to the nanoscale size regime, results in a hypsochromic shift of the absorption onset, as shown in Fig. 2.4 [25]. A relatively sharp absorption feature near the absorption onset corresponds to the excitonic peak, i.e. the lowest excited state exhibiting large oscillator strength. Its position depends on the band-gap and, consequently, on the size of the nanoparticles, its form and width is strongly influenced by the size distribution, as well as the type and stoichiometry of the nanocrystals. Therefore, polydispersed samples typically exhibit only a shoulder in the absorption spectrum at the position of the excitonic transition [26].

Nanocrystals such as that of copper chalcogenides, show complicated spectra with the exciton peaks often not present [27]. Less pronounced absorption features in the shorter wavelength range correspond to excited states of higher energy [28]. As a rule of thumb, it can be asserted that the larger the number of such spectral features and the more distinctly they are resolved in the absorption spectrum, the smaller is the size dispersion of the sample. In solar cells, the tunable band gap property can therefore be potentially exploited to create solar cells with an active layer that absorbs in the entire visible to near infrared wavelengths of the solar spectrum as depicted in Fig. 2.3. This will of course increase the efficiency of the solar cells.

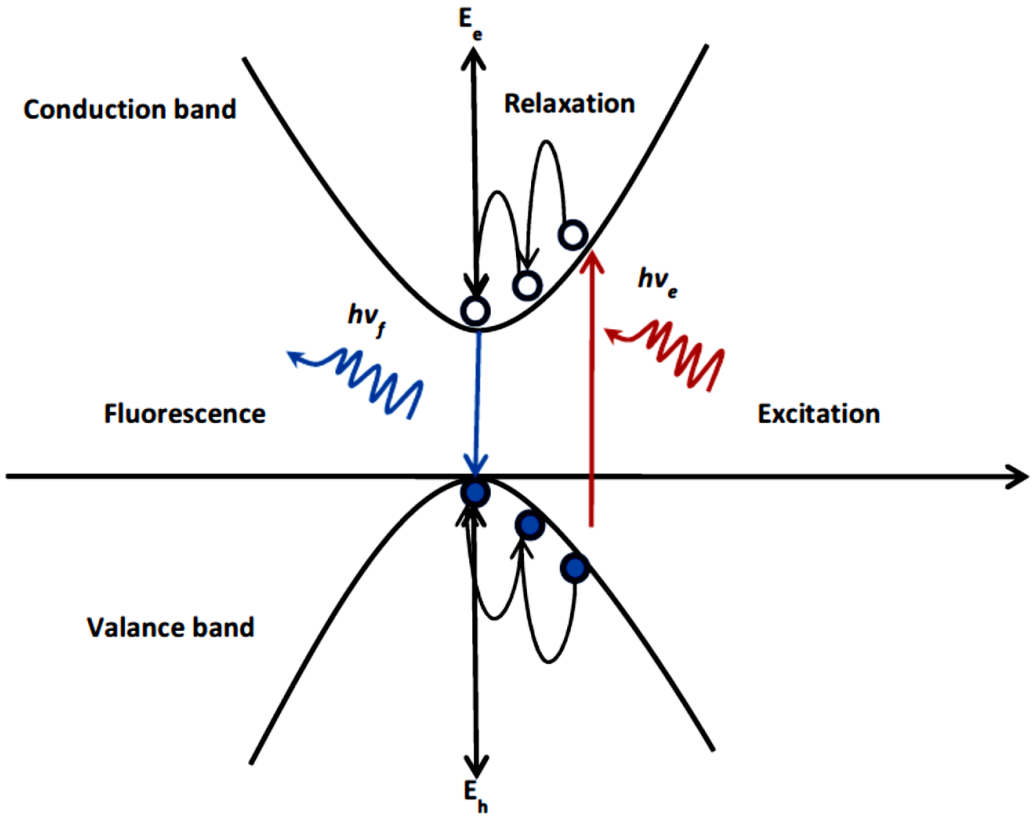

Fig. 2.5: Intra-band relaxation [29].

Photoluminescence spectroscopy is an important technique for examination of the size distribution, quality of semiconductor nanocrystals as well as excitation lifetimes. Typically,

when a semiconductor nanocrystal absorbs a photon with sufficiently larger energy than the band gap, an exciton is formed. The electron and the hole created then occupy the excited states above 1S in the discrete bands of the conduction and the valence band. In the event that a hot exciton is created, the very first process experienced is the exciton relaxation where the electron and the hole will quickly relax (<1 ps) to their ground states (the 1Se1Sh exciton) by means of a cascade of intra-band non-radiative relaxation steps, through which their excess energy will be lost as heat as shown in Fig. 2.5 [29].

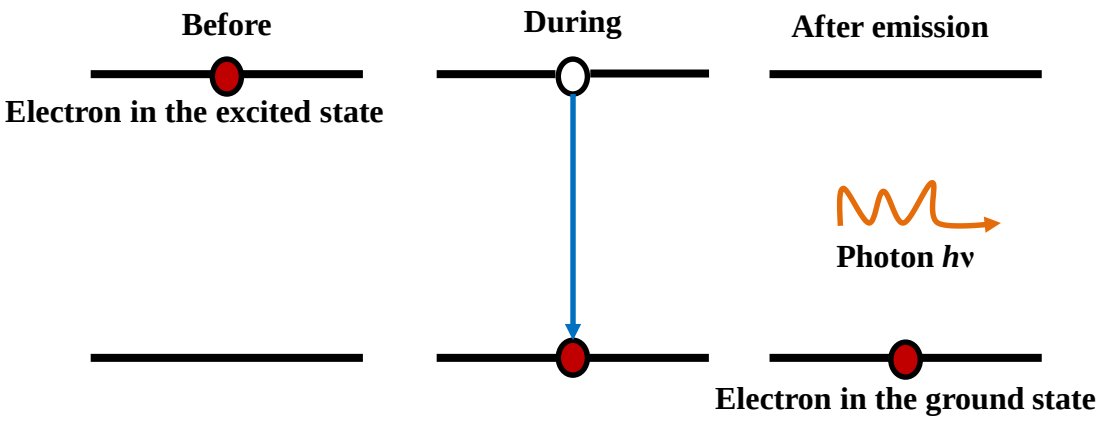

Fig. 2.6: Radiative recombination.

The second process is the electron-hole recombination which takes place after the exciton has reached its ground state (i.e., lowest energy 1Sh-1Se exciton) resulting into a further relaxation. During this process the excited electron returns to the valence band and the exciton energy is released radiatively which results into photoluminescence as shown in Fig. 2.6. Hence, photoluminescence (PL) is the emission of a photon due to exciton relaxation via radiative recombination. A well-defined emission peak in a PL spectrum with a small Stokes Shift relative to the band gap corresponds to the direct recombination of the exciton. This implies that the emitted photons have energies corresponding to the band gap of the nanocrystals and

as such PL spectroscopy presents the same size dependent properties as the absorption spectra as shown in Fig, 2.4. The width of the PL peak (full width at half maximum) can also be indicative of the dispersity of the sample. Radiative recombination can also occur when charge carriers are trapped in a defect or surface state. The resulting emission is known as defect PL or trap PL, and is characterized by a very broad emission band that is blue-shifted from the absorption band gap [30-31]. Trapping of the charge carriers in defect or surface states or impurities can also result in non-radiative recombination through which the exciton energy is fully dissipated as heat in the crystal lattice. Surface stares become more prevalent as the size of the nanocrystal decreases. This is due to the presence of vacancies and dangling bonds on the surface of the nanocrystal. This can however be circumvented by passivating the surface by using organic ligands as surfactants. The surfactants can therefore help to tune the emission properties [32-37].

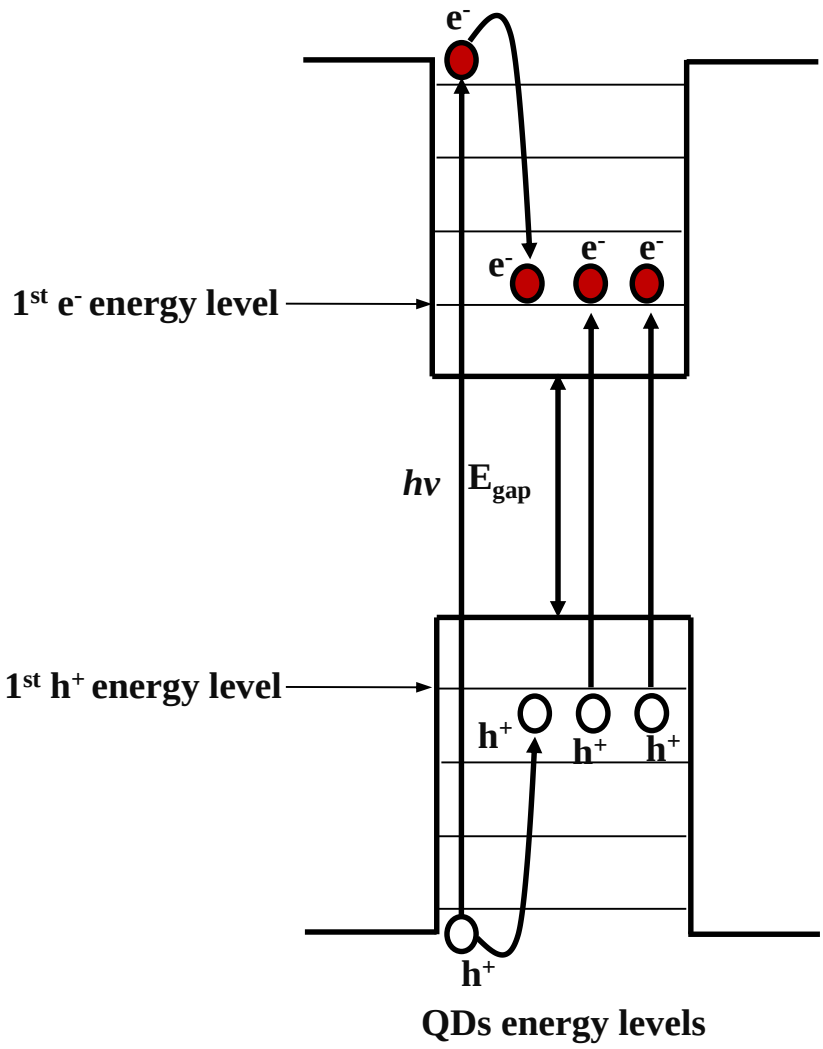

Fig. 2.4: Multiple exciton generation in semiconductor nanocrystals.

In photovoltaic research, carrier multiplication is a welcomed phenomenon and can potentially result in an increase in efficiency. This phenomenon occurs when absorption of a single photon of energy leads to the creation of multiple excitons. In conventional solar cells such as mono crystalline silicon, each photon is only able to excite one electron across the band gap of the semiconductor, and any excess energy in that photon is dissipated as heat. In a material with multiple exciton generation (MEG), high-energy photons excite on average more than one electron across the band gap as shown in Fig. 2.7, and so in principle the solar cell can produce more useful work. The mechanism of MEG is still under intense debate and a number of

theories have been suggested however recently there has been a consensus that MEG occurs through impact ionization [38-42].

Light excites a high-energy exciton which decays irreversibly into a quasi-continuum of multi-exciton states available at this energy. The model requires only the density of states of multi-excitons to be very high, while the Coulomb coupling between X and multi-X can be quite small [43]. MEG has been shown in PbSe, PbS, PbTe, CdS, CdSe, InAs, Si and InP nanocrystals [44-55]. Nevertheless, in order for MEG to have a large impact on solar energy conversion, the design of the solar cell must be able to fully exploit this property. Hence the requirements are (1) the nanocrystals must be the absorbing component, (2) the multi-excitons produced within the nanocrystals must be separated prior to Auger recombination, and (3) the free charge carriers or excitons must be transported to electron- and hole-accepting contacts. A further requirement is that the MEG efficiency must not be degraded when the nanocrystals are incorporated into solar cells [56].

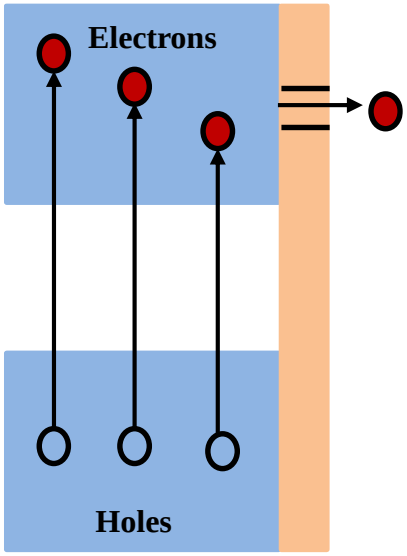

Fig. 2.8: Hot carrier extraction.

Another strategy that renders quantum dots good candidates for photovoltaics applications is their long excitation lifetimes. A major possibility for further improvement of photovoltaics lies in the efficient use of the excess energy of hot carriers. Such carriers are generated by photons whose energies considerably exceed the bandgap of the absorber and their excess energy is typically converted into heat. Harvesting this energy is highly challenging since thermalization of hot carriers typically takes place on a picosecond time scale or faster [57]. In photovoltaics, heat dissipation by hot carriers constitutes a major loss channel responsible for the Shockley–Queisser efficiency limit, and different strategies to resolve this problem are being explored [58, 59-62]. Quantum dots have excitation lifetimes in the order of nanoseconds and by employing selective electrodes the electrons can be extracted before cooling to the ground state as shown in Fig. 2.8.

Semiconductor nanocrystals have been synthesized using a variety of methods which can be roughly distinguished as ‘top down’ or ‘bottom up’ routes. Frankly, a majority of chemists are interested in the bottom up approach as it allows for synthesis in molecular scale, starting from precursors seen as building blocks, and all the way up to the final desired product. This allows for a variety of parameters to be manipulated and more importantly for a variety of routes to obtain the same product. Solution methods are therefore used and semiconductor nanocrystals are thus obtained as colloids. The formation of colloids in solution is generally described by the Lamer and Dinegar growth mechanism [63]. The model depicted in Fig. 2.9 suggests formation of nuclei from precursors which then self-react in order to grow and be more stable. These continue to grow as the reaction proceeds through Ostwald ripening until growth is terminated by stopping the reaction.

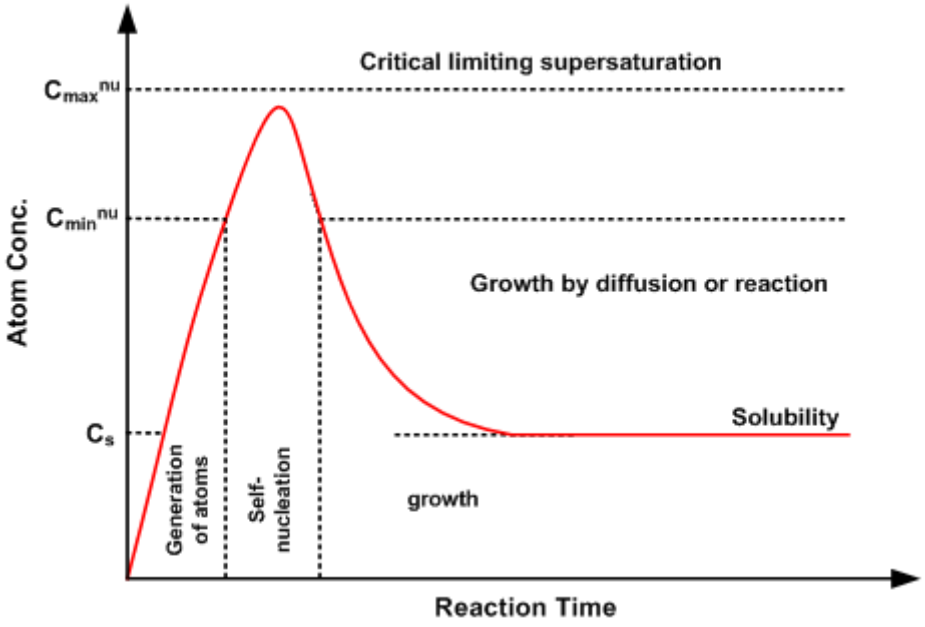

Fig. 2.9: Lamer and Dinegar growth mechanism.

A number of methods have been reported for the synthesis of colloidal semiconductor nanocrystals however the most popular ones are the solvothermal method and the reflux method that constitutes either the hot injection or heating up route. The solvothermal method involves the synthesis of nanomaterials in specific solvents, polar or non-polar at high temperatures and pressures in a sealed autoclave vessel [64-67]. While this method has an advantage of making materials in large quantities, it has disadvantages such as long reaction times, relatively harsh reaction conditions and expensive reaction vessels as well as production of more polydispersed samples. The reflux method is probably the most versatile method. First introduced by the Bawendi group where they synthesized TOP/TOPO capped CdE nanoparticles where E = S, Se and Te from bis(trimethysilyl)sulfide, selenium and telluride respectively and dimethylcadmium [68]. The method has since been modified, the use of dialkylmetal precursors were in particular found to be less desirable as they are toxic. O'Brien et al. introduced the use of single source precursors where they are not only less toxic but

provided an advantage of having the metal already bonded to the chalcogen [69]. Common to the two methods is that the precursors are injected at high temperatures into a hot coordinating solvent. The hot injection results in the burst of nucleation and consequently results in the production of nanocrystals with a narrow size distribution. A number of authors have reported in this type of synthesis for various types of metal chalcogenides [70-75].

The hot injection method does pose some difficulty and injection of precursors into hot solvents can be dangerous and this process can sometime prove to be inconsistent as it susceptible to human error. Thus, some researchers prefer the heating up method. The method is based on the concept of controlling the thermodynamics and the kinetics in the nanocrystal nucleation stage. Typically in a non-injection method, the separation of the nucleation and the growth is realized by slowly heating up the solution together with the precursors in one pot to a desired working temperature [76]. It has been shown that high quality colloidal nanocrystals are produced at relatively high temperatures (>200 °C). This therefore creates a major challenge for controlling the shape and size distribution because the temperature is increased over a broad range (e.g. from room temperature to over 200 °C). If the reactivity of a precursor is too high, this broad change of temperature often leads to concurrent nucleation and growth of nanocrystals in the reaction, which results in products that are polydispersed. However, if the precursors are too stable, a very small number of nuclei may form, which leads to uncontrollable particle growth. Therefore the precursors should meet the requirement that they have negligible reactivity at a low temperature, but significant reactivity at elevated temperatures [77, 78]. This method has been used to synthesize several high quality nanocrystals including CdSe, CdTe, PbSe, Ag_2S, Cu_2S, PbS and InSe [79-83].

2.3 Conductive polymers

Conventional polymers such as plastics, rubber etc. are usually highly resistant to electrical conductivity and are either dielectrics or insulators. With the discovery of polyacetylene in the 1970s, conductive polymers have received much attention from the scientific community. This culminated in the award of the Nobel Prize in 2000 to Heeger, MacDiarmid and Shirakawa for their discovery and development of electrically conductive polymers [84]. The unique characteristic of conducting polymers is the conjugated molecular structure of the polymer main chain where the π-electrons delocalize over the whole polymer chain. A few examples are shown in Table 2.1.

Conjugated polymers have delocalized π-electron structures, including the band structure of π-valence band and π*-conduction band. In the basic state of the intrinsic conjugated polymers, all the valence bands are filled by electrons and the conduction bands are all empty. The bandgap (E_g) of conjugated polymers is measured by the difference in energy of the highest occupied molecular level (HOMO) and the lowest unoccupied molecular level (LUMO), like other semiconductors. The E_g values of most conjugated polymers are in the range 1.5 – 3.0 eV hence they are referred to as organic semiconductors [85]. The E_g values of conjugated polymers can be measured by UV-Vis absorption spectroscopy of the conjugated polymer films. In solar cells, conductive polymers play an important role since their Eg values determine the absorption wavelength range of the devices, and the HOMO and LUMO energy levels influence the exciton dissociation efficiency at the donor/acceptor interface and the open circuit voltage of the solar cells [86]. Therefore, it is very important to understand the effect of the molecular structure on the energy bandgap and electronic energy levels of the conjugated polymers.

Table 2.2: List of common conductive polymer backbone [87]

	Heteroatoms present		
Chain type	**No heteroatoms**	**N containing**	**S containing**
Aromatic cycles	Poly(fluorene)s	**The N is in the aromatic cycle:**	**The S is in the aromatic cycle:**
	Poly(phenylene)s	Poly(pyrrole)s (PPY)	Poly(thiophene)s (PT)
	Poly(pyrene)s	Poly(carbazole)s	Poly(3,4-ethylenedioxythiophene) (PEDOT)
	Poly(azulene)s	Poly(indole)s	**The S is outside the aromatic cycle:**
	Poly(naphthalene)s	Poly(azepine)s	Poly(p-phenylene sulfide) (PPS)
		The N is outside the aromatic cycle:	
		Poly(aniline)s (PANI)	
Double bond	Poly(acetylene)s (PAC)		
Aromatic cycles and double bonds	Poly(p-phenylene vinylene) (PPV)		

Polarons are the major charge-carriers in conducting. The positive polaron with positive charge and the negative polaron with negative charge are denoted as P^+ and P^-, respectively. P^+ is formed after oxidation of the conjugated polymer main chain and P^- is formed after reduction of the conjugated polymer main chain. The appearance of the polarons produces two new polaron energy levels in the bandgap of the conjugated polymers. P^+ and P^- have spin quantum number of 1/2. The bipolaron is the charge carrier that possesses double charges by coupling of two P^+ or two P^- on a conjugated polymer main chain. The bipolaron has no spin, and it can be formed when the concentration of polarons are high in the conjugated polymer main chains. The positive bipolaron and negative bipolaron correspond to the hole pair or the electron pair [88].

Conductivity is the most important property of conducting polymers. The conductivity of common doped conducting polymers is in the range of 10^{-3} – 10^{3} S/cm, whereas that of the intrinsic conjugated polymers without doping is in the range of 10^{-9} – 10^{-6} S/cm. After doping, conductivity of conjugated polymers increases by six to nine folds. The highest conductivity reported in the literature is 10^{5} S/cm for drawing-extended ordering conducting polyacetylene film [89]. Conducting polymers usually have an amorphous structure, in some cases with ordered domains. The charge-transporting mechanism in conducting polymers is different from that in the crystalline conducting materials where there exist conduction bands and valence bands and the charge carriers can move freely in the energy bands. In conducting polymers, the charge carriers are located in the local doping energy levels (limited length of conjugated polymer chain) or in a very narrow doping energy band in the case of ordered domains. The charge carriers can move easily on the conjugated polymer main chain, but the charges have to hop for the transportation between the conjugated polymer chains. The activation energy for the hopping of the charge carriers is much higher than that of the charge transportation within

the conjugated polymer main chains. Therefore, the charge transportation in conducting polymers is limited by the hopping between the conjugated polymer chains [90]. Hence, the conductivity of conducting polymers shows characteristics of hopping transportation. The conductivity of conducting polymers shows temperature dependence like that of semiconductors, and it obeys the Mott Variable Range Hopping (VRH) model:

$$\sigma(T) = \sigma_0 \exp\left[-\left({T_0}/{T}\right)^{1/(n+1)}\right] \qquad \text{eq. (2.2)}$$

where σ_0 is a factor weakly related to temperature, n is the dimension number, n = 1, 2, 3 indicate that it is one-dimension, two–dimension, and three-dimension VRH transportation. For the common three-dimension system, the conductivity equation is [91],

$$\sigma(T) = \sigma_0{}^{3d} \exp\left[-\left({T_0}^{3d}/{T}\right)^{1/4}\right] \qquad \text{eq. (2.3)}$$

$${T_0}^{3d} = {c}/{[k_B N(E_F) L^3]} \qquad \text{eq. (2.4)}$$

where, c is a constant, k_B is the Boltzmann constant, L is the localization length (effective conjugated chain length), and $N(E_F)$ is the state density at the Fermi energy level.

2.4 Polymer nanocomposites

The integration of nanoparticles into polymers has been of significant interest to the scientific community for some time. Nano-sized fillers have been used for some time in conjunction with polymer materials, in an effort to enhance the properties relative to the polymers alone. Many

cases have been reported in the past where particles have been embedded in polymer matrices however the challenge still remains in obtaining a homogeneous blend [92]. Nanocrystals tend to behave in one of three ways when incorporated into polymer matrix, they can either aggregate, be dispersed throughout the matrix or form a self-assembled dispersion (Fig. 2.10). The latter two, being the most desirable. For a random dispersion of nanoparticles within a polymer film to be achieved, the particles must be compatible with the surrounding polymer matrix [93].

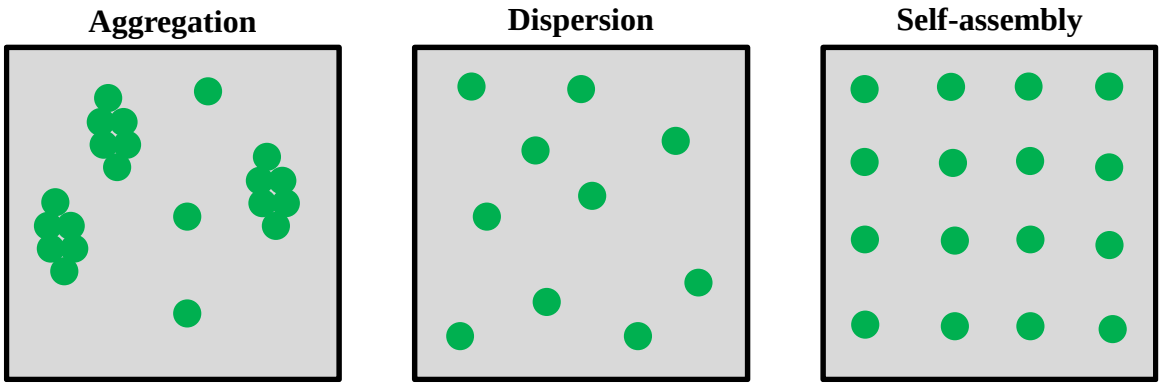

Fig. 2.10: Nanocrystal phase behaviour in polymeric matrix.

There are a number of strategies being employed to get the perfect blend in order to harness the properties. From dispersing the nanoparticles and polymer into a common solvent and blending at room temperature or elevated temperatures to the "graft-to" approach which attaches polymers to nanoparticles and the "graft-from" method, which focuses on polymerization from a nanoparticle surface [94-96]. Moloto et al. reported on the synthesis of MnS/polyvinylcarbazole nanocomposites using the solution blending approach at room temperature and 70 °C where minimal interaction between the nanoparticles and the polymer was observed although an improvement was seen with increased temperature [97]. Waldron and co-workers also reported on solution blending of PbSe and AB9093 epoxy polymer where

they reported on a reduced quantum yield from 55 % to 26 % due to the poor dispersity of the nanoparticles in the polymer matrix [98]. The typical graft-to approach is carried out by the attachment of polymers with ligand-functionalized chain-ends to nanoparticles through ligand exchange chemistry as shown in Fig. 2.11. The grafting density may be reduced due to steric shielding that arises upon placement of each successive polymer chain onto the nanoparticle. An example of this grafting-to method involves the ligand exchange of pyridine functionalized poly(ethylene glycol) (PEG) for TOPO on CdSe nanoparticles to afford a water soluble [99].

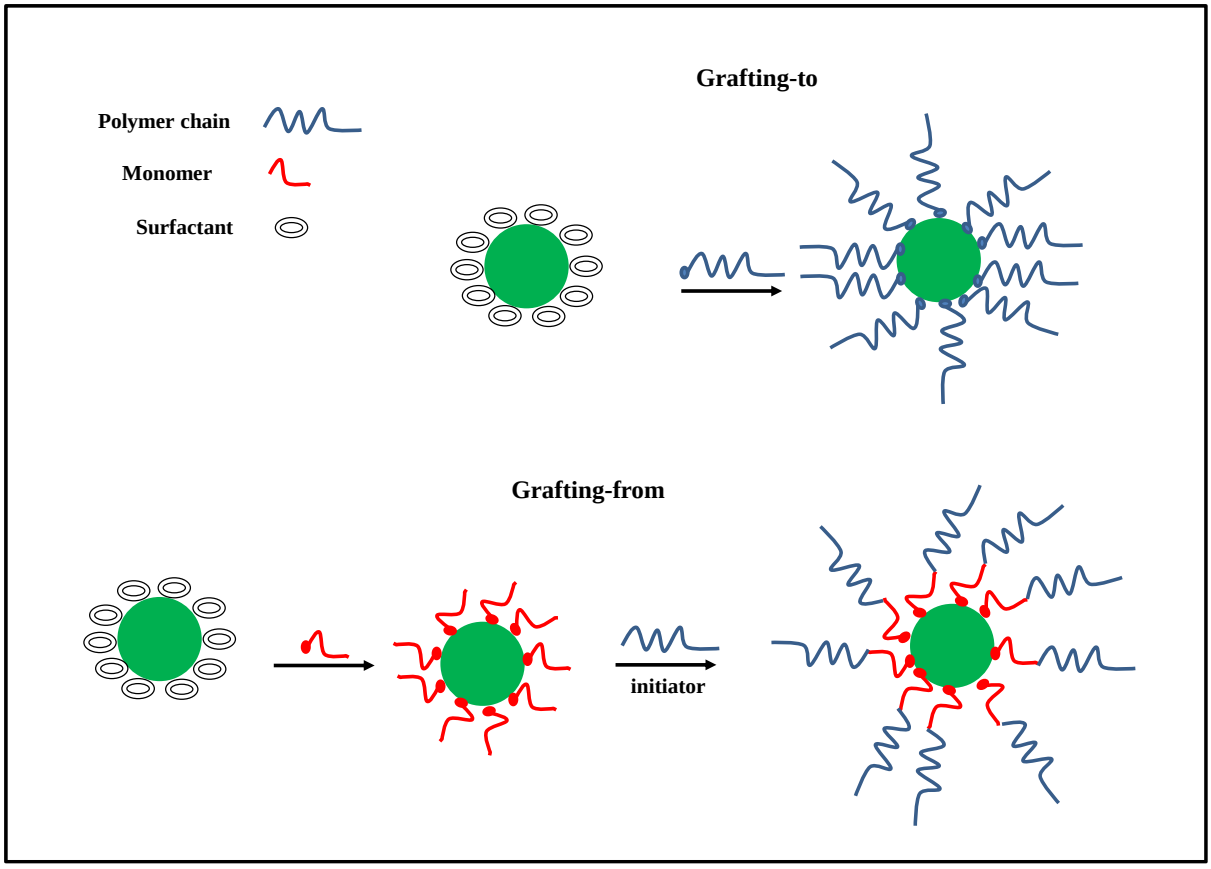

Fig. 2.11: Grafting-to and grafting-from synthesis of polymer nanocomposites.

The attachment of polymerization initiators to nanoparticle surfaces, followed by polymer growth outward from the surface, describes the "graft-from" technique. Critical to this "grafting-from" process is the compatibility of the nanoparticle with the polymerization conditions chosen, such that neither the attachment of functional ligands nor the polymerization

process appreciably alters the inherent properties of the nanoparticles [100]. This process is depicted in Fig. 2.11. The grafting of polymers from nanoparticles has been achieved by using an atom transfer radical polymerization (ATRP) process [101-103]. Wang et al. achieved the synthesis of well-defied organic/inorganic nanocomposite via reverse ATRP [104]. Polymer grafting onto a colloidal silica surface has been reported by Yoshinaga et al. [105]. In addition to grafting-to and from, in situ polymerization has been reported. This involves the addition of the nanoparticle precursors in the presence of the polymer matrix. Moloto et al. reported the formation of a core-shell like structure using this method where the polymer was thought to encapsulate the nanoparticles [106]. All the methods have advantages and disadvantages ranging from simplicity to high degree of difficulty to better interfacial interaction.

2.5 Principles and characterization of solar cells

Photovoltaic energy conversion consists of two important steps. First, the absorption of light generates an electron-hole pair. The electron and hole are then separated by the structure of the device, that is, electrons to the negative terminal and holes to the positive terminal, thus generating electrical power. This process is illustrated in Fig. 2.12, which shows the principal features of the typical solar cells in use today.

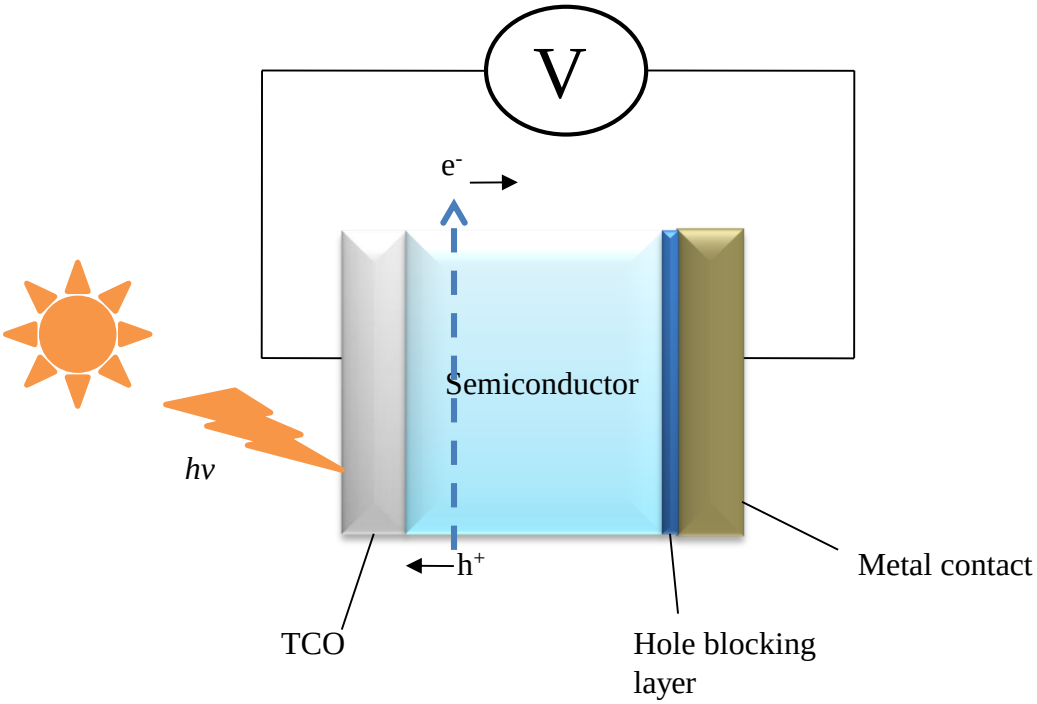

Fig. 2.12: Basic structure of a solar cell.

A solar cell is characterized by a current versus voltage measurement. This results in a curve shown in Fig. 2.13. From this graph, a few important performance parameters can be extracted, mainly the open circuit voltage (V_{OC}), short circuit current (J_{SC}), fill factor (FF), and maximum power (Pmax). Open circuit voltage is the voltage the cell produces when no current is flowing and represents the maximum voltage of the cell. The short circuit current is the current the cell can produce when the two electrodes are shorted together (i.e. V = 0).

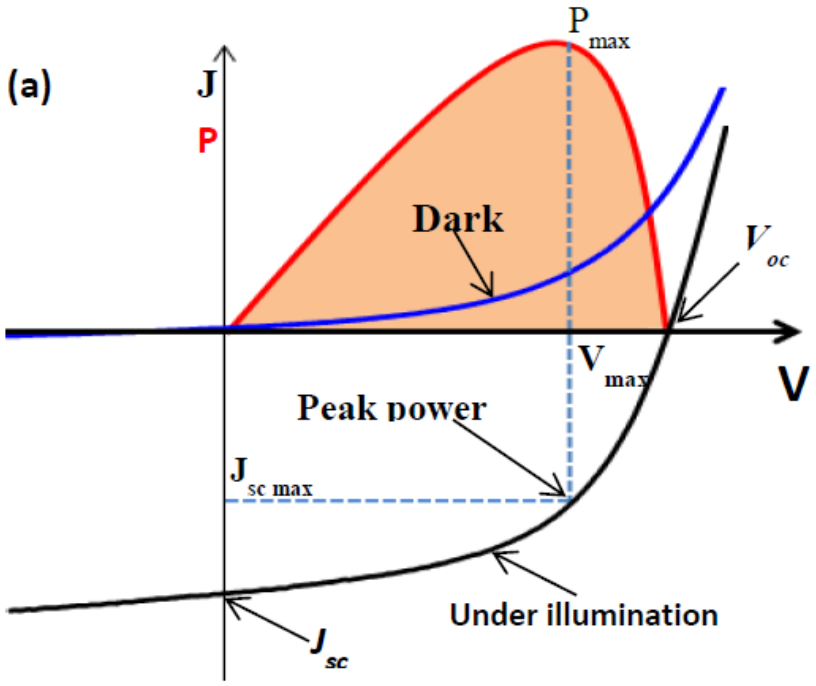

Fig. 2.13: I-V curve showing the important parameters.

Because power is the product of voltage and current, the point on the graph that forms the largest rectangle with the two axes represents the point of maximum power output. Fill factor is just the ratio of the actual maximum power to the ideal maximum power, that is:

$$FF = \frac{J_{max}V_{max}}{J_{sc}V_{oc}} \qquad \text{eq. (2.5)}$$

From this point, it is straightforward to get the power conversion efficiency, just divide the maximum power output by the power of the incident light:

$$\eta = \frac{P_{max}}{P_{in}} = \frac{J_{sc}V_{oc}FF}{P_{in}} \qquad \text{eq. (2.6)}$$

2.6 Hybrid solar cells

Organic photovoltaics (OPVs) are solar cells that use a combination of conjugated polymers such as poly(3-hexylthiophene-2,5-diyl) (P3HT) and [6,6]-phenyl C61-butyric acid methyl

ester (PCBM) as active layers for light absorption and charge transport in order to generate electricity from sunlight. While the external behaviour of organic photovoltaics is the same as that of inorganic PVs, the mechanism by which the voltage and current are generated is quite different [107]. The OPV material is not crystalline, so there are no nice bands for the electrons, nor is there an electric field to drive them. Because of that, when an excited electron is created by incident light it will quickly recombine with its hole unless something causes them to separate before recombination can happen. For that reason, OPVs consist of two materials, one that has an affinity for electrons and the other for holes. Once the electron and hole are separated into distinct materials, they can just diffuse apart due to their respective concentration gradients. Thus, there are three roles that will need to be fulfilled by the materials: absorption of light in the visible spectrum (if this is to be used in the sun), a semiconducting material that will take the electrons when excitons separate (the acceptor), and a semiconducting material that will take the holes (the donor) [108]. The conducting materials must be semiconductors so that the cell can maintain an output voltage and not just produce photoconductivity. If the charge carriers are generated far from the electrodes, the materials will also need to be efficient charge conductors (long carrier lifetimes) so that the charges are not lost before collection. Many material combinations have been tried that fit these requirements. They can be classified into three primary categories: molecular, polymer, and hybrid. The materials used in this thesis are an example of a hybrid OPV because they include an organic polymer as well as inorganic nanoparticles.

Because excitons will only separate into charge carriers at the interface of the two materials, it is desirable to maximize the interface surface area to volume ratio. This can be done by making very thin films of one material on top of the other, by mixing the two materials and forming what is known as a bulk heterojunction (BHJ), or by making some more complicated structure

that will maximize the junction surface area while maintaining a path for the charge carriers to get to the electrodes such as the vertically aligned BHJ as shown in Fig. 2.14.

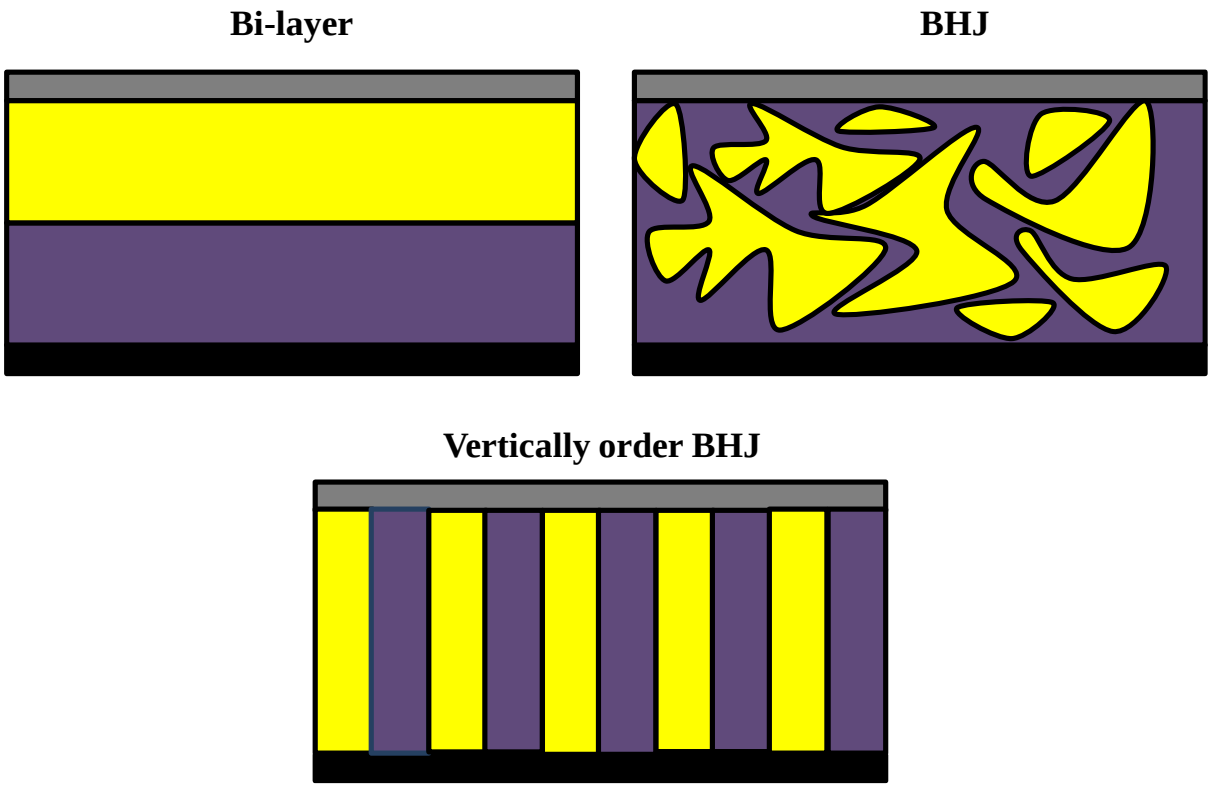

Fig. 2.14: Active layer architecture in OPVs.

The operating principles of organic solar cells are illustrated in Fig. 2.15. The donor material which is usually a conjugated polymer is photo-excited through light absorption to generate excitons. The exciton diffuses into a donor-acceptor (D-A) interface whereby dissociation occurs through electron transfer. The internal electric field generates the photo-current and photo-voltage from the separated charge carriers, which move to the electrodes. However, the lifetime of the carriers and the diffusion length results in the recombination of carriers [109-111]. This therefore leads to the reduction of efficiency. This can however be circumvented using BHJ architecture where the donor and acceptor have maximum interfacial connection. The BHJ can be obtained by careful synthesis and characterization of polymer nanocomposites.

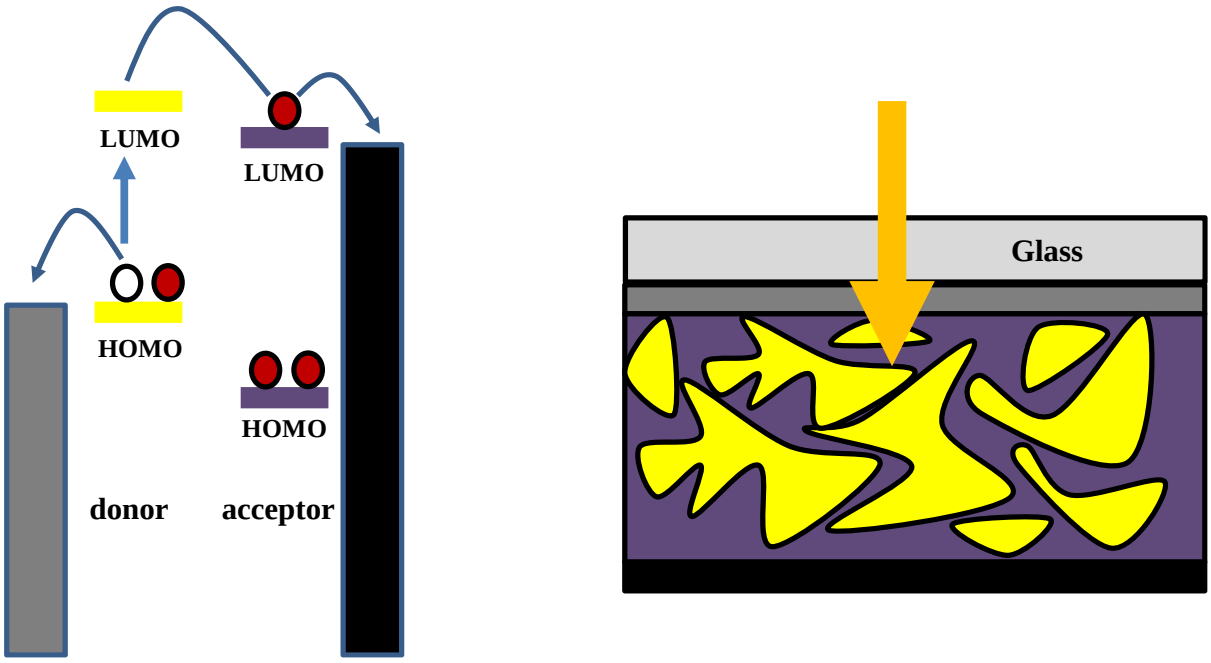

Fig. 2.15: Mechanism of a BHJ solar cell.

Apart from the short excitation lifetimes and short diffusion length, OPVs/BHJ solar cells also suffer from stability problems and have low strength due to the nature of the materials used. This has therefore prompted the fabrication of hybrid solar cells. These are modification of BHJ solar cells where PCBM is replaced with semiconductor nanocrystals. This is to try and solve all the issues associated with BHJ solar cells whilst improving on the efficiency by using the superior properties of semiconductor nanocrystals. Several researchers are engaged in this research area. Huynh et al. reported on the use of semiconductor nanorods in hybrid solar cells. A photovoltaic device consisting of 7-nanometer by 60-nanometer CdSe nanorods and P3HT was assembled from solution with an external quantum efficiency of over 54% yielding a device that had a conversion efficiency of 6.9% [112]. Olson et al. showed that different forms of nanoparticles affect the power conversion efficiencies in hybrid solar cells. Their group used CdSe tetrapods combined with a low band gap polymer, poly [2, 6-(4,4-bis-(2-ethylhexyl)-4H-cyclopenta [2, 1-*b*; 3, 4-*b*']dithiophene)-*alt*-4, 7-(2, 1, 3-benzothiadiazole)] (PCP-DTBT), to form the active layer of hybrid solar cells. They fabricated solar cells with power conversion

efficiency (PCE) of 3.2% under simulated air-mass (AM) 1.5 global irradiation of 1000 W/m^2 as well as their devices showed moderately high external quantum efficiency (EQE) of greater than 30% in a range of 350-800 nm with a maximum EQE of 55% in range of 630-720 nm [112]. Zhou et al. published a paper showing the effect of non-ligand exchange of CdSe quantum dots and P3HT conducting polymer on the PCE of the hybrid solar cell. Their group used a simple wash process using hexanoic acid to remove the capping ligand from the nanocrystals. The removal of the ligand showed no effect on the UV-Vis spectrum but did demonstrate higher PCE of 2% which at the time was higher than the efficiency of the short ligand butylamine which was reported at 1.77% [113]. Qiao et al. reported on a P3HT nanofibers/CdSe hybrid solar cell. They further showed that annealing improved performance of the solar cell which was attributed to the reduced barrier to interfacial charge transfer facilitated by the reduced organic content around the nanocrystals post annealing [114].

Evident from the studies above, three factors are important in achieving higher PCE in hybrid solar cells. Firstly, the morphology of the active layer is important, maximum interaction between the donor and the acceptor is crucial. This has been discussed at length above with the use of BHJ structures being most desired and also by using more anisotropic nanocrystals such as rods and tetrapods, the interaction can be improved. Secondly, the ligand surrounding the nanocrystals is a hindrance to charge transfer and reduces the interaction between the polymer and the nanocrystal due to its length. Unfortunately, these long-chained ligands are necessary in the synthesis of nanocrystals as they passivate the surface which minimizes defects hence resulting in good electronic properties. In addition, they control the nucleation and growth of the nanocrystals as well as prevent agglomeration hence resulting in particles that are monodispersed with uniform properties. There are two general strategies which are ligand exchange from original long alkyl ligands to shorter molecules e.g. pyridine, and chemical

surface treatment and washing for reducing the ligand shell. A combination of ligand shell reduction and ligand exchange afterwards might further improve the solar cell performance by enhancing the electron transport in the interconnected nanocrystal network [115]. Thirdly, annealing the device can also improve performance as excess organic material is removed and the crystallinity improves [116].

References

[1] N. Yaacobi-Gross, Colloidal Semiconductor Nanocrystals Based Solar Cells, **2012**, 201. Thesis

[2] C. Yuan, The Study of II-VI Semiconductor Nanocrystals Sensitized Solar Cells, **2012**, 125. Thesis

[3] S.V. Gaponenko, Optical properties of semiconductor nanocrystals, Cambridge university press, **1998**, 335.

[4] V.L.Colvin, A.N. Goldstein, A.P. Alivisatos; Journal of American Chemical Society, 114, **1992**, 5221.

[5] M.A. Olshavsky, N.A. Goldstein, A.P. Alivisatos ; Journal of American Chemical Society, 112, **1990**, 9438.

[6] M. Labrenz, G.K. Druschel, T. Thomsen_Ebert, B. Gilbert, S.A. Welch, K.M. Kemner, G.A. Logan, R.E. Summons, G.D. Stasio, P.L. Bond, B. Lai, S.D. Kelly, J.F. Banfield; Science, 290, **2000**, 1744.

[7] A.I. Ekimov, A.L. Efros, A.A. Onushchenko; Solid State Communications, 56, **1985**, 921.

[8] M. Chamarro, C. Gourdon, P. Lavallard, A.I. Ekimov; Japanese Journal of Applied Physics, 34, **1995**, 12.

[9] D. Norris, M. Bawendi; The Journal of chemical physics, 103, **1995**, 5260.

[10] P. Rodrigues, G. Tamulaitis, Y.Y. Peter, S.H. Risbud; Solid state communications, 94, **1995**, 583.

[11] D.J. Norris, Electronic structure in semiconductor nanocrystals, Marcel Dekker: New York, **2004**.

[12] C. De Oliveira, A. De Paula, F. Plentz Filho, J.M. Neto, L. Barbosa, O. Alves, E. Menezes, J. Rios, H. Fragnito, C.B. Cruz; Applied physics letters, 66, **1995**, 39.

[13] W. Hoheisel, V. Colvin, C. Johnson, A. Alivisatos; The Journal of chemical physics, 101, **1994**, 8455.

[14] M. Nirmal, C. Murray, M. Bawendi; Physical Review B, 50, **1994**, 2293.

[15] D. Norris, M. Nirmal, C. Murray, A. Sacra, M. Bawendi; Zeitschrift für Physik D Atoms, Molecules and Clusters, 26, **1993**, 355.

[16] D. Norris, A. Sacra, C. Murray, M. Bawendi; Physical review letters, 72, **1994**, 2612.

[17] V. Esch, B. Fluegel, G. Khitrova, H. Gibbs, X. Jiajin, K. Kang, S.W. Koch, L. Liu, S. Risbud, N. Peyghambarian; Physical Review B, 42, **1990**, 7450.

[18] N. Moloto, Synthesis, properties and applications of Mn, Co, Ni and Cu chalcogenide nanoparticles, **2011**.

[19] A. Ekimov, A. Onushchenko, Soviet Physics Semiconductors-USSR, 16 ,**1982**, 775.

[20] J. Warnock, D. Awschalom, Physical Review B, 32, **1985**, 5529.

[21] N.F. Borrelli, D. Hall, H. Holland, D. Smith, Journal of Applied Physics, 61, **1987,** 5399.

[22] D. Mocatta, G. Cohen, J. Schattner, O. Millo, E. Rabani, U. Banin, Science, 332,**2011**, 77.

[23] J. Wang, M.S. Gudiksen, X. Duan, Y. Cui, C.M. Lieber, Science, 293, **2001**, 1455.

[24] J. Hu, L.-s. Li, W. Yang, L. Manna, L.-w. Wang, A.P. Alivisatos, Science, 292, **2001**, 2060.

[25] X. Peng, L. Manna, W. Yang, J. Wickham, E. Scher, A. Kadavanich, A.P. Alivisatos, Nature, 404, **2000**, 59.

[26] V.F. Puntes, K.M. Krishnan, A.P. Alivisatos, Science, 291 .**2001**, 2115.

[27] T.S. Ahmadi, Z.L. Wang, T.C. Green, A. Henglein, M.A. El-Sayed, Science, 272 ,**1996**, 1924.

[28] Z.A. Peng, X. Peng, Journal of the American Chemical Society, 123 ,**2001**, 1389.

[29] Z.A. Peng, X. Peng, Journal of the American Chemical Society, 124 .**2002**, 3343.

[30] C. Pu, J. Zhou, R. Lai, Y. Niu, W. Nan, X. Peng, Nano research, 6 ,**2013**, 652.

[31] Y. Yin, A.P. Alivisatos, Nature, 437, **2005**, 664.

[32] H. Weller, Sciences, 361, **2003**, 229.

[33] O. Chen, X. Chen, Y. Yang, J. Lynch, H. Wu, J. Zhuang, Y.C. Cao, Journal of the Gesellschaft Deutscher Chemiker 47, **2008**, 8638.

[34] L.C. Roof, J.W. Kolis, Chemical reviews, 93, **1993**, 1037.

[35] M. Han, X. Gao, J.Z. Su, S. Nie, Nature biotechnology, 19, **2001**, 631.

[36] I.L. Medintz, H.T. Uyeda, E.R. Goldman, H. Mattoussi, Nature materials, 4, **2005**, 43.

[37] D.V. Talapin, C.B. MurrayScience, 310, **2005**, 86.

[38] L. Zhu, M.-Q. Zhu, J.K. Hurst, A.D. Li, Journal of the American Chemical Society, 127, **2005**, 8968.

[39] M. Kazes, D.Y. Lewis, Y. Ebenstein, T. Mokari, U. Banin, Advanced Materials, 14, **2002**, 317.

[40] S. Coe, W.-K. Woo, M. Bawendi, V. Bulović, Nature, 420, **2002**, 800.

[41] I. Gur, N.A. Fromer, M.L. Geier, A.P. Alivisatos, Science, 310, **2005**, 462.

[42] C. Murray, D.J. Norris, M.G. Bawendi, Journal of the American Chemical Society, 115, **1993**, 8706.

[43] Z. Peng, X. Peng, Journal of the American Chemical Society, 123, **2001**, 183.

[44] M.A. Hines, P. Guyot-Sionnest, The Journal of Physical Chemistry, 100, **1996**, 468.

[45] X. Peng, M.C. Schlamp, A.V. Kadavanich, A.P. Alivisatos, Journal of the American Chemical Society, 119, **1997**, 7019.

[46] D.J. Norris, A.L. Efros, S.C. Erwin, Science, 319, **2008**, 1776.

[47] N. Pradhan, D. Goorskey, J. Thessing, X. Peng, Journal of the American Chemical Society, 127, **2005**, 17586.

[48] P. Reiss, New Journal of Chemistry, 31, **2007**, 1843.

[49] N.S. Norberg, G.L. Parks, G.M. Salley, D.R. Gamelin, Journal of the American Chemical Society, 128, **2006**, 13195.

[50] D.A. Bussian, S.A. Crooker, M. Yin, M. Brynda, A.L. Efros, V.I. Klimov, Nature materials, 8, **2009**, 35.

[51] M. Ibáñez, R. Zamani, A. LaLonde, D. Cadavid, W. Li, A. Shavel, J. Arbiol, J.R. Morante, S. Gorsse, G.J. Snyder, Journal of the American Chemical Society, 134, **2012**, 4060.

[52] C. Xiao, J. Xu, K. Li, J. Feng, J. Yang, Y. Xie, Journal of the American Chemical Society, 134, **2012**, 4287.

[53] F.J. Fan, Y.X. Wang, X.J. Liu, L. Wu, S.H. Yu, Advanced Materials, 24, **2012**, 6158.

[54] K.S. Leschkies, T.J. Beatty, M.S. Kang, D.J. Norris, E.S. Aydil, American Chemical Society Nano, 3, **2009**, 3638.

[55] Q. Guo, S.J. Kim, M. Kar, W.N. Shafarman, R.W. Birkmire, E.A. Stach, R. Agrawal, H.W. Hillhouse, Nano letters, 8, **2008**, 2982.

[56] J.M. Luther, M. Law, Q. Song, C.L. Perkins, M.C. Beard, A.J. Nozik, American Chemical Society Nano, 2, **2008**, 271.

[57] J. Guo, S. Liang, Y. Shi, C. Hao, X. Wang, T. Ma, Physics, 17, **2015**, 28985.

[58] X. Zhang, M. Zhen, J. Bai, S. Jin, L. Liu, ACS Applied Materials & Interfaces, 8, **2016**, 17187.

[59] F. Gong, H. Wang, X. Xu, G. Zhou, Z.-S. Wang, Journal of the American Chemical Society, 134, **2012**, 10953.

[60] F. Gong, X. Xu, Z. Li, G. Zhou, Z.-S. Wang, Chemical communications, 49, **2013**, 1437.

[61] A.I. Ekimov, A.L. Efros, A.A. Onushchenko, Solid State Communications, 56, **1985**, 921.

[62] M. Chamarro, C. Gourdon, P. Lavallard, A.I. Ekimov, Japanese Journal of Applied Physics, 34, **1995**, 12.

[63] D. Norris, M. Bawendi, The Journal of chemical physics, 103, **1995**, 5260.

[64] P. Rodrigues, G. Tamulaitis, Y.Y. Peter, S.H. Risbud, Solid state communications, 94, **1995**, 583.

[65] D.J. Norris, Electronic structure in semiconductor nanocrystals, Marcel Dekker: New York, 2004.

[66] C. De Oliveira, A. De Paula, F. Plentz Filho, J.M. Neto, L. Barbosa, O. Alves, E. Menezes, J. Rios, H. Fragnito, C.B. Cruz, Applied physics letters, 66, **1995**, 439.

[67] W. Hoheisel, V. Colvin, C. Johnson, A. Alivisatos, The Journal of chemical physics, 101, **1994**, 8455.

[68] M. Nirmal, C. Murray, M. Bawendi, Physical Review B, 50, **1994**, 2293.

[69] D. Norris, M. Nirmal, C. Murray, A. Sacra, M. Bawendi, Molecules and Clusters, 26, **1993**, 355-357.

[70] D. Norris, A. Sacra, C. Murray, M. Bawendi, Physical review letters, 72, **1994**, 2612.

[71] V. Esch, B. Fluegel, G. Khitrova, H. Gibbs, X. Jiajin, K. Kang, S.W. Koch, L. Liu, S. Risbud, N. Peyghambarianm, Physical Review B, 42, **1990**, 7450.

[72] A.O. Nejo, Synthesis of organically capped and water soluble metal sulphide semiconductor nanoparticles, in University of Zululand, 2013, Thesis.

[73] A.L. Efros, A.L. Efros, Soviet Physics Semiconductors-USSR, 16, **1982**, 772.

[74] A.L. Efros, M. Rosen, Annual Review of Materials Science, 30, **2000**, 475.

[75] A. Ekimov, A. Onushchenko, A. Plyukhin, A.L. Efros, JETP, 61, **1985**, 891.

[76] A.I. Ekimov, A.A. Onushchenko, ZhETF Pisma Redaktsiiu, 34, **1981**, 363.

[77] T. Itoh, Y. Iwabuchi, T. Kirihara, Physica status solidi (b), 146, **1988**, 531.

[78] A. Ekimov, A. Onushchenko, A.L. Éfros, ZhETF Pisma Redaktsiiu, 43, **1986**, 292.

[79] A. Ekimov, A.L. Efros, M. Ivanov, A. Onushchenko, S. Shumilov, Solid State Communications, 69, **1989**, 565.

[80] G. Mshvelidse, O. Gogolin, E. Tsitsishvili, C. Märkle, J. Chadha, A. Hepting, F. Gindele, W. Petri, W. Send, D. Gerthsen, Physica Status Solidi B Basic Research, 207, **1998**, 369.

[81] M. Nirmal, L. Brus, Accounts of Chemical Research, 32, **1999**, 407.

[82] E. Groeneveld, Synthesis and optical spectroscopy of (hetero)-nanocrystals: An exciting interplay between Chemistry and Physics, **2012**, Thesis.

[83] R. Koole, E. Groeneveld, D. Vanmaekelbergh, A. Meijerink, C. de Mello Donegá, Nanoparticles, Springer, **2014**, 13.

[84] Y. Zhou, M. Eck, C. Veit, B. Zimmermann, F. Rauscher, P. Niyamakom, S. Yilmaz, I. Dumsch, S. Allard, U. Scherf, M. Krüger; Solar Energy Materials and Solar Cells, 95, **2011**, 1232.

[85] L.O. Brown, J.E. Hutchison; Journal of American Chemical Society, 121, **1999**, 3414.

[86] M. Kuno, J.K. Lee, B.O. Dabbousi, F.V. Mikulec, M.G. Bawendi; Journal of Chemical Physics, 106, **1997**, 4403.

[87] I. Lokteva, N. Radychev, F. Witt, H. Borchert, J. Parisi, J. Kolny-Olesiak; Journal of Physical Chemistry. C, 114, **2010**, 4747.

[88] N. Moloto, N.J. Coville, S.S. Ray, M.J. Moloto, Physica B, 404, **2009**, 4461.

[89] Y. Li, A. Rizzo, M. Mazzeo, L. Carbone, L. Manna, R. Cingolani, G. Gigli, Journal of Applied Physics97, **2005**, 125.

[90] P.O. Anikeeva, J.E. halpert, M.G. Bawedi, V. Bulovic, Nano Letters, 9, **2009**, 2532.

[91] W. Chung, K. Park, H.J. Yu, J. Kim, B-H. Chun, S.H. Kim; Optical Materials, 32, **2010**, 515.

[92] J, George, R. Kumar, V.A. Sajeevkumar, K.V. Ramana, R. Rajamanickam, V. Abhishek, S. Nadanasabapathy, Siddaramaiah, Carbohydrate Polymers, 105, **2014**, 285.

[93] X. Gong, C.Y. Tang, L. Pan, Z. Hao, C.P. Tsui, Composites; Part B, 60, **2014**, 494.

[94] C. B. Murray, D. J. Norris and M. G. Bawendi; Journal of American Chemical Society, 115, **1993**, 8706.

[95] M. Darbandi, G. Urban and M. Krüger, Journal of Colloid and Interface Science, 351, **2010**, 30.

[96] D. J. Norris and M.G Bawendi, Physic Review B, 53, **1996**.

[97] C.J Murphy, Analytical Chemistry, A, **2002**, 2319.

[98] D.L. Waldron, A. Preske, J.M. Zawodyn, T.D. Krauss, M.C. Gupta, Nanotechnology, 26(7), **2015**, 4484.

[101] J. Pyun and K. Matyjaszewski, Chemical Materials,13, **2001**, 3436.

[102] K. Ohno, K. Koh, Y. Tsuji, and T. Fukuda, Macromolecules, 35, **2002**, 8989.

[103] T. Lui, S. Jia, T. Kowalewski, K. Matyjaszewski, R. Casadio-Portilla, and J. Belmont, Langmuir, 19, **2003**, 6342.

[104] Y.-P. Wang, X.-W. Pei, and K. Yuan, Material Letters, 59, **2005**, 1614.

[105] K. Yoshinaga and M. Teramoto, Bull. Chemical Society. Journal., 69, **1996**, 2667.

[106] C. Querner, P. Reiss, S. Sadki, M. Zagorska and A. Pron, Physical Chemistry, 7, **2005**, 3204.

[107] E. Kucur, J. Riegler, G. A. Urban and T. Nann, Journal of Chemical Physics, 119, **2003**, 2333.

[108] Y. Yang and S. Chen; Nano Letters, 3, **2003**, 343.

[109] S. K. Haram, A. Kshirsagar, Y. D. Gujarathi, P. P. Ingole, O. A. Nene, G. B. Markad and S. P. Nanavati, Journal of Physical Chemistry, 115, **2011**, 6243.

[110] M. Soreni-Harari, N. Yaacobi-Gross, D. Steiner, A. Aharoni, U. Banin, O. Millo and N. Tessler, Nano Letters, 8, **2008**, 678.

[111] Z. Ding, B. M. Quinn, S. K. Haram, L. E. Pell, B. A. Korgel. A. J. Bard, Science, 296, **2002**, 1293.

[112] J. Bisquert, D. Cahen, G. Hodes, S. Rühle and A. Zaban, Journal of Physical Chemistry. B, 108, **2004**, 8106.

[113] N.C Greenham, X, Poeng, A.P Alivisatos, Phyical Reviews B, 54, **1996**, 17628.

[114] J.L. Bredas, D. Beljonne, V. Coropeeanu, J. Cornil, Chemical Reviews, 104, **2004**, 4971.

[115] A.J Nozik, Physica E, 14, **2002**, 11.

[116] D. Kumar, R.C. Sharma, European Polymer Journal, 34, **1998**, 1053.

CHAPTER 3

SIZE QUANTIZATION IN Cu_2Se NANOCRYSTALS

3.1 Introduction

Semiconductor nanocrystals in colloidal form can potentially offer many benefits as active photovoltaic (PV) materials in building of the next generation of solar cells. Much of their attractiveness is attributed to their tuneable properties. Engineering of their size, shape and composition can have a vast influence on their electronic and optical properties [1-5]. Furthermore, their large surface to volume ratio and solution processability can forge the realization of cheap, high efficient solar cells. The effect of size on the electronic and optical properties of semiconductor nanocrystals has been well studied in colloidal cadmium chalcogenides however little or no work on size dependent optical properties for copper selenide has been reported [6-10]. Copper selenide nanocrystals are particularly interesting candidates for PV applications as they offer the green pathway as compared to cadmium containing chalcogenides. In addition, the metal precursors for the synthesis of copper selenide are very cheap and highly abundant [11]. Copper selenide is a p-type semiconductor with a direct band gap ranging from 2.1-2.39 eV and an indirect band gap ranging from 1.2-1.7 eV [12]. It can exist in many crystalline phases including monoclinic, cubic, and hexagonal and can possess various stoichiometric ratios such as CuSe, Cu_2Se, $CuSe_2$, and Cu_3Se_2 as shown in Fig. 3.1 [13]. The formation of different stoichiometries of copper selenide makes its synthesis challenging. However, by carefully controlling the synthetic parameters, one can determine the specific conditions for a specified stoichiometry.

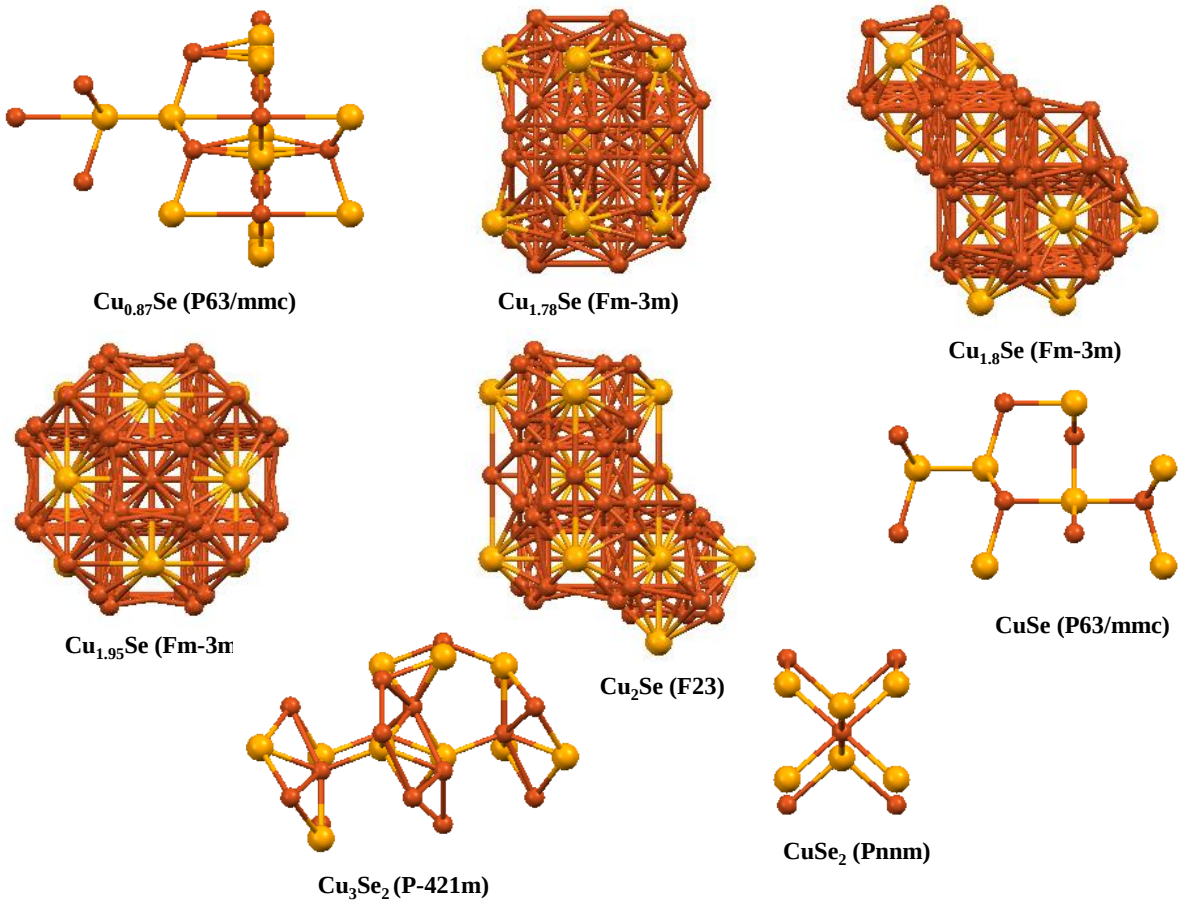

Fig. 3.1: Stoichiometries and space group of copper-selenium.

In nanotechnology and more specifically in colloidal synthesis, one can manipulate the size and shape of the nanoparticles by varying the synthesis parameters such as time, temperature, concentration and capping agents [14-15]. Time has been shown to result in the growth of particle sizes. This is due to the Ostwald repining effect. The time effect can be easily observed in the synthesis CdSe nanoparticles where evolution of different colours is observed with increased time [16]. This is also established in the absorption spectra where a red shift is observed with increasing sizes. Temperature can also affect the resultant particles. This is particularly seen for copper selenide in the phase diagram shown in Fig. 3.2 where different stoichiometries and crystal phases are seen at different temperatures [17].

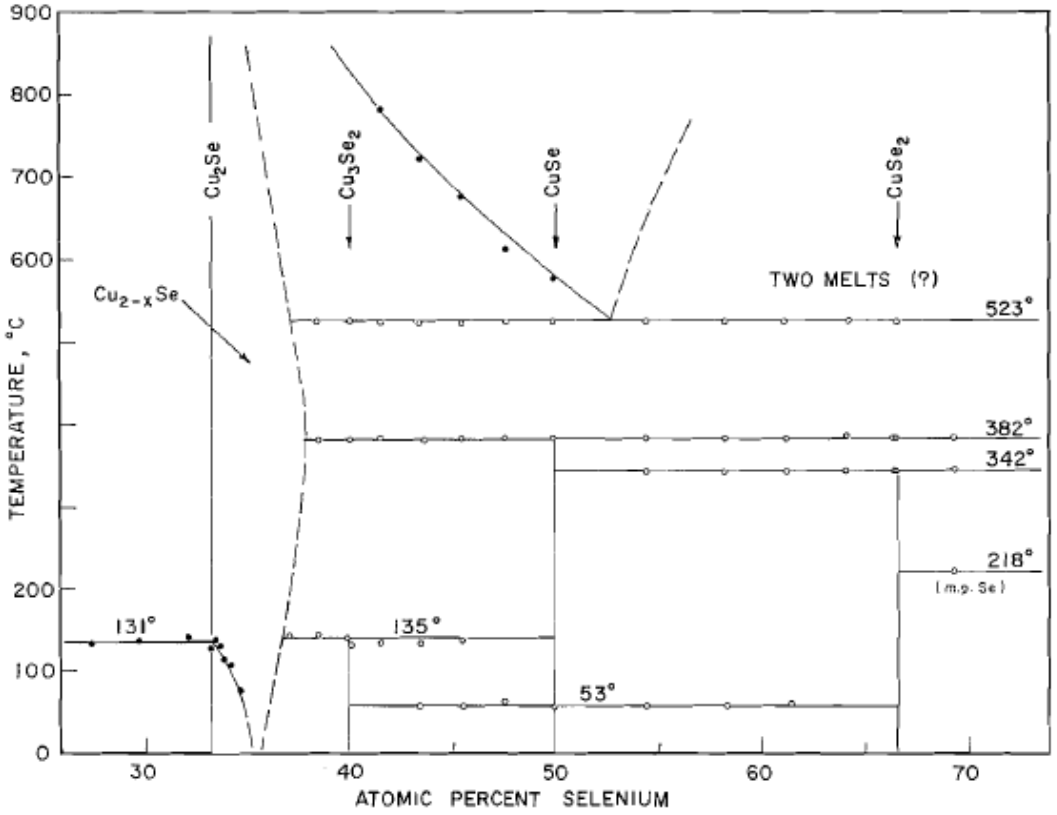

Fig. 3.2: Phase diagram of copper-selenium.

The concentration has an effect on the nucleation step in the synthesis of the particles and influences the amount of monomers present and can result in either an increase in particle sizes with increasing concentration or it can alter the morphology of the particles [18]. Capping agents/surfactants can influence the reactivity hence the nucleation of the particles by binding strongly or weakly on the surface of the nuclei. In addition they can have preferential attachment to specific crystallographic planes hence resulting in the growth of anisotropic particles [19]. The interest in employing copper selenide stems from its various reported applications such as thin-film photovoltaics, optical filters and dry galvanic cells (as solid electrolytes) [20,21]. Copper selenide has been prepared using various methods with the majority being thin-film produced using techniques such as electrodeposition and chemical bath deposition [22–24]. However a number of solution-based synthetic routes yielding

nanocrystals have not been sufficiently reported including colloidal synthesis in hot coordinating and non-coordinating solvents. Herein we report on the synthesis of copper selenide using the colloidal hot injection method. The effect of time and temperature on the stoichiometry and size of the nanoparticles is also studied. In addition, we report for the first time visualizable size quantization in copper selenide nanocrystals.

3.2 Experimental section

3.2.1 Materials

Copper(I)chloride, selenium powder, trioctylphosphine (TOP), hexadecylamine (HDA), chloroform and methanol were all purchased from Sigma-Aldrich.

3.2.2 Synthesis of the Cu_2Se nanocrystals

Copper selenide nanocrystals were prepared under inert conditions using a one pot synthesis method. In a typical synthesis 0.8 g of CuCl was dissolved in 5 ml of TOP, the solution was stirred for 1 hr at room temperature. 1.0 g of Se powder was dissolved in 5 ml of TOP and the solution was also stirred for 1 hr at room temperature. About 5 g of HDA was heated under N_2 gas to 100 °C. Thereafter the TOP-Se solution was added to the HDA and the temperature was increased to 220 °C. At 220 °C the TOP- CuCl solution was added to the reaction flask and a temperature drop was observed. The temperature was then increased to 220 °C and then the timer was started. Aliquots at 2, 4, 6, 8, 10, 15, 30 and 60 min were then taken. The nanocrystals were flocculated by the addition of methanol. The resultant crystals were then washed several times with hot methanol and the powders were collected by centrifugation and they were allowed to dry in air and were later dispersed in chloroform. For the temperature study the reactions were carried out at 140,180, 220 and 260 °C.

3.2.3 Instrumentation

A Varian Cary Eclipse (Cary 50) UV-Vis spectrophotometer was used to carry out the absorption measurements. A Varian Cary Eclipse EL04103870 fluorescence spectrophotometer with a medium PMT voltage at an excitation wavelength of 200 nm was used to measure the photoluminescence of the particles. For both spectral analysis, the powders were dissolved in chloroform and placed in quartz cuvettes (1cm path length). XRD patterns on powdered samples were measured on a Bruker MeasSrv D2-205530 diffractometer using secondary graphite monochromated CuKα radiation (λ 1.54060 Å) at 30 kV/30 mA. Measurements were taken using a glancing angle of incidence detector at an angle of 2˚, for 2θ values over 10 - 90° in steps of 0.026° with a step time of 37 s and at a temperature of 25 °C. The transmission electron microscopy (TEM) was carried out on a FEI Technai T12 TEM microscopy operated at an acceleration voltage of 200 kV with a beam spot size of 20 - 100 nm in TEM mode. The samples were prepared by placing a drop of the suspended nanoparticles in chloroform, on a carbon-copper grid. The grid with the sample was then allowed to dry at room temperature.

3.3 Results and discussion

3.3.1 Size quantization in Cu_2Se nanocrystals

Size quantization has been readily shown on binary metal chalcogenides particularly on CdSe nanocrystals with the classical picture depicting the different colours of the nanocrystals [16, 24-25]. Herein, we report for the first time the physically visible size quantization effect on Cu_2Se nanocrystals after the variation of the synthetic time. The colours vary from bright blue to green, yellow, brown and ultimately black with the increase in time of synthesis as depicted in Fig. 3.3.

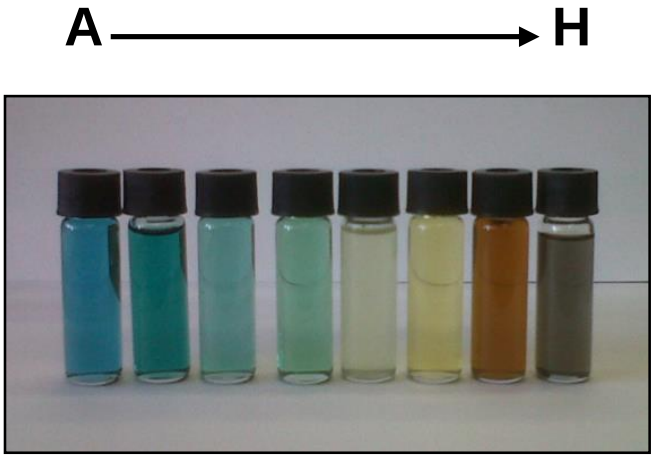

Fig. 3.3.: Size quantization effect in Cu_2Se nanocrystals depicted by the change in colour with an increase in time, A being an aliquot at 2 min through to H and aliquot at 60 min.

The optical characterization of the as prepared nanocrystals was then performed in order to confirm the quantization effect. Fig. 3.4 shows the absorption and emission spectra of selected copper selenide nanocrystals and Table 3.1 summarizes the results for all the samples. Fig. 3.4 shows the absorption and emission data from the time variation reactions. The absorption spectrum of sample A shows two well defined excitonic peaks with the band edge located at 795 nm. The band edge is indicative of an indirect band gap transition and is however blue-shifted from the bulk band edge of 886 nm. As the time is prolonged as seen in Fig. 3.4 and Table 3.1, there is a slight red-shift of the band edge from the 2 min sample (A) to the 8 min sample (D). However, it must be said that the UV-Vis absorption spectrum of copper chalcogenides usually shows a broad curve with no clearly defined absorption band edge. Nevertheless, the emission spectrum can be used as a rough indicator of the absorption band edge. A red-shift in the emission maximum from A to D is observed. This is indicative of the growth in particle sizes. As the time is increased beyond 8 min, there is initially a significant red-shift in the absorption spectrum however further increments see no changes in the absorption band edges and emission maxima. Nevertheless, the emission spectrum shows

successive broadening until the 60 min sample where the size distribution is now tuned to near monodespersity.

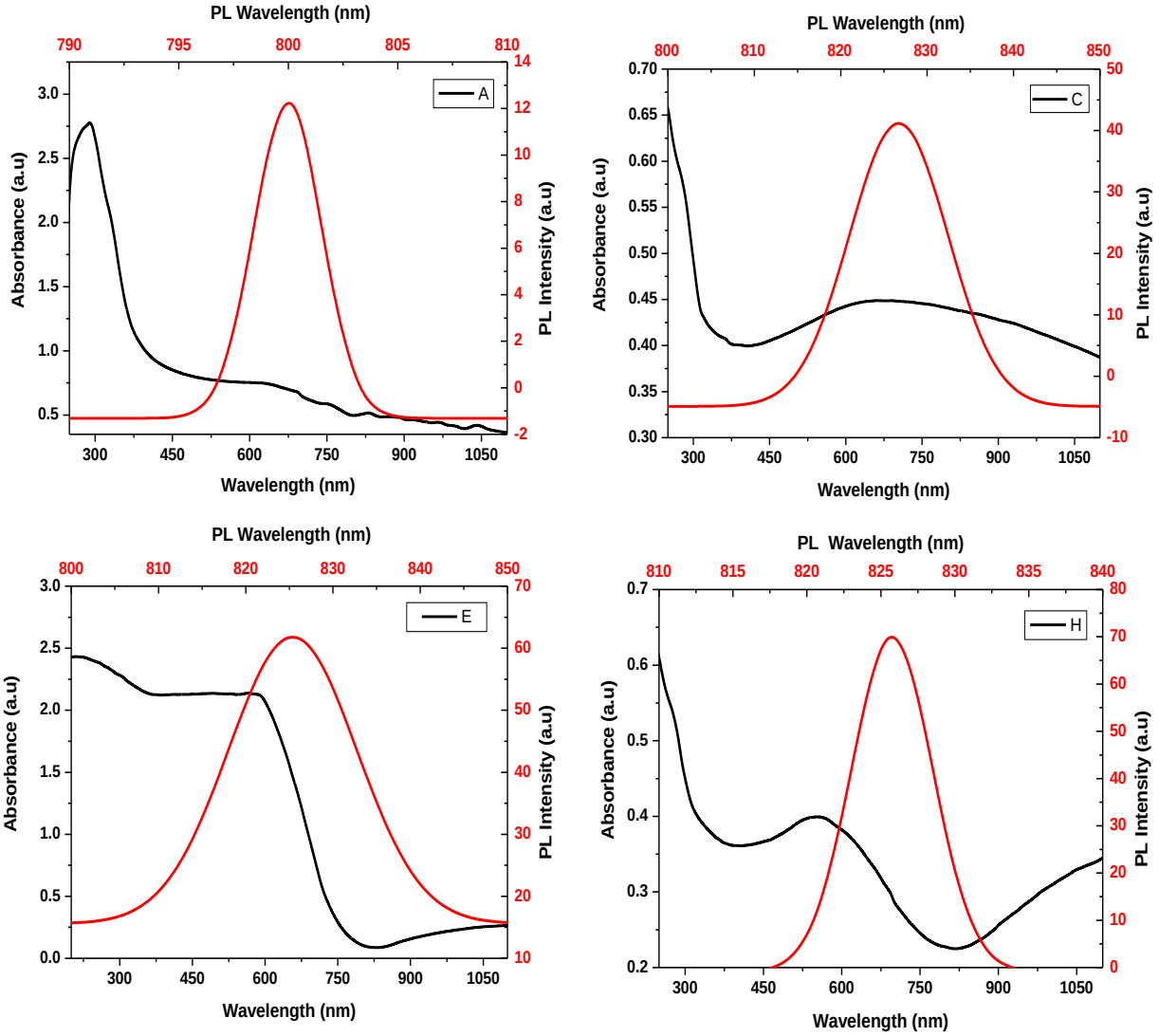

Fig. 3.4: UV-Vis absorption and photoluminescence of spectra of samples A, C, E and H.

Table 3.1: UV-Vis absorption band edges and emission maxima for samples A to H

Sample	Colour	Absorption λ (nm)	Emission λ (nm)
A	Blue	795	800
B	Bluish-green	-	812
C	Light green	-	826
D	Green	800	826
E	Opaque	818	826
F	Yellow	818	826
G	Brownish-orange	818	826
H	Dark brown	818	826

The composition and structure of the nanocrystals were determined by XRD and TEM studies. The XRD diffractograms for samples A, C, E and H are shown in Fig. 3.5. The diffractograms showed diffraction peaks for samples A, C and E that are attributed to the capping agent HDA (JCPDS card no.: 00-042-1782). Because of the small sizes of the nanocrystals, the presence of capping agent molecules overwhelms the diffraction from the nanocrystals, however as the nanocrystal size increased as in sample H, the diffraction peak could be indexed to a face centred cubic phase of Cu_2Se with the 2θ values 31.2°, 36.4°, 52.1°, 62°, 76.7° and 84.9° corresponding to the (111), (200), (220), (311), (400) and (420) planes (JCPDS card no.: 03-065-2982). Energy-dispersive X-ray spectroscopy was also done on the samples and confirmed the presence of Cu and Se (Fig. 3.1S).

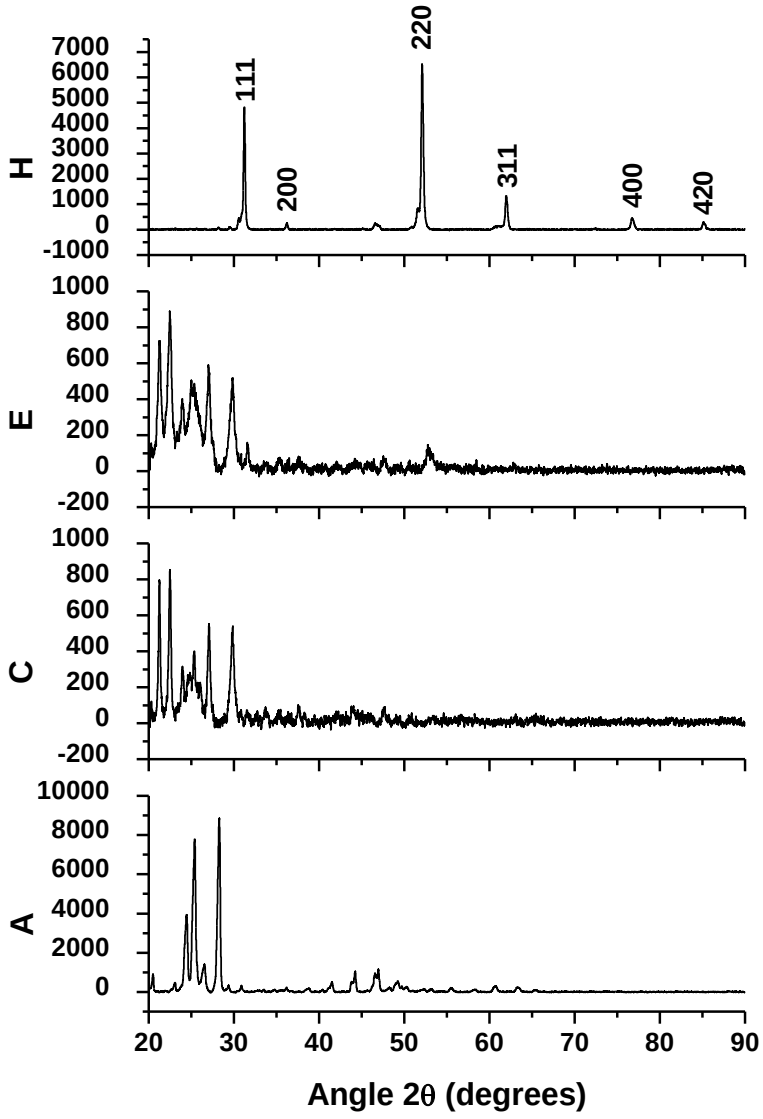

Fig. 3.5: PXRD patterns of samples A, C, E and H.

The morphologies of the nanocrystals are shown in Fig. 3.6. The 2 min sample (A) shows very small agglomerated particles. This is however expected as the XRD showed a large presence of the capping agent. As the time is increased to 6 min (C), the size of the particles increased to 2.7 nm. The particles also showed some degree of polydispersity and this is in agreement with the observed broadening of the emission spectrum. As the time is further increased to 10 min, the particle sizes further increase to 3.5 nm and the 60 min sample showed sizes with an

average diameter of 7 nm. Generally, the particles were of small sizes and less than the Bohr radius of copper selenide.

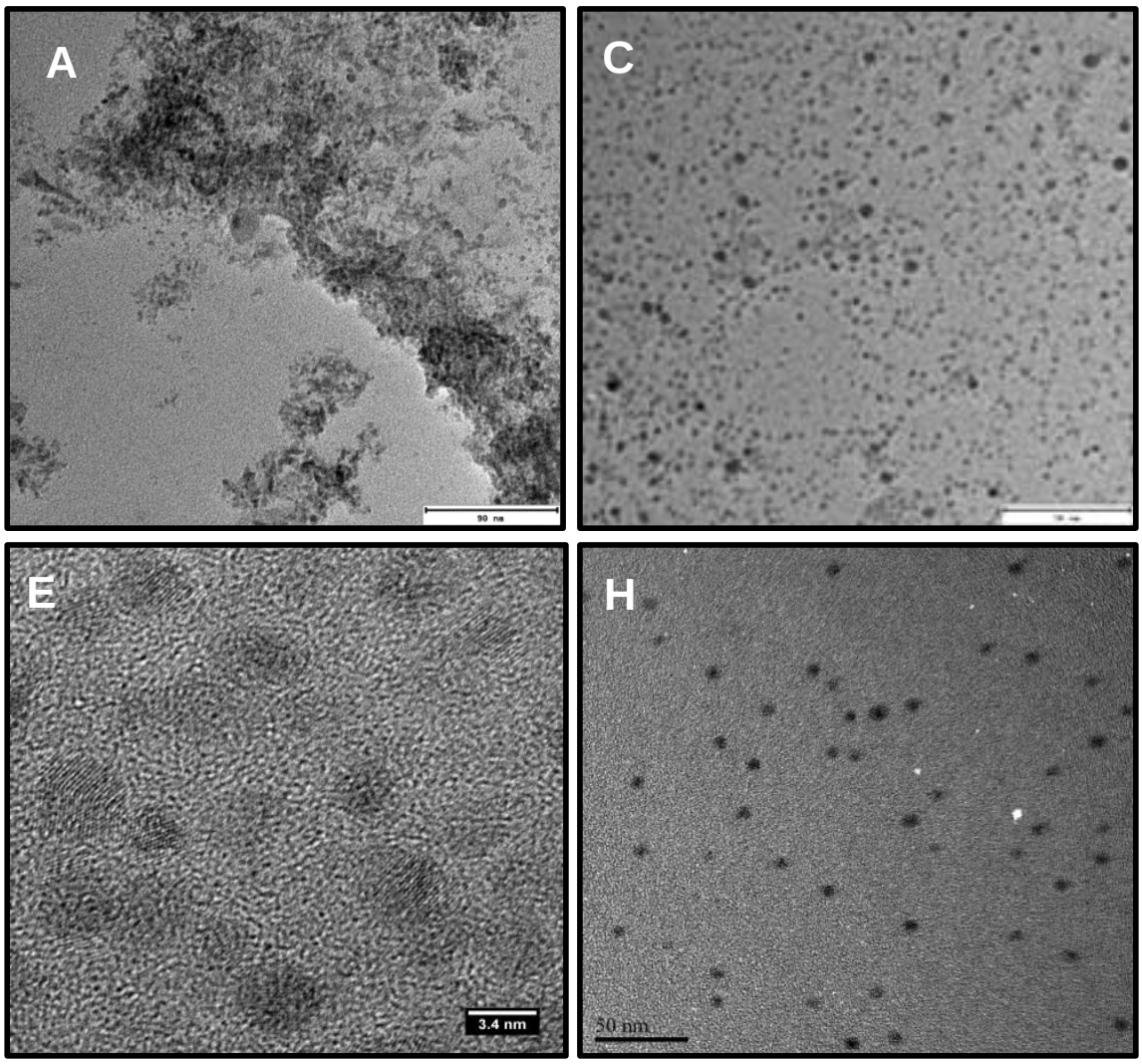

Fig. 3.6: TEM images of samples A to H.

3.3.2 Effect of temperature on the properties of copper selenide

It is well known that temperature plays a major role in the growth of nanoparticles. Temperature has been shown to have an effect on size of the nanoparticles, with higher temperatures resulting in larger nanoparticle sizes. The reaction temperature may also affect the shape of the nanoparticles due to the competition between the kinetics and thermodynamic growth regime [26]. Key to these materials is that at different temperatures, they form different products with

different stoichiometries. However, working in the nano regime can also bring about surprising results as the dynamics of reactions are quite different from the corresponding bulk. The time of synthesis was chosen to be 6 min, mainly because the particles were small but more stable compared to the 2 and 4 min samples. The 2 and 4 min samples within a period of two weeks showed signs of agglomeration indicative by the change in colours from blue to black signifying that the particles were bigger.

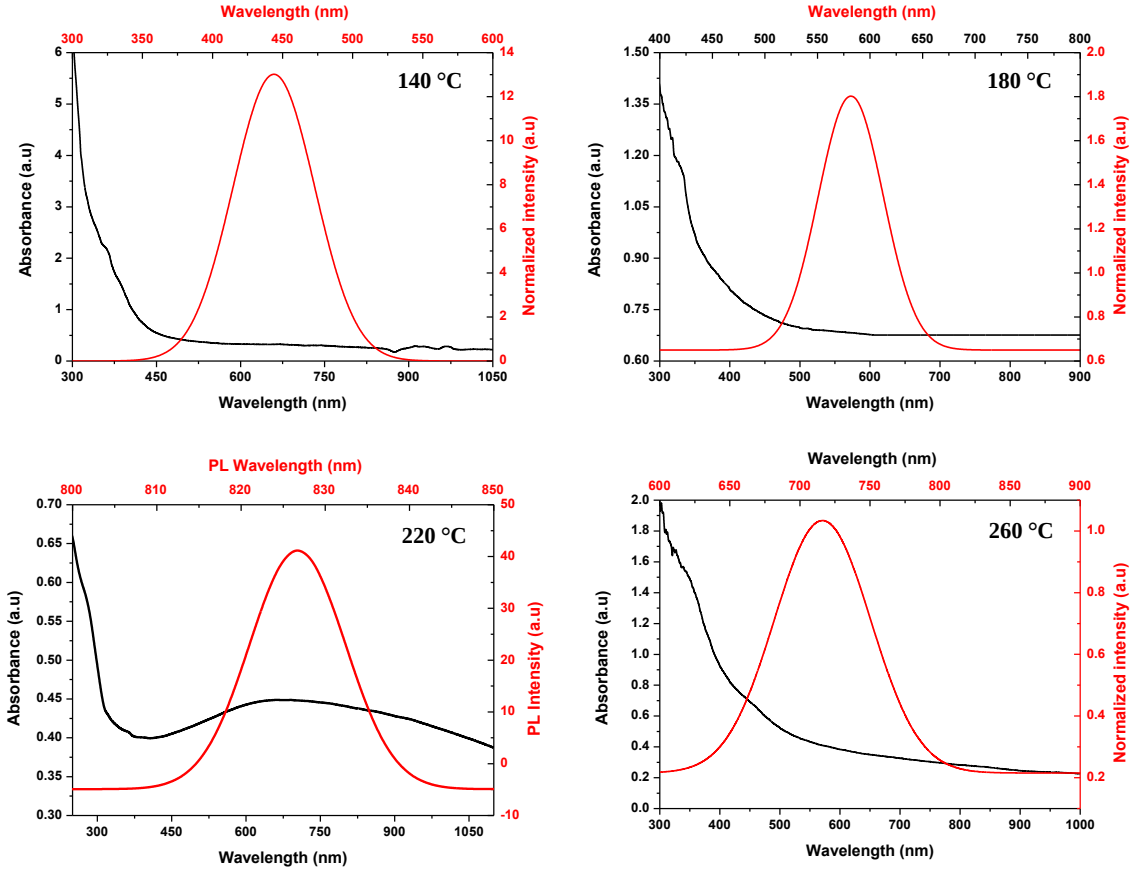

Fig. 3.7: UV-Vis absorption and photoluminescence spectra of copper selenide nanocrystals synthesized at different temperatures.

The optical properties of samples prepared at 140, 180, 220 and 260 °C are shown in Fig. 3.7 and summarized in Table 3.2. The UV-Vis absorption spectra of samples synthesized from 140, 180 and 260 °C have a band edge indicative of a direct bang gap semiconductor. Copper

selenide has direct band gap between 2.1-2.39 eV corresponding to 519 and 590 nm. The band edges are however blue shifted from the bulk values. This is due to quantum confinement and is attributed to the small sizes of the nanoparticles. The particles synthesized at 260 °C does however show two peak shoulders with the edges located at 407 nm and 522 nm. This signifies a polydispersed sample. The particles synthesized at 220 °C shows a very broad shoulder thus making it impossible to estimate the band edge.

Table 3.2: Summary of the optical properties of copper selenide particles synthesized at different temperatures

Sample	Absorption λ (nm)	Emission λ (nm)	FWHM (nm)
140 °C	436	445	70
180 °C	456	583	77
220 °C	-	826	15
260 °C	407 (522)	716	81

The emission maxima for all the samples are red-shifted absorption band edges. The full-width-half-maximum (FWHM) can be an indication of the size distribution of the particles. In general, a FWHM greater than 100 nm is regarded as a sign of polydispersity. Evidence from Table 3.2 revealed, all the samples were nearly monodispersed. However, the sample synthesized at 260 °C had the largest FWHM. This is not surprising as there were two peaks observed in absorption spectrum hinting to two size populations of particles.

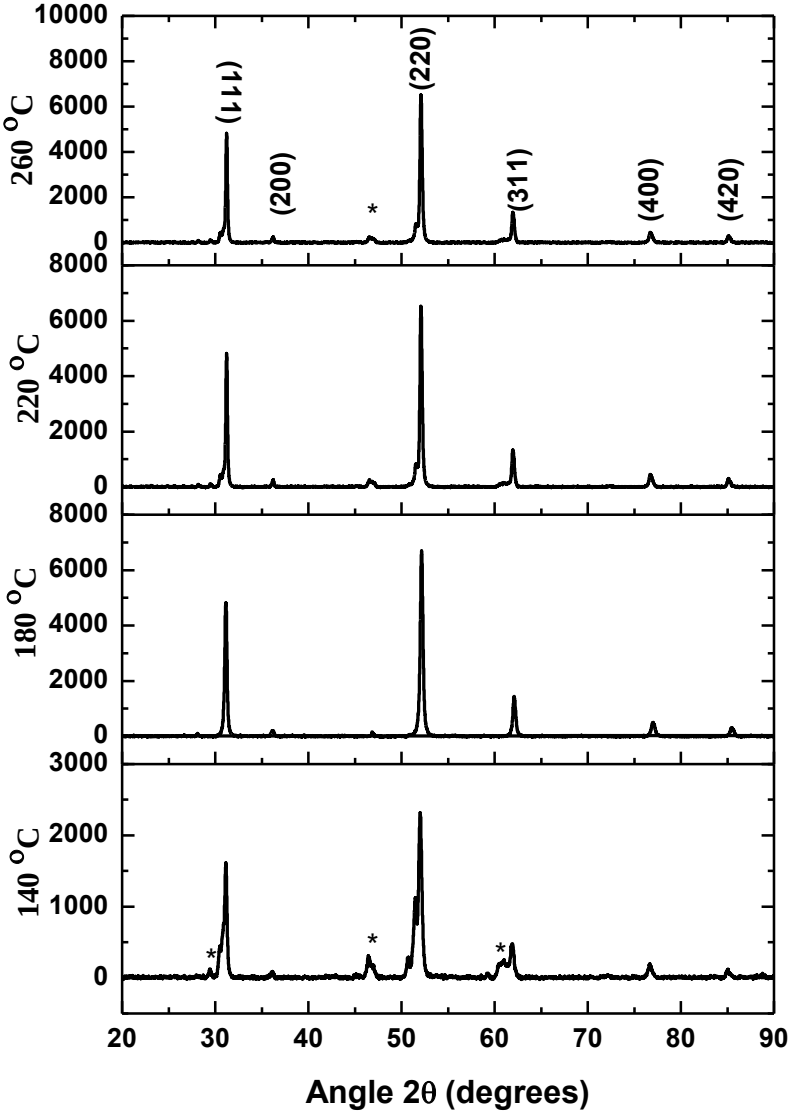

Fig. 3.8: X-ray diffraction of copper selenide nanocrystals synthesized at different temperatures where * signifies Se.

X-ray diffraction was done to probe the crystal structure of the resultant nanoparticles and to ascertain the dominant phase. The results are shown in Fig. 3.8. The diffraction patterns are the same except for particles synthesized at 140 °C where a large presence of unreacted selenium was seen. The solubility of selenium at lower temperatures is a bit problematic hence the detection of it. Nevertheless, all the particles were indexed to a face centred cubic phase of

Cu_2Se (JCPDS card no.: 03-065-2982). The temperature used in this study did not influence the crystal phase of the nanocrystals signifying that Cu_2Se is stable within this temperature range.

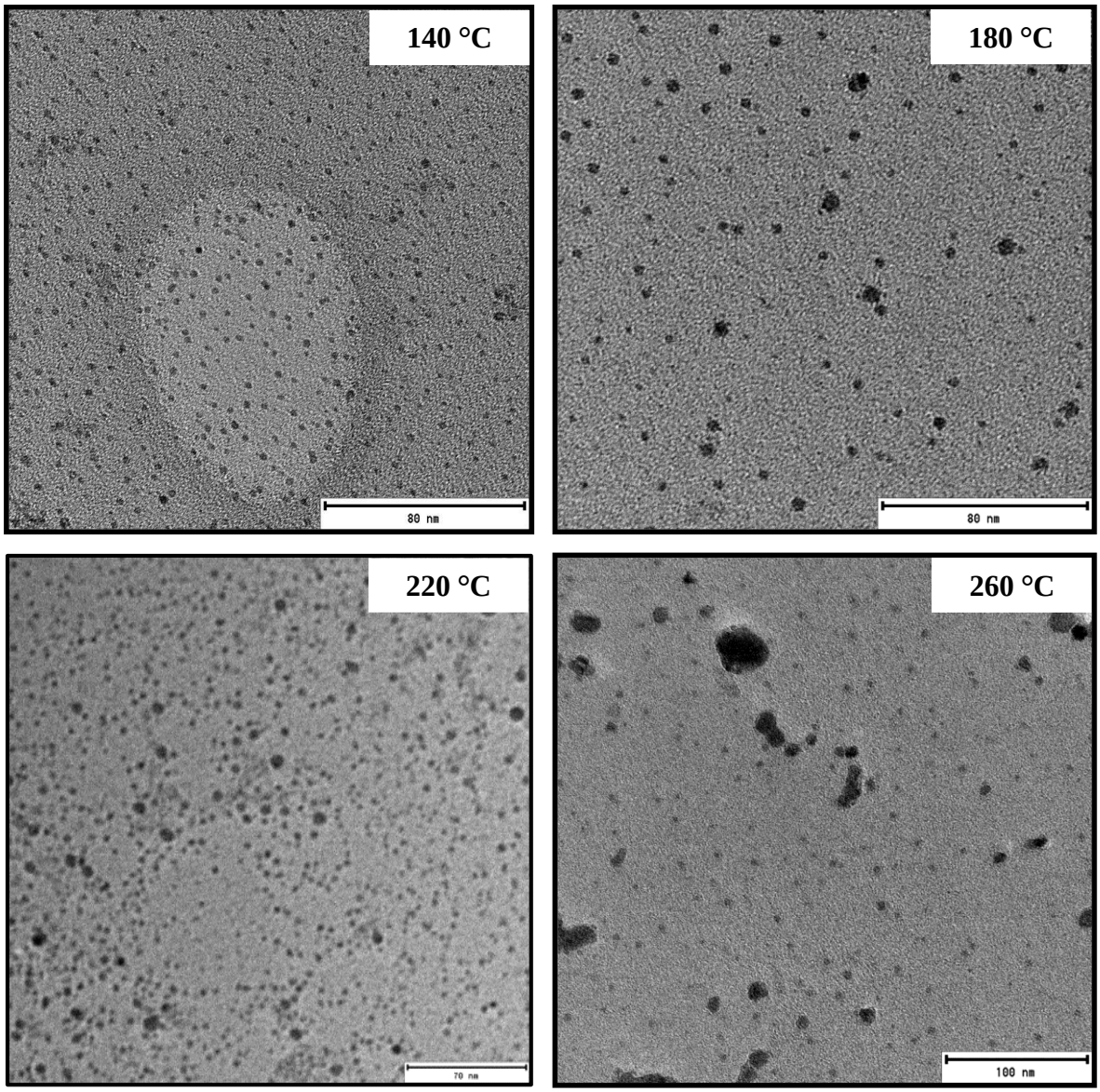

Fig. 3.9: TEM images of copper selenide nanocrystals synthesized at different temperatures.

The sizes and morphologies of the as-synthesized nanoparticles are shown in Fig. 3.9 and the size distribution histograms are shown in Fig. 3.10. All particles were spherical in shape. A steady increase in size was observed as the temperature was increased from 140 °C to 180 °C

and 260 °C with the average size 2.3 nm, 3.9 nm and 8.1 nm respectively. The 260 °C sample does however a few big particles. The particles synthesized at 220 °C does deviate a bit from the trend with the particles having an average diameter of 3 nm. This is somehow consistent with the optical data where the optical band gap of these particles was thought to be indirect compared to the others which were direct. The increase in particle sizes with increasing temperature is consistent with Ostwald ripening and is a readily observed trend in nanoparticle synthesis.

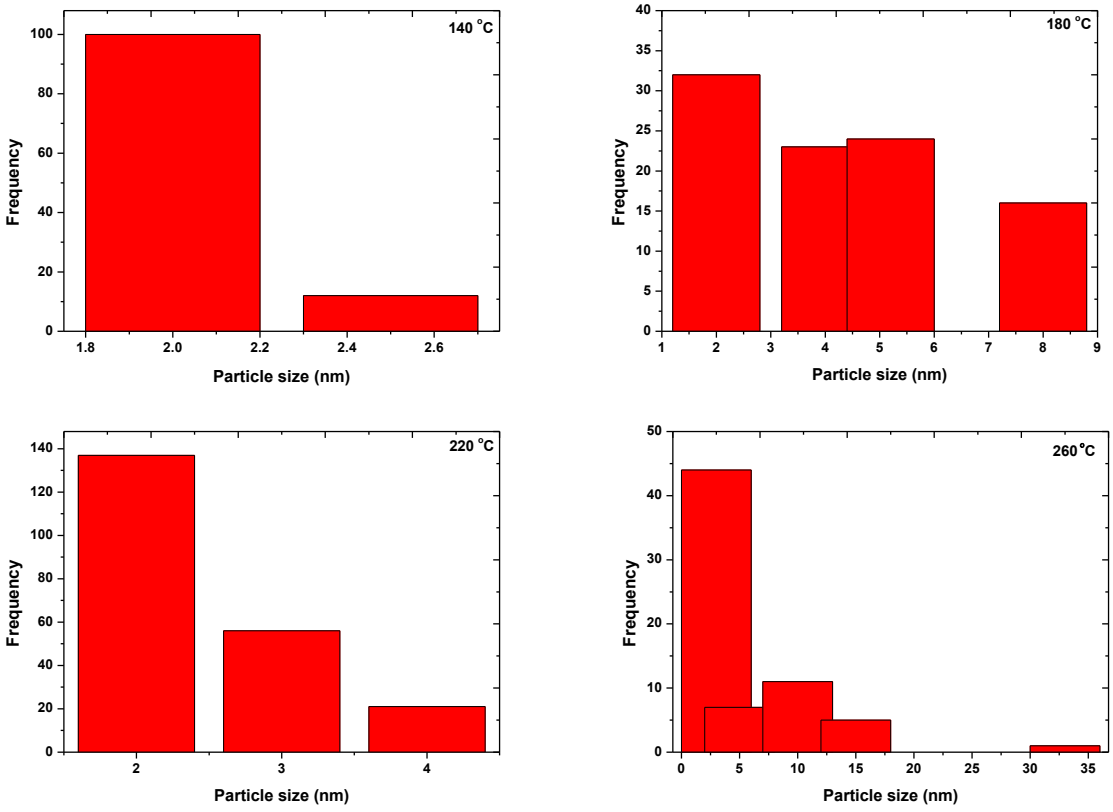

Fig. 3.10: Size distribution plots of copper selenide nanocrystals synthesized at different temperatures.

3.4 Conclusion

Size quantized Cu_2Se nanocrystals were synthesized using the colloidal synthesis method and at different time intervals, different colours of the different sizes were observed similar to the

popular CdSe images. The particle sizes ranged from 2 nm to 7 nm. By controlling the size of these nanocrystals, the band gap was engineered. Temperature also had an effect on the size of the particles with bigger sizes obtained as the temperature was increased. The most interesting thing is that Cu_2Se nanocrystals are quite resistant to changes with the size marginally increasing with increasing time and temperature. This therefore makes it quite useful for applications. The work shows that these nanoparticles can be used in solar cells and has the potential to improve efficiencies due to the ability to absorb more of the solar radiation spectrum going into the infra-red region. The uniqueness of this finding will aid in improvement of electronic devices of all sorts and more especially in rainbow solar cells as they use a variety of different size nanoparticles and types and with this work one will be able to produce rainbow solar cells of a single source material.

References

[1] C. B. Murray, D. J. Norris and M. G. Bawendi, Journal of American Chemical Society, 115, **1993**, 8706.

[2] M. Darbandi, G. Urban and M. Krüger, Journal of Colloid and Interface Science., 351, **2010**, 30.

[3] D. J. Norris and M.G Bawendi, Physic Review B, 53, **1996**, 16338.

[4] V. M Bhuse, P.P. Hankare, K.M. Gudage, R. Sharma, Journal of Alloy; Compounds, 488, **2008**, 466.

[5] A.M. Herman and L. Fabick, Journal of Crystal growth., 61, **1983**, 658.

[6] F. Rong, Y. Bai, T. Chen and Z. Wenjie, Materials Research Bulletin., 47, **2012**, 975.

[7] K. A. Sablon, J. W. Little, V. Mitin, A. Sergeev, N. Vagidov and K. Reinhardt, Nano Letters, 11, **2011**, 2311.

[8] N. Moloto, H. Puggens, S. Govindraju, B. Rakgalakane and M. Kalenga, Thin Solid Flims, 531, **2013**, 29.

[9] R.A. Laudise, Chemical Engineering News, 28, **1983**, 29.

[10] K. Byrappa, M. Yoshimura, Handbook of Hydrothermal Technology, **2001**, 235.

[11] W. Maret. J-M. Moulis, Metal ions in life sciences, 11, **2013**, 1.

[12] R. Roy, Journal Solid State Chemical, 111, **1994**, 75.

[13] S.K. Haram, K.S.V. Santhanam, M. Numannspallart, C. Levyclement, Material Research Society Bulletin, 27, **1992**, 1185.

[14] H.Okimura, T. Mastsumae, R. Malabe, Thin Solid Films, 71, **1980**, 53.

[15] W. S. Chen, J. M. Stewat, R.A. Mackensen, Applied Physical Letters, 46, **1958**, 1095.

[16] L.F. Gou, C.J. Murphy, Journal of Materials Chemistry, 14, **2004**, 735.

[17] M. Li, W. Zhou. W. Gou, Y. Zhou, Z. Hou, Z. Du, S.W. Chua, Journal of Physical Chemistry. C, 116, **2012**, 26507.

[18] Y. Sun, B. Mayers, Y.N. Xia, Nano letters, 3, **2003**, 675.

[19] W. Ostwald, Z. Physical Chemistry, 37, **1901**, 385.

[20] M. Souilah, A. Lafondn, C. Guilloy-Deudon, S. Harel, M. Evain, Journal of Solid State Chemistry, 183, **2010**, 2274.

[21] S. Deka, A. Genovese, Y. Zhang, K. Miszta, G. Bertoni, R. Krahne, C. Giannini, L. Manna, Journal of American Chemical Society, 132, **2010**, 8912.

[22] C. Wadia, A. P. Alivistos, D.M. Kammen, Environment Science Technology, 18, **2009**, 2072.

[23] A. Rockett, R.W. Birkmire, Journal of Applied Physic, 70, **1991**, 81.

[24] Y. X. Hu, M. Afzaal, M. Malik, P. O Brien, Journal of Crystal Growth, 297, **2006**, 61.

CHAPTER 4

THE EFFECT OF STRUCTURAL PROPERTIES OF Cu_2Se /POLYVINYLCARBAZOLE NANOCOMPOSITES ON THE PERFORMANCE OF HYBRID SOLAR CELLS

4.1 Introduction

There has been a constant drive for cost effective photovoltaics since the fabrication of the first solar cell [1]. A number of technologies have since been developed as alternatives for p-n junction silicon solar cells [2]. Amongst these technologies, organic solar cells offer much promise in reducing the costs. This is due to their compatibility with solution based roll to roll manufacturing hence making them applicable in products with thin film, flexible and light weight features. Currently, state of the art bulk heterojunction solar cells involves the use of conductive polymers as donors and fullerenes as acceptors. These devices have achieved power conversion efficiencies (PCE) of just over 10% [3]. However there has been a rather slow growth to the efficiencies due to a number of factors affecting these devices. Among these challenges is the low open circuit voltage (V_{OC}) [4]. There is competing arguments as to what factors affect the V_{OC}; some researchers attribute the V_{OC} to the mere difference of the work functions of the two metal electrodes. Others to the morphology of the active layer or the electrochemical potential of the cathode (poly(3,4-ethylenedioxythiophene):poly(styrenesulfonate) (PEDOT:PSS) [5-7].

Replacing the fullerenes with inorganic nanocrystals is thought to be one way of circumventing some of the problems [8]. This results in the so-called hybrid solar cells. Although the efficiencies of hybrid solar cells are lagging the fullerene based devices, it is theoretically

envisaged that these may surpass the efficiencies because of their intrinsic properties such as tunable band gaps, high absorption coefficiencies and high carrier mobilities [9]. In addition, it is possible to synthesize nanocrystals with elongated and branched morphologies resulting in desirable exciton dissociation and charge transport properties [10, 11]. A number of studies using CdS and CdSe as the acceptor material have been conducted due to the established synthetic methods and thorough understanding of the properties of these materials [12, 13]. Additionally, several studies have been reported for improving the performance of polymer/CdSe hybrid solar cells such as the varying of the size and shape of the nanocrystals [14, 15], through surface modification of the nanocrystals [16-18] as well as polymer end-group functionalization [19], and thin-film nanomorphology control [20].

Herein, we investigate a similar type of material to CdSe however we replace the toxic cadmium with a widely available and non-toxic copper. If one should think of industrial scale application, copper selenide then becomes a better alternative. Copper selenide is a semiconductor that exists in many crystalline phases including monoclinic, cubic, and hexagonal and can possess various stoichiometric ratios such as CuSe, Cu_2Se, $CuSe_2$, and Cu_2Se_3. It is reported that Cu_xSe_y has a direct and indirect band gap of 2.2 eV and 1.4 eV respectively [21]. The interest in employing copper selenide stems from its various reported applications such as thin-film photovoltaics, optical filters and dry galvanic cells (as solid electrolytes) [22, 23].

The morphology of the active layer in hybrid solar cells plays an important role hence several efforts to perfect this has been undertaken. Architectures vary from bi-layer structures [24] to bulk heterojunctions [25] to nanorods arrays [26] however common to all is the need to have good interfacial interaction between the donor and the acceptor materials. Nevertheless, while

interfacial interaction is important, it is critical to have a balance between the filler and the host to harness the properties of the filler whilst keeping the integrity of the host material. Herein we therefore propose the use of polymer nanocomposites to form bulk heterojunction structures and we study the effect of the filler concentration (Cu2Se) on the morphology of the conductive polymer, polyvinylcarbazole (PVK). PVK is a hole transport material (with the hole mobility, μh larger than electron mobility, μel) exhibiting an emission spectrum that owing to the carbazole groups, covers the whole blue region [27]. We further report on the effect of the different polymer nanocomposites with varying filler concentrations on the performance of hybrid solar cells.

4.2 Experimental section

4.2.1 Materials

Copper(I)chloride, selenium powder, trioctylphosphine (TOP), hexadecylamine (HDA), poly vinyl-9-carbazole (PVK) (MW 1,100,000 gmol-1), pyridine, methanol, acetone, isopropanol and poly(3,4-ethylenedioxythiophene)-poly(styrenesulfonate) were all purchased from Sigma-Aldrich.

4.2.2 Synthesis of the Cu_2Se nanocrystals

Cu_2Se nanocrystals were synthesized using a method that we described earlier [28]. In a typical synthesis 0.8 g of CuCl was dissolved in 5 ml of TOP, the solution was stirred for 1 hr at room temperature. 1.0 g of Se powder was dissolved in 5 ml of TOP and the solution was also stirred for 1 hr at room temperature. About 5 g of HDA was heated under N_2 gas to 100 °C. Thereafter the TOP-Se solution was added to the HDA and the temperature was increased to 220 °C. At 220 °C the TOP-CuCl solution was added to the reaction flask and a temperature drop was observed. The temperature was then increased to 220 °C and then the timer was started.

Aliquots at 2, 4, 6, 8 and 10 min were then taken. The nanocrystals were flocculated by the addition of methanol. The resultant crystals were then washed several times with hot methanol and the powders were collected by centrifugation and they were allowed to dry in air.

4.2.3 Synthesis of Cu_2Se/PVK nanocomposites

Cu_2Se nanocrystals were first dispersed in pyridine to exchange the long-chained HDA with a shorter pyridine ligand. The nanocrystals were then flocculated from the pyridine solution by the addition of methanol and subsequently washed several times with methanol and dried at room temperature. The dried powders were then dispersed in chloroform. PVK was subsequently also dissolved in the common solvent chloroform. The two chloroform solutions were mixed and allowed to stir for 30 min at 70 °C. The resultant composite was flocculated by the addition of methanol and collected through centrifugation. The amount of the nanocrystals was varied (10, 20, 30 and 50 wt.%) to give the desired composition of the nanocomposite.

4.2.4 Fabrication of the hybrid solar cells

The structure of the devices consisted of the following layers of films: ITO/PEDOT-PSS/Cu_2-Se-PVK nanocomposite/aluminium. The substrates were routinely cleaned by sequential ultrasonication in acetone, isopropanol, and de-ionized water and then dried in air for 20 min. Aqueous PEDOT-PSS dispersions were spin-coated on the substrates and then annealed at 150 °C for 30 min forming thin films with a thickness of about 55 nm. The nanocomposite layers (25 mg/ml) were spin coated at 3000 rpm, dried and annealed at 150 °C for 30 min resulting in a thin film coating of ~200 nm. The top Al contacts were sputtered through a shadow mask to generate an array of patterned electrodes. The Al was deposited by thermal evaporation in high

vacuum of better than 5×10^{-5} Pa at a rate of about 0.2 nm/s. The final area of each device was 0.08 cm^2 and was defined by the overlap between the top ITO and bottom Al electrodes.

4.2.5 Instrumentation

The morphology of the nanoparticles and nanocomposites was determined on Technai G^2 TEM Spirit operated at 200 kV. SEM analysis was performed on FEI Nova Nanolab 600 FIB/SEM instrument operating at 30 kV. The samples on a carbon tape were coated by a gold-palladium layer before the analysis. A Brüker Tensor 27 Fourier Transform Infrared spectrometer was used to analyse the surface functionalities and the type of functional groups present on the materials. Thermogravimetric analysis (TGA) was performed with a Perkin-Elmer STA6000 using nitrogen as the purge gas and a heating rate of the 10 °$Cmin^{-1}$. The flow rate of the purge gas was kept at 20 $mL.min^{-1}$. A Varian Cary Eclipse (Cary 50) UV-VIS spectrophotometer was used to carry out the absorption measurements. A Varian Cary Eclipse EL04103870 fluorescence spectrophotometer with a medium PMT voltage at an excitation wavelength of 300 nm was used to measure the photoluminescence (PL) of the samples. For both spectral analyses, the powders were dissolved in chloroform and placed in quartz cuvettes (1cm path length). The thin film thicknesses were determined by a Filmetrics F20 instrument. The device performances were characterized under AM1.5G 100 mW/cm^2 illumination in a laminar flow cabinet.

4.3 Results and discussion

The morphology and the extent of interaction of Cu_2Se with PVK was studied using electron microscopy. Fig. 4.1 (a) shows the TEM micrograph of the as-synthesized Cu_2Se nanocrystals. The nanocrystals are spherical with an average size of ~3 nm. The prepared nanocrystals were first stripped off of the long alkyl chained amine HDA, by refluxing in pyridine. Pyridine is

known to form weak and reversible bonds with the surface of the nanocrystals [30] and therefore the pyridine molecules can be easily replaced by overwhelming the nanocrystals with polymer molecules. Incremental weight percentages of the nanocrystals to polymer are reported. The 10% addition of Cu_2Se was the minimum amount that showed an appreciative difference between the polymer and the nanocomposites. Meanwhile, 50% was selected as it still preserved some of the features of the polymer yet clearly the nanocrystal features were more dominant. Fig. 4.1 (b), (c) and (d) represent the SEM images of the pristine polymer, 10% and 50% nanocomposites respectively. The pristine PVK has a smooth morphology consistent with polymers. As 10% by mass of Cu_2Se is added, a change in morphology is observed and the polymer is broken down into particulates in line with the spherical shape of the nanocrystals. This is further exaggerated by the addition of more nanocrystals (50%) where finer spherical particulates are observed. The TEM micrographs of the composites are shown in Fig. 4.1 (e) and (f). Fig. 4.1 (e) shows the presence of greater percentage of the polymer; the more polymer molecules they are, the more agglomerated the particles whereas when 50% of the polymer is used whilst some agglomeration is observed the extent is less.

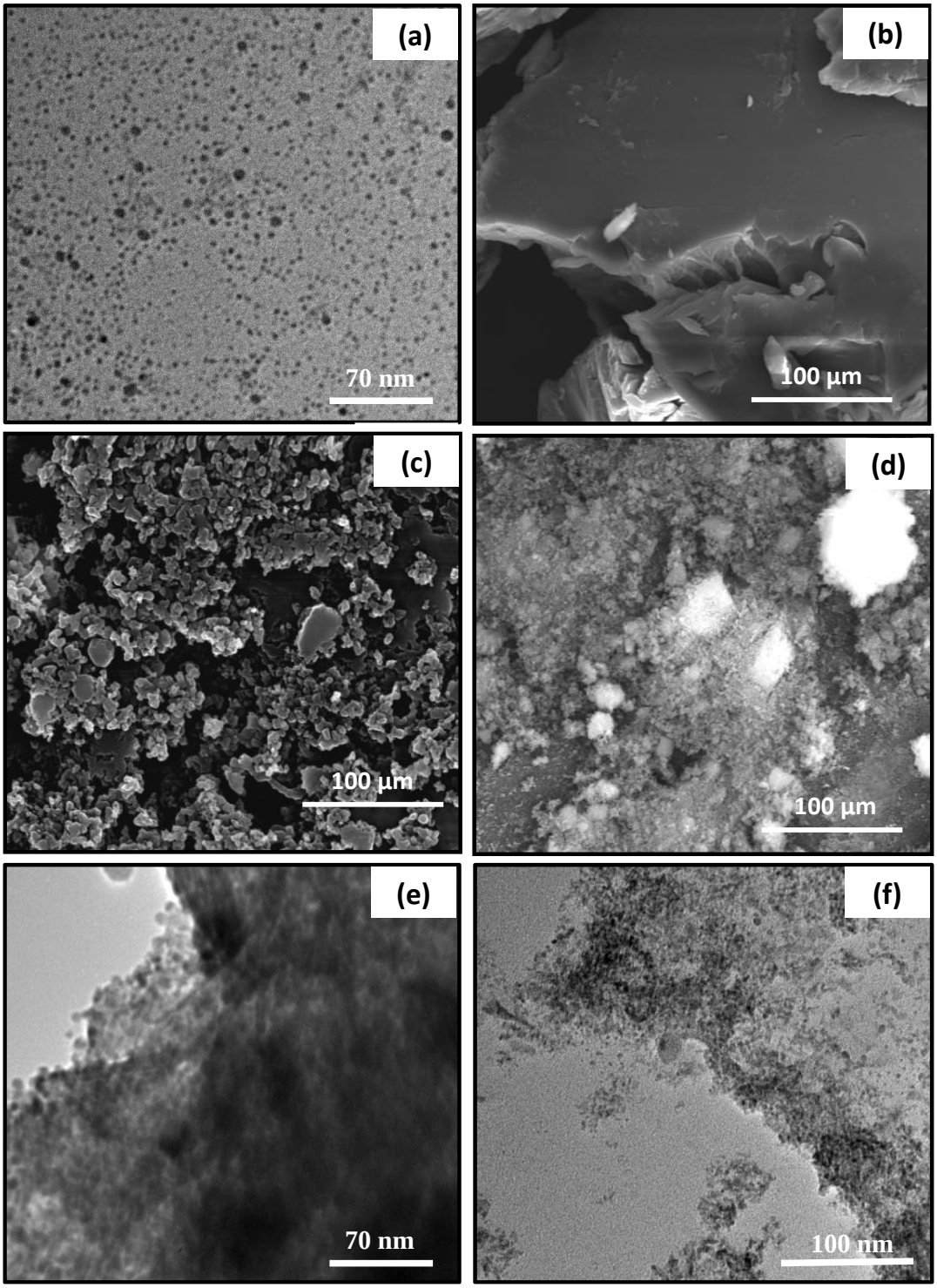

Fig. 4.1: (a) TEM micrograph of Cu_2Se nanoparticles and (b) SEM micrograph of PVK, (c) SEM micrograph of 10% Cu_2Se/PVK nanocomposite (d) SEM micrograph of 50% Cu_2Se/PVK nanocomposite, (e) TEM micrograph of 10% Cu_2Se/PVK nanocomposite and (f) TEM micrograph of 50% Cu_2Se/PVK nanocomposite.

Energy dispersive X-ray spectroscopy (EDX) was done to ascertain the presence of Cu_2Se nanocrystals. The pristine polymer in Fig. 2 (a) of course shows only the presence of carbon and nitrogen. Fig. 4.2 (b) and (c) shows the presence of copper and selenium with the quantitative amount in (c) larger than in (b) consistent with the 10% and 50% addition.

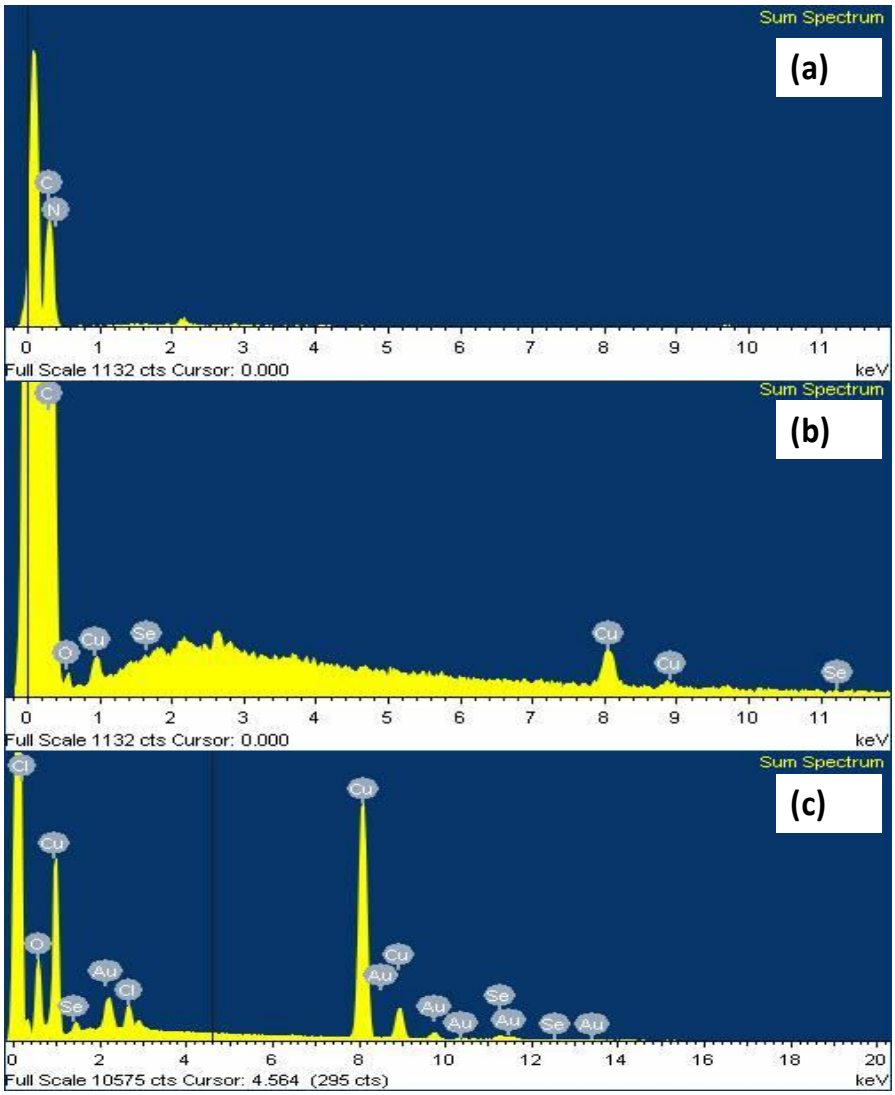

Fig. 4.2: (a) EDX spectrum of PVK, (b) 10% Cu_2Se/PVK nanocomposite and (c) 50% Cu_2Se/PVK nanocomposite.

FTIR spectroscopy can also be a useful tool in determining the extent of the interaction between the polymer and the nanocrystals. Fig. 4.3 shows the FTIR spectra of the pure polymer, 10% and 50% nanocomposites. The FTIR spectrum of the 10% nanocomposite is similar to that of

the pure PVK however a slight shift in the C-H stretching frequency from 3060 cm^{-1} for the pure PVK to 2981 cm^{-1} for the nanocomposite as well as the enhancement of the peak is observed. This therefore suggests that the integrity of the polymer is maintained nevertheless some interaction between the polymer and the nanocrystals is still evident and this bodes well with the morphology observed in the SEM and TEM images. The FTIR spectra of 20% and 30% nanocomposites are shown in the supporting information in Fig. 4.1S. While there are appreciable differences between the spectrum of the pure PVK and that of the nanocomposites, the two extreme cases (10% and 50%) were chosen as the difference in properties would be more pronounced. Fig. 4.3 (c) depicts the spectrum for the 50% addition of Cu_2Se. The characteristic frequencies for PVK are absent, suggesting a complete breakdown of the polymer structure. This is consistent with the fine particulates observed in the SEM and TEM images.

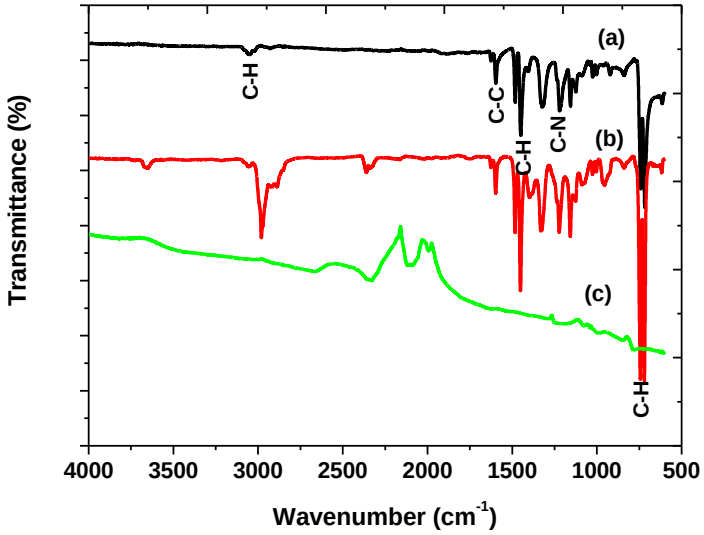

Fig. 4.3: (a) FTIR spectrum of PVK, (b) 10% Cu_2Se/PVK nanocomposite and (c) 50% Cu_2Se/PVK nanocomposite.

To further study the structural integrity of the nanocomposites, TGA analysis was performed. Fig. 4.4 shows the TGA curves of the pure polymer and the nanocomposites. Fig. 4.4 (a) shows

a typical TGA for PVK where the first degradation step is associated with the loss of water and other volatiles that might be present followed by the degradation of the polymer to carbon and then complete decomposition above 450 °C. The addition of the nanocrystals results in an improvement of stability of the polymer beyond 600 °C and of course the residual remains are attributed to the Cu_2Se nanocrystals. The more Cu_2Se nanocrystals added (Fig. 4.2S shows the 20 and 30% nanocomposites), the more thermally stable is the composite as shown in Fig. 4.4 (c).

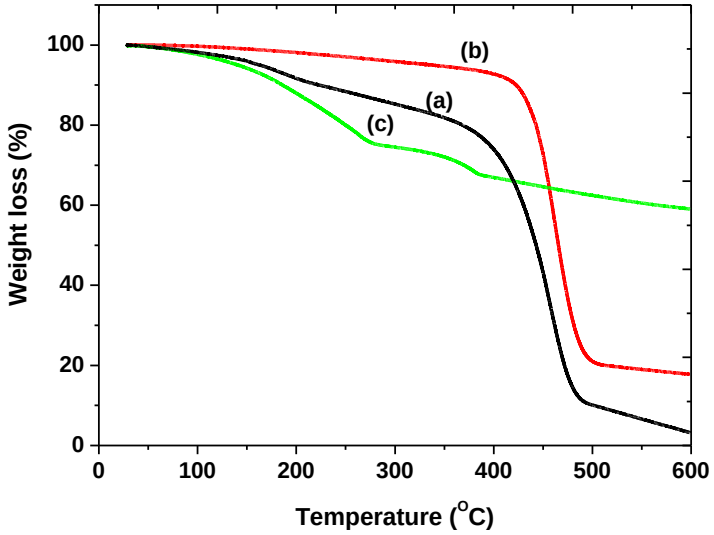

Fig. 4.4: TGA curve of (a) PVK, (b) 10% Cu_2Se/PVK nanocomposite and (c) 50% Cu_2Se/PVK nanocomposite.

The optical properties of the HDA-capped Cu_2Se and the nanocomposites are shown in Fig. 4.5. The absorption spectrum of the Cu_2Se nanocrystals shows two well defined excitonic peaks with the band edge located at 795 nm. The band edge is indicative of an indirect band gap transition and is however blue-shifted from the bulk band edge of 886 nm. On the other hand, the photoluminescence spectrum shows a well-defined emission peak with a maximum located at 800 nm and FWHM of 100 nm indicative of a somewhat monodispersed sample. The PVK

shows a characteristic absorption peak at the UV-region and has a broad emission peak covering the entire UV-Vis region. The optical properties of the 10% Cu_2Se/PVK nanocomposite are similar to that of the pure PVK, a trend that has already been shown. However, the photoluminescence spectrum is slightly red-shifted from 390 nm for the pure PVK to 397 nm for the composite. The optical properties of the 50% Cu_2Se/PVK are different from the pure PVK with new peaks being observed. These peaks may be attributed to the Cu_2Se nanocrystals.

The absorption spectrum has peaks in the UV region below 400 nm associated with PVK as well as a shoulder peak depicted in Fig. 4.6 attributed to the Cu_2Se nanocrystals. The peak has an absorption band edge of ~550 nm which is blue-shifted from the one observed for the HDA capped Cu_2Se. This may be because of the stripping of the HDA molecules. The photoluminescence spectrum in Fig. 4.5 also has peaks reminiscent of PVK and Cu_2Se nanocrystals. The peaks have however blue-shifted a bit. This is consistent with the observed morphology of the 50% nanocomposite, i.e. fine particulates. The emission peak with a maximum at 605 nm shown in Fig. 4.6 is attributed to the nanocrystals and is red-shifted from the corresponding absorption band-edge in Fig. 4.6. The optical properties presented in Fig. 4.6 suggest that the average particle sizes of the nanocrystals may have reduced due to the treatment with pyridine and the interaction with the polymer.

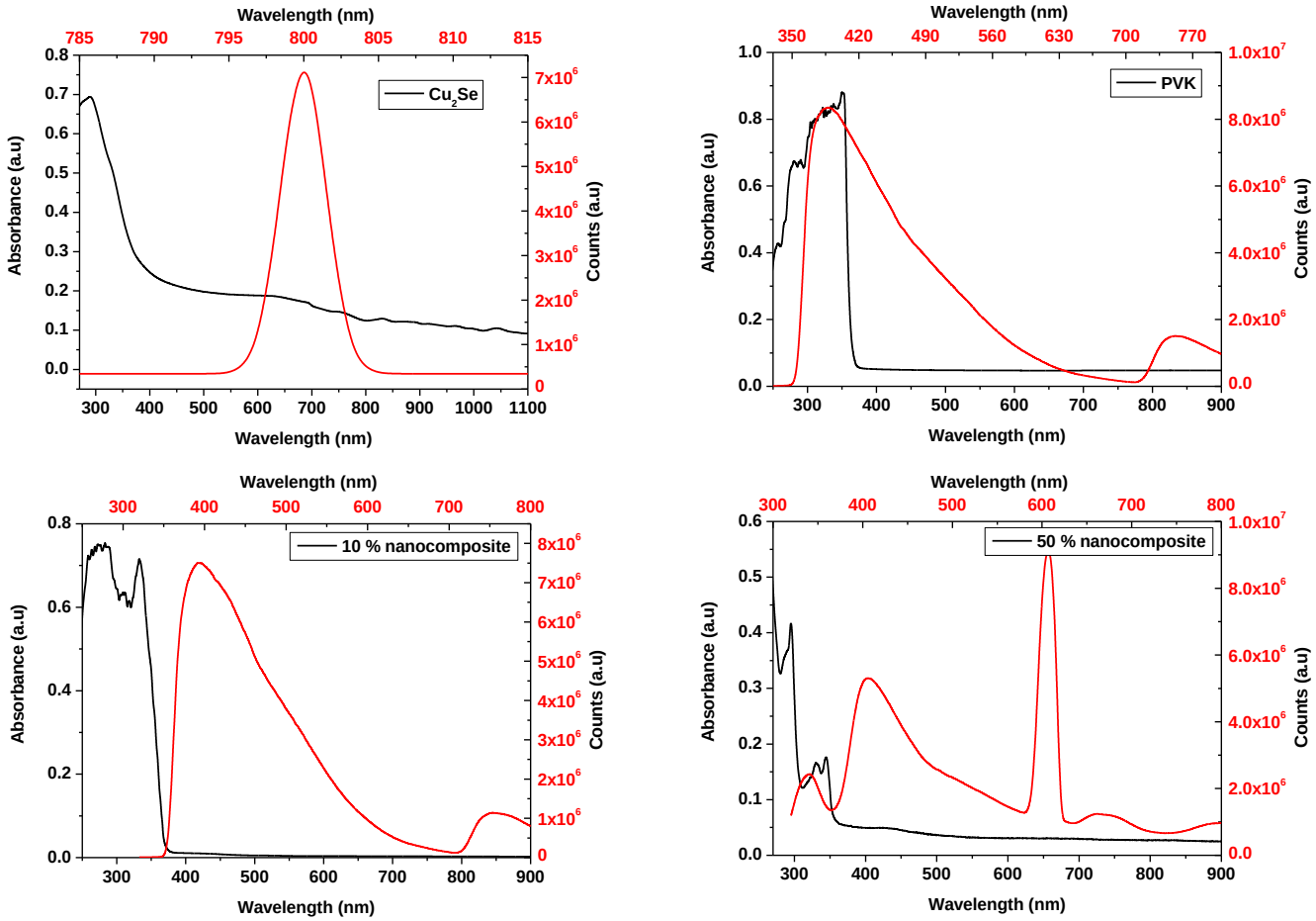

Fig. 4.5: UV-Vis absorption spectra and photoluminescence spectra with excitation at 300 nm for Cu_2Se, PVK, 10% Cu_2Se/PVK nanocomposite and 50% Cu_2Se/PVK nanocomposite.

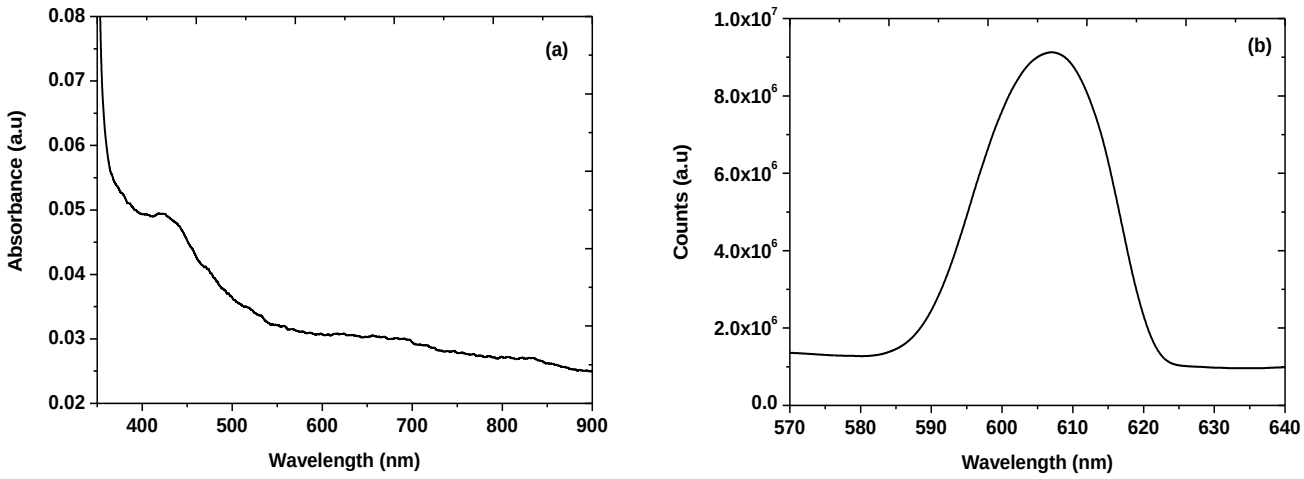

Fig. 4.6: Selected peaks of (a) UV-Vis absorption and (b) photoluminescence spectra of 50% Cu_2Se/PVK nanocomposite.

The synthesized nanocomposites were then tested in a simple device configuration depicted in Fig. 4.7. Due to the energy level offset between the polymer and the nanocrystals, Cu_2Se act as an electron acceptor and PVK as a hole acceptor. The 50% Cu_2Se/PVK nanocomposite showed no photo-response whilst the reduction in the wt. % Cu_2Se showed a steady increase in the photo-response. This could be because of the morphology of the nanocomposite. As shown before, too much addition of the nanocrystals breaks down the polymeric structure hence reducing the pathways for the electrons to travel.

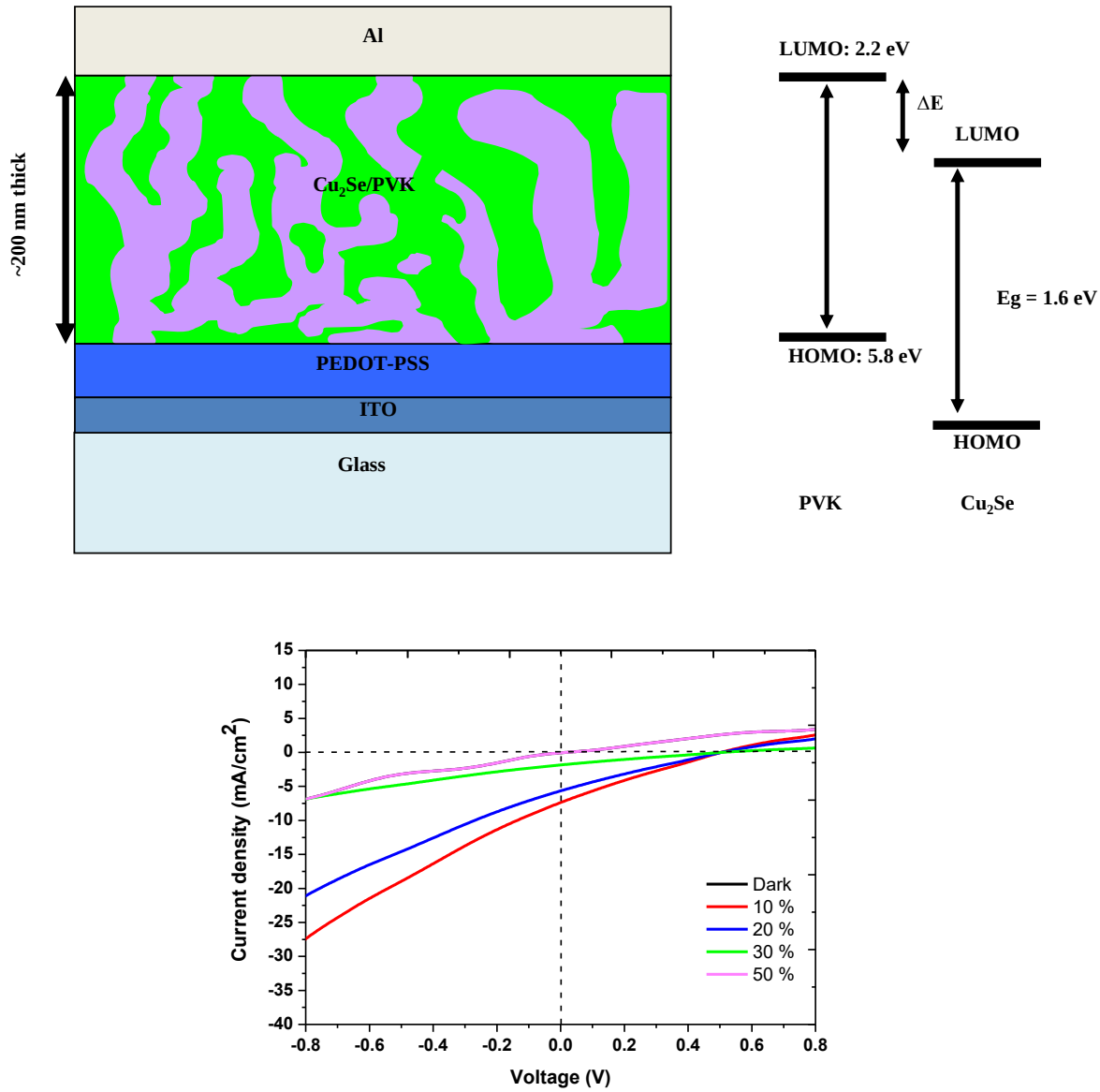

Fig. 4.7: Device architecture and J-V curves of the 10, 20, 30 and 50% Cu_2Se/PVK nanocomposites in the dark and under illumination.

The current density–voltage (J-V) curves of the different Cu_2Se/PVK nanocomposite for the dark and under illumination are reported in Fig. 4.7. The device properties for the different nanocomposites are shown in Table 4.1. The PCE is particularly low when compared to other nanocrystal/polymer hybrid solar cells [9, 20], however it must be said that the commonly reported work use different nanocrystals i.e. CdSe or PbS and other polymer combinations. In

addition, the reported devices have not yet been optimised hence there is scope to further increase the efficiency. The FF is particularly low nonetheless there are several strategies that can be used to increase the fill factor, from inverting the architecture of the hybrid solar cell [29], to the introduction of a buffer layer [30] to name a few. The V_{OC} and J_{SC} can also be improved, amongst other things, by lowering the band-gap of the nanocrystals which can then enable absorption in a longer range; this can be easily achieved by tailoring the size of the nanocrystals. The device with 10 wt. % nanocrystals performed the best with the conversion efficiency of 1.02%. This is attributed to the preservation of the integrity of the polymer thus allow for electrons to flow easier through the polymeric chains. The 50 wt. % nanocomposite devices on the other hand showed no photo-response, consistent with the breaking down of the polymeric chains as seen on the other results.

Table 4.1: Device properties of the nanocomposites

Sample	**V_{OC} (V)**	**J_{SC} (mA/cm^2)**	**FF (%)**	**η (%)**
10% Cu_2Se/PVK	0.50	7.34	22.28	1.02
20% Cu_2Se/PVK	0.50	5.64	22.34	0.79
30% Cu_2Se/PVK	0.50	1.83	22.29	0.25
50% Cu_2Se/PVK	0	0	0	0

4.4 Conclusion

In conclusion, herein for the first time, it has been shown that Cu_2Se nanocrystals can be used in hybrid solar cells as an alternative for CdSe and PbS. It has also shown that while harnessing the properties of the nanocrystals is important, it is also important to keep the integrity of the polymer as the long chains of polymers play a crucial role in charge transport. Hence it has

shown that 10% by weight addition of Cu_2Se improves the properties of PVK and this has resulted in a hybrid solar cell with 0.74% PCE.

References

[1] D. M. Chapin, C. S. Fuller, G. L. Pearson, Journal of Applied Physics, 25, **1954**, 676.

[2] C. J. Brabec, J. A. Hauch, P. Schilinsky, C. Waldauf, MRS Bulletin, 30, **2005**, 50.

[3] Y. Liang, Z. Xu, J. Xia et al., Advanced Materials, 22, **2010**, 135.

[4] M. C. Scharber, D. Muhlbacher, M. Koppe et al., Advanced Materials, 18, **2006**, 789.

[5] C. J. Brabec, A. Cravino, D. Meissner et al., Advanced Functional Materials, 11, **2001** 374.

[6] J. Liu, Y. Shi, Y. Yang, Advanced Functional Materials, 11, **2001**, 420.

[7] H. Frohne, S. E. Shaheen, C. J. Brabec, D. C. Muller, N. S. Sariciftci, K. Meerholz, Chemical Physics and Physical Chemistry, 3, **2002**, 795.

[8] Y. Zhou, M. Eck, C. Veit et al., Solar Energy Materials and Solar Cells, 95, **2011**, 1232.

[9] Y. Zhou, M. Eck, M. Kruger, Energy and Environmental Science, 3, **2010**, 185.

[10] W. U. Huynh, J. J. Dittmer, A. P. Alivisatos, Science, 295, **2002**, 2425.

[11] X. Peng, L. Manna, W. Yang et al., Nature, 404, **2000**, 59.

[12] D. V. Talapin, A. L. Rogach, A. Kornowski, M. Haase, H. Weller, Nano Letters, 1, **2001**, 207.

[13] C. B. Murray, D. J. Norris, M. G. Bawendi, Journal of the American Chemical Society, 115(19), **1993**, 8706.

[14] S. Dayal, M. O. Reese, A. J. Ferguson, D. S. Ginley, G. Rumbles, N. Kopidakis, Advanced Functional Materials, 20, **2010**, 2629.

[15] B. Q. Sun, N. C. Greenham, Physical Chemistry Chemical Physics, 8, **2006**, 3557.

[16] J. S. Owen, J. Park, P.-E. Trudeau, A. P. Alivisatos, Journal of the American Chemical Society, 130, **2008**, 12279.

[17] J. D. Olson, G. P. Gray, S. A. Carter, Solar Energy Materials and Solar Cells, 93, **2009**, 519.

[18] B. C. Sih, M. O. Wolf, Journal of Physical Chemistry C, 111, **2007**, 17184.

[19] J. Liu, T. Tanaka, K. Sivula, A. P. Alivisatos, J. M. J. Frechet, Journal of the American Chemical Society, 126, **2004**, 6550.

[20] Y. Wu, G. Zhang, Nano Letters, 10, **2010**, 1628.

[21] R. Roy, Journal of Solid State Chemistry, 111, **1994**, 11.

[22] H. W. Hillhouse, M. C. Beard, Current Opinion in Colloid and Interface Science, 14, **2009**, 245.

[23] F. Lin, G.-Q. Bian, Z.-X. Lei, Z.-J. Lu, J. Dai, Solid State Sciences, 11, **2009**, 972.

[24] C. W. Tang, Applied Physics Letters, 48, **1986**, 183.

[25] H. Hoppe, N. S. Sariciftci, Journal of Materials Research, 19, **2004**, 1924.

[26] S. Gunes, H. Neugebauer, N. S. Sariciftci, Chemical Reviews, 107, **2007**, 1324.

[27] N. Moloto, N. J. Coville, S. S. Ray, M. J. Moloto, Physica B: Condensed Matter, 404, **2009**, 4461.

[28] S. Govindraju, M. P. Kalenga, M. Airo, M. J. Moloto, L. M. Sikhwivhilu, N. Moloto, Optical Materials, 38, **2014**, 310.

[29] X. Guo, N. Zhou, S. J. Lou et al., Nature Photonics, 7, **2013**, 825.

[30] C. Platzer-Bjorkman, P. Zabierowski, J. Pettersson, T. T orndahl, M. Edoff, Progress in Photovoltaics: Research and Applications, 18, **2010**, 249.

CHAPTER 5

COLLOIDAL SYNTHESIS AND CHARACTERIZATION OF AMORPHOUS NIOBIUM SELENIDE

5.1 Introduction

There is growing interest in nanomaterials due to their unique properties compared to bulk materials. The study of "bottom-up" one pot synthesis methods has been increasing due to its simplicity and its cost effectiveness. Colloidal methods have been successful in producing various nanomaterials of different morphologies using different metals and metal salts with organic capping agents [1-2]. Niobium selenides are interesting materials as they show remarkable properties. They can form a number of stoichiometric variations, amongst which, $NbSe_2$ is the most popular and is part of the metal dichalcogenides similar to those of W and Mo [3-4]. However, the compounds of niobium selenide can form at various oxidation states and these compounds can be perturbed particularly in the nano-regime where meta-stable compounds can be synthesized. The most common compounds of niobium selenide are shown in Fig. 5.1. Niobium selenides have been reported to show temperature dependent superconductivity, Peierls instability and charge density wave transport properties [5-6]. As a result, they have found application in batteries, supercapacitors, as polymer fillers as well as thin film devices [7-10].

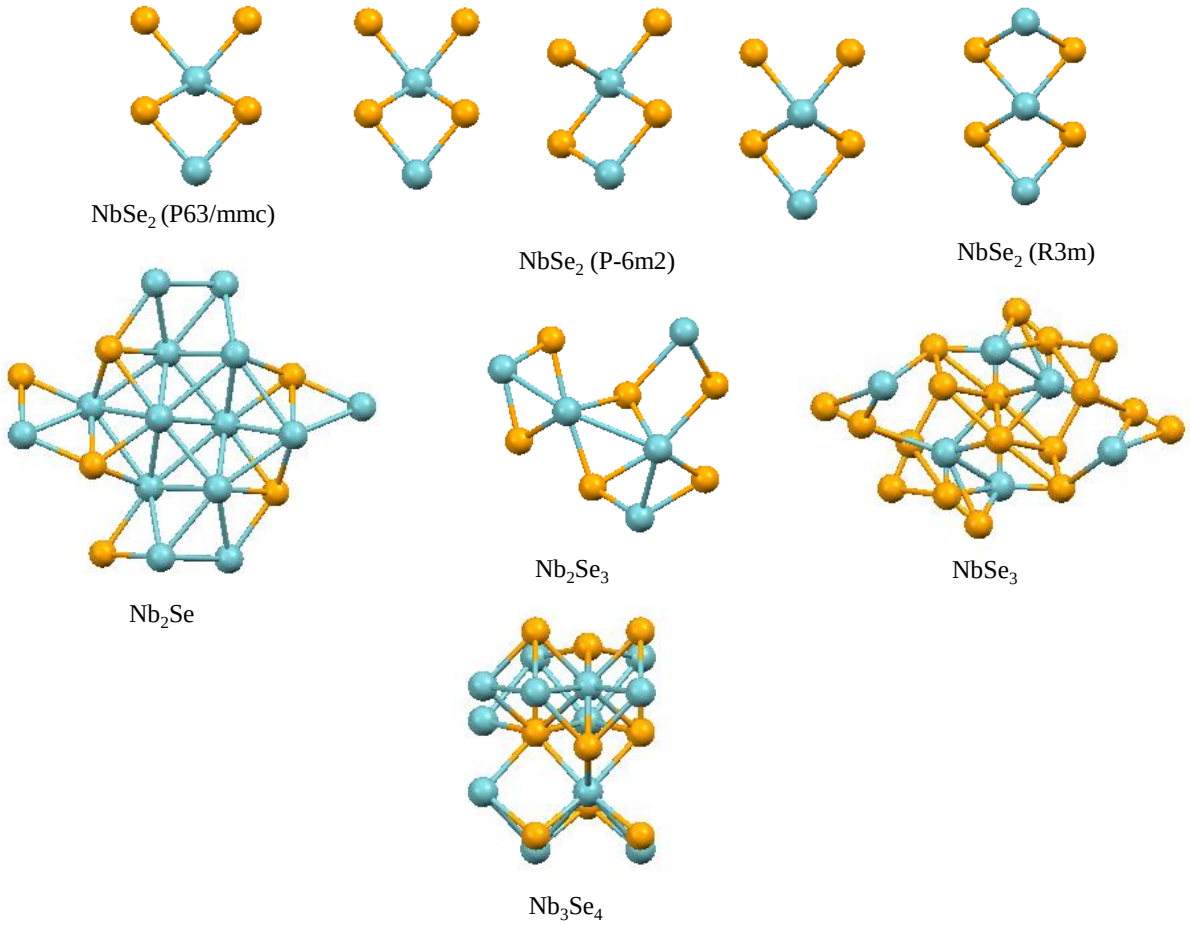

Fig. 5.1: Various compounds of niobium selenide.

Niobium diselenide has been synthesized using various methods. It has been reported that $NbSe_2$ is capable of forming nanotubes and nanofibers via chemical vapour transformation method. In addition, the authors also showed that the nanotubes and nanofibers displayed metallic conductivity [11]. Currently solid state synthesis of niobium diselenide has been successful but has had issues of forming low yields, broad size distribution and has high level of impurities. In addition, solid state method use high temperatures and relatively sophisticated equipment. On the other hand, solution based techniques uses comparatively low temperatures; they have improved morphological control and can result in high yields [12-16]. Sekar et al. reported the first solution based synthesis of 2D nanoplates and 1D nanowires of $NbSe_2$ using a one pot synthesis with niobium chloride and elemental selenium as precursors in oleylamine

and dodecylamine. They concluded that the nanoplates had a thickness of 10-70 nm with lateral dimensions between 500 and 1000 nm. The nanowires that were synthesized were 2-25 nm in diameter with lengths in the micron range [10]. $NbSe_3$ is another common compound of niobium selenide. It has relatively high electronic conductivity ($\sigma = 2.9 \times 10^2\ \Omega^{-1}cm^{-1}$) and has thus found application in batteries as cathode material [17]. $NbSe_3$, just like $NbSe_2$ has been largely synthesized using solid state methods that have resulted in man-sized materials. Stabile et al. reported on the synthesis of single-crystalline $NbSe_3$ nanoribbons by a facile one-step vapour transport process involving the transport of selenium powder onto a niobium foil substrate [18]. Quite evident from literature is that very little work has been done on the synthesis of niobium selenides using the colloidal method. In this study we report on the synthesis of niobium selenide nanospheres via a one pot colloidal synthesis method using hexadecylamine as a capping agent. We further investigate the effect of concentration and annealing temperature on the properties of the resultant nanocrystals.

5.2 Experimental section

5.2.1 Materials

Niobium(V)chloride, selenium powder, trioctylphosphine (TOP), hexadecylamine (HDA), chloroform and methanol were all purchased from Sigma-Aldrich.

5.2.2 Synthesis of the niobium selenide particles

Niobium selenide particles were prepared under inert conditions using a one pot synthesis method. In a typical synthesis 0.8 g of $NbCl_5$ was dissolved in 5 ml of TOP, the solution was stirred for 1 h at room temperature. About 1.0 g of Se powder was dissolved in 5 ml of TOP and the solution was also stirred for 1 hr at room temperature. About 5 g of HDA was heated under N_2 gas to 100 °C. Thereafter the TOP-Se solution was added to the HDA and the

temperature was increased to 220 °C. At 220 °C the TOP- $NbCl_5$ solution was added to the reaction flask and a temperature drop was observed. The temperature was then increased to 220 °C and then the timer was started. Aliquots at 45, 60, 75, 90, 105 and 120 min were then taken. The nanocrystals were flocculated by the addition of methanol. The resultant particles were then washed several times with hot methanol and the powders were collected by centrifugation and they were allowed to dry in air and were later dispersed in chloroform for some characterization. Thereafter the 45 min and 105 min samples were annealed for 3 h at 700 °C. In addition, the concentration was varied by increasing the amount of selenium in the system.

5.2.3 Instrumentation

A Varian Cary Eclipse (Cary 50) UV-Vis spectrophotometer was used to carry out the absorption measurements. A Varian Cary Eclipse EL04103870 fluorescence spectrophotometer with a medium PMT voltage at an excitation wavelength of 250 nm was used to measure the photoluminescence (PL) of the particles. For both spectral analysis, the powders were dissolved in chloroform and placed in quartz cuvettes (1cm path length). XRD patterns on powdered samples were measured on a Bruker MeasSrv D2-205530 diffractometer using secondary graphite monochromated CoKα radiation (λ 1.79 Å) at 30 kV/30 mA. Measurements were taken using a glancing angle of incidence detector at an angle of 2°, for 2θ values over 10 - 90° in steps of 0.026° with a step time of 37 s and at a temperature of 25 °C. The transmission electron microscopy (TEM) was carried out on a FEI Technai T12 TEM microscopy operated at an acceleration voltage of 200 kV with a beam spot size of 20 - 100 nm in TEM mode. The samples were prepared by placing a drop of the suspended nanoparticles in chloroform, on a carbon-copper grid. The grid with the sample was then allowed to dry at room temperature. The scanning electron microscope (SEM) was carried out on a FEI Nova

Nanolab 600 FIB/SEM microscope operated at an acceleration voltage of 30 kV. The samples were prepared by dusting the powder over a sticky carbon tape and coated with palladium.

5.3. Results and discussion

5.3.1 Effect of time on the properties of niobium selenide

Quantum confinement as a function of time has been well studied in nanoparticle synthesis, in particular metal chalcogenides [19]. Herein we report on the synthesis of niobium selenide and their properties as the reaction proceeds with time. Aliquots shorter than 45 min resulted in small nanoparticle yields with no defined shapes, indicative of incomplete nucleation. Hence the results shown here are for samples synthesized for 45 min and longer. The absorption and photoluminescence properties of niobium selenide with respect to time are shown in Fig. 5.2 and summarized in Table 5.1. All samples showed an absorption excitonic peak in the UV-region ranging from 249 nm to 255 nm. Nevertheless, there was slight shift in band edges as depicted in Table 5.1. This was primarily due to the tailing spectra of some of the particles. The tailing of the absorption spectra is indicative of polydispersed samples. The absorption properties were quite similar and showed weak dependence on the time of synthesis. Whilst very few studies report on the optical properties of niobium selenide, S. B. Artemkina and co-workers reported UV-Vis absorption spectra of $NbSe_2$ and $NbSe_3$, where they observed the band edge for $NbSe_2$ in the 400 nm region and that of $NbSe_3$ in the 600 nm region [3]. Given that, it is possible that the synthesized material in this study is that of $NbSe_2$.

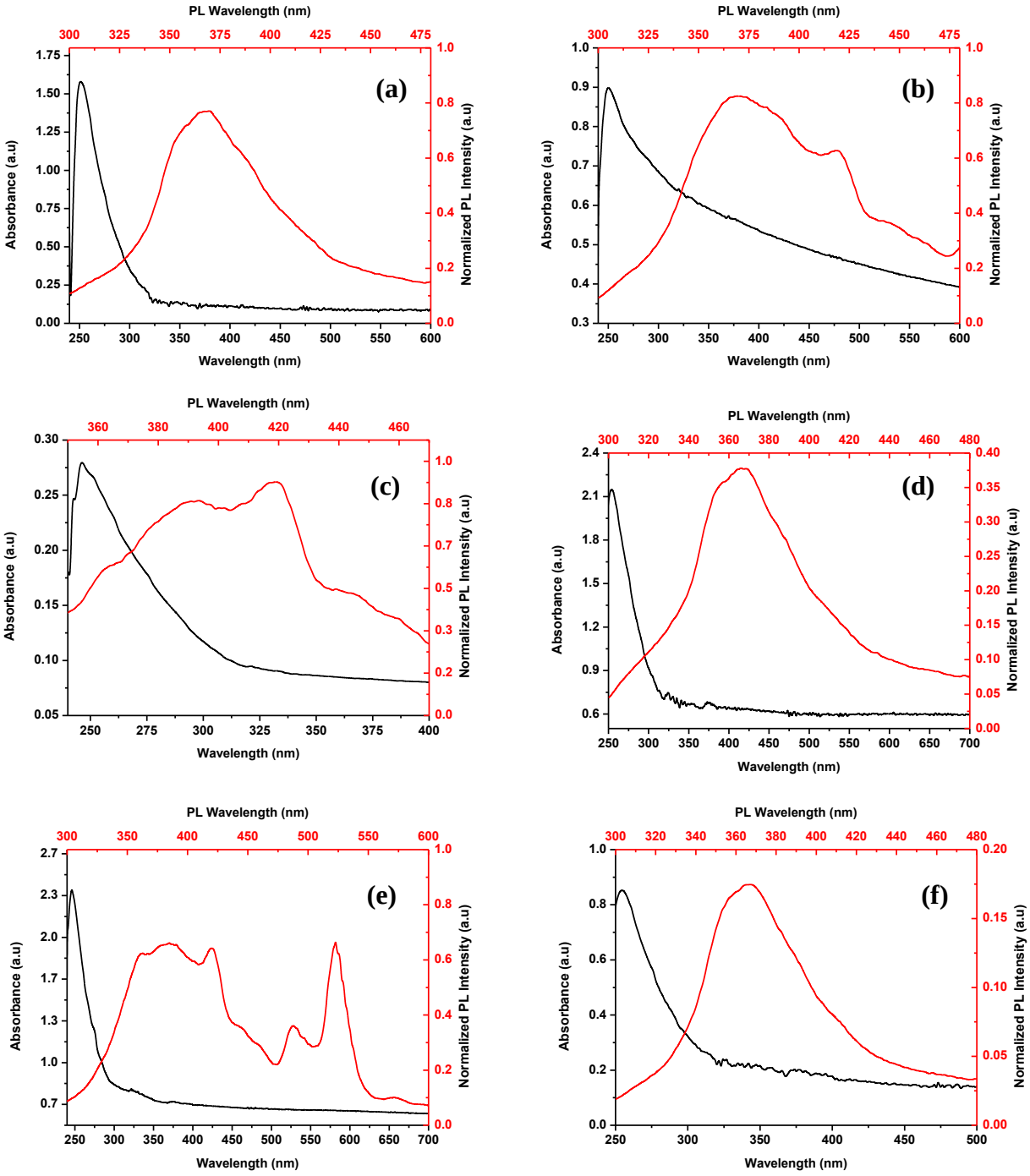

Fig. 5.2: UV-Vis absorption and PL spectra of niobium selenide particles synthesized at (a) 45 min, (b) 60 min, (c) 75 min, (d) 90 min, (e) 105 min and (f) 120 min.

The PL spectra of all samples showed multiple peaks or peak shoulders. This was similar to results reported for molybdenum selenide, another layered metal dichalcogenide. Wang et al.

reported on the PL of molybdenum selenide with multiple peaks and attributed the peaks to the electronic structure of the materials formed, i.e. mono or multi layered and even different morphologies will possess different electronic structures as well as possible defects [20]. Evident from Fig. 5.2 and Table 5.1 is that the different samples have similar emission peaks probably assigned to different electronic transitions.

Table 5.1: Optical data for niobium selenide particles synthesized at 15 min intervals from 45 min to 120 min

Time	UV-Vis excitonic peak (nm)	UV-Vis absorption band edge (nm)	PL peak wavelength (nm)						
			A	B	C	D	E	F	G
45	250	320	357	380	416	-	-	476	-
60	249	-	369	-	420	429	462	-	-
75	249	325	363	392	419	446	460	-	-
90	249	325	356	368	-	-	-	-	-
105	249	330	362	386	420	445	459	488	522
120	255	320	325	344	406	-	-	-	-

The XRD diffraction patterns of niobium selenide synthesized at different times are shown in Fig. 5.3. The XRD patterns showed two broad peaks indicative of the amorphous nature of the samples. The crystallinity of the samples did not improve with prolonged reaction times. This however does indicate the similarity of the samples consistent with the observed optical data.

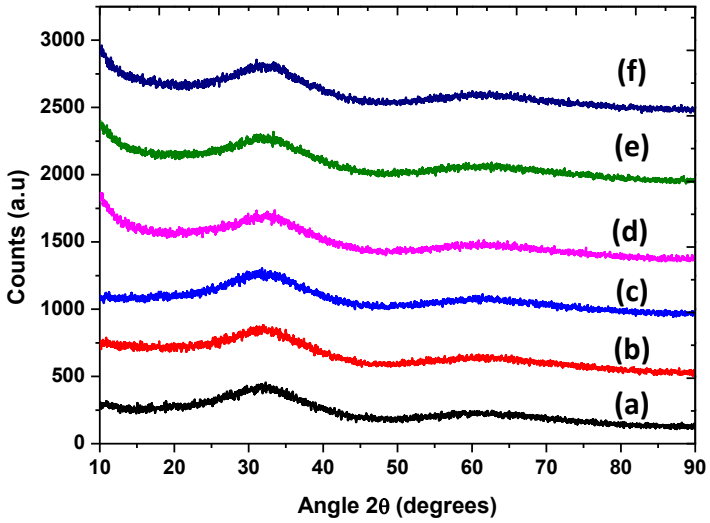

Fig. 5.3: XRD patterns of niobium selenide particles synthesized at (a) 45 min, (b) 60 min, (c) 75 min, (d) 90 min, (e) 105 min and (f) 120 min.

SEM and TEM studies were done to study the morphological properties of the resultant particles. The SEM micrograms are shown in Fig. 5.4. The particles were polydispersed and spherical in shape. Nevertheless, the sample synthesized in 105 min showed the most well defined particles that were less polydispersed. As the time was prolonged to 120 min, the particles appeared to be planar however the degree of polydispersity increased. In addition, there were finer particles deposited on the 120 min samples.

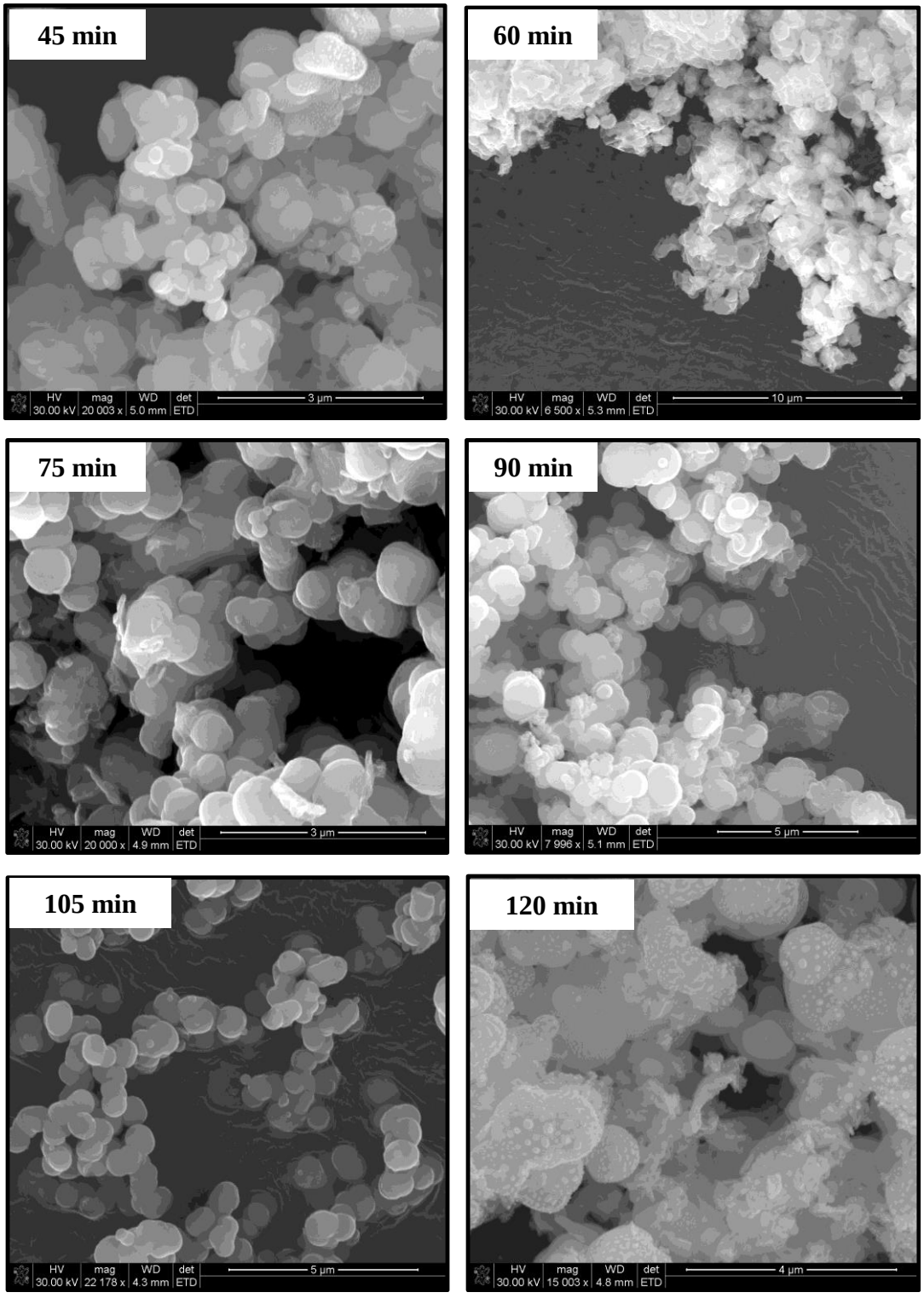

Fig. 5.4: SEM micrographs of niobium selenide particles synthesized at different times.

The TEM images are shown in Fig. 5.5. Large spherical hollow particles were observed for the sample synthesized in 45 min. The average thickness of the shell was 40 nm with the inner

diameter being 120 nm. The presence of hollow particles is indicative of the material being similar to hollow carbon spheres and might be attributed to the presence of oxygen as it was observed from the EDX spectrum (Fig. 5.1S). As the time was prolonged to 60 min, the particles were then polydispersed however the hollow structure was still observed. Further increment of time resulted in solid spheres forming. The particles synthesized after 75 min showed some degree of agglomeration, nevertheless, the average particle size was 220 nm. The 90 min sample was more agglomerated. The 105 min sample showed perfectly spherical particles with an average diameter of 235 nm, however smaller particles were also observed. Another interesting feature that was observed was that when particles overlapped, the particles below were still seen. This is a common feature in carbon nanomaterials such as carbon spheres [21] and this feature is attributed to the folding of thin layer of graphene sheets hence resulting in relatively transparent particles. It is therefore plausible that $NbSe_2$ particles will show a similar feature as it is a layered structure in bulk form similar to graphite, i.e. it is made up of layers held together by weak intermolecular forces. As the time is increased to 120 min, the average size remains 235 nm however the polydispersity of the sample seem to improve. Niobium selenide is usually described as a layered structure and morphologies such as nanoplates and nanodiscs have been previously reported [10]. The emergence of spherical particles in this instance can be possibly attributed to the presence of impurities such as chlorine and oxygen as shown in Fig. 5.1S. In addition, the impurities could be the reason for the poor crystallinity of the samples.

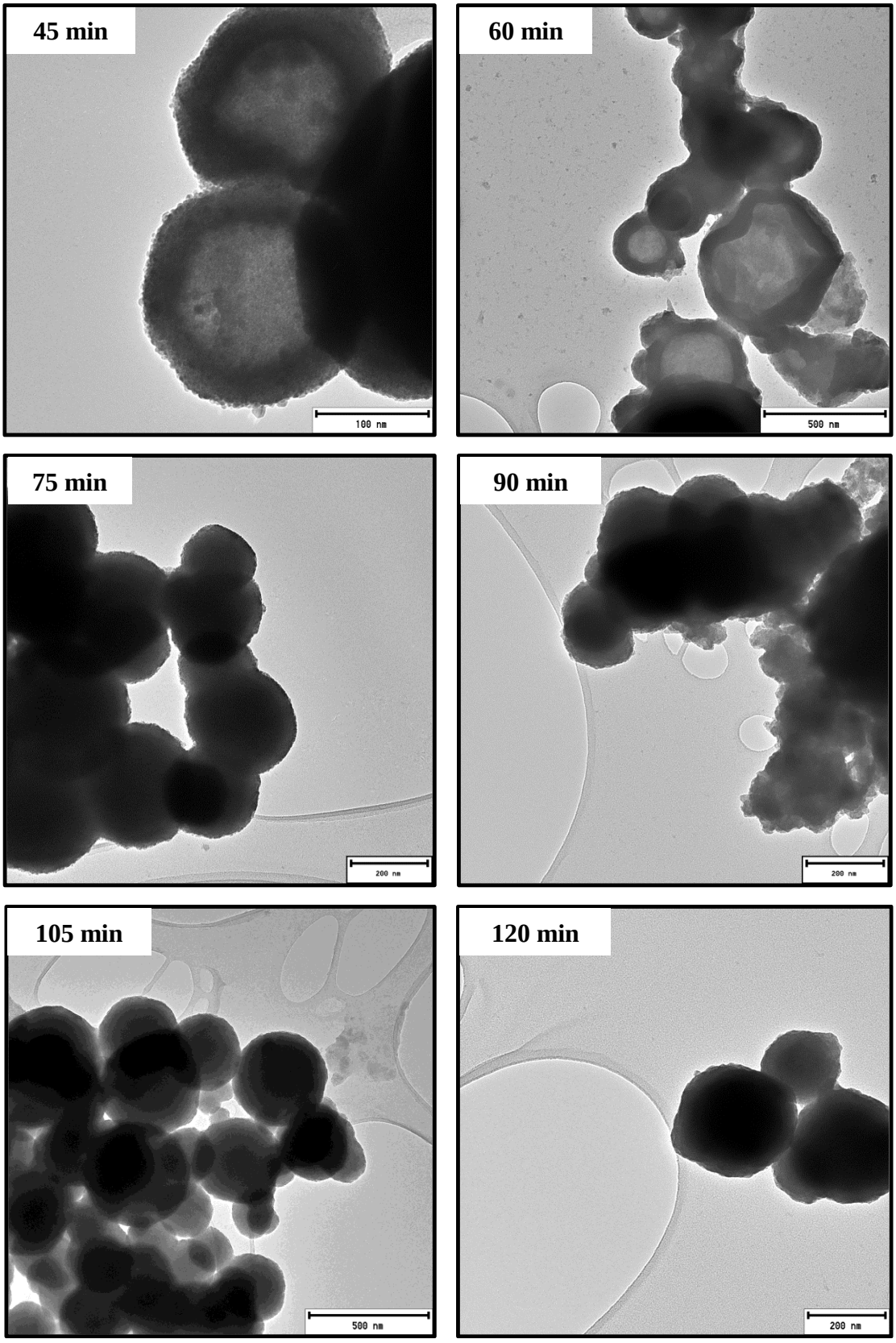

Fig. 5.5: TEM micrographs of niobium selenide particles synthesized at different times.

3.2 Annealing to improve crystallinity of niobium selenide

To try and improve the crystallinity of the samples, two samples were subjected to annealing. The 45 min and 105 min samples were chosen as a result of the hollow structure and the well-defined solid spheres respectively. The X-ray diffraction studies of niobium-selenium systems have long been a subject of research [22]. Niobium selenide has often been synthesized using solid state methods where long reaction time and high temperatures are employed. In binary systems, it therefore becomes possible to systematically study the reactivity between two elements by forming a diffusion couple. This is achieved by putting two bulk pieces of each element together at a well-defined interface. The emergence of amorphous material has been shown to form first in these solid state reactions with the composition near that of the lowest temperature eutectic in a phase diagram [22]. According to Fukuto and co-workers, annealing the amorphous niobium selenide at 600 °C and above, will result in a formation of crystalline $NbSe_2$ [23]. However, such control in nanomaterials synthesized in solution is not easily achievable and metastable compounds may often form. Nevertheless, an attempt to anneal the as-synthesized samples at high temperature was undertaken.

Fig. 5.6 shows the XRD patterns of the pristine and annealed 45 and 105 min samples respectively. Upon annealing in nitrogen at 700 °C, the XRD pattern showed only slight changes with the two broad peaks still being observed however the intensity of the peaks increased slightly. In order to test if indeed niobium was present in the samples, the samples were annealed in oxygen and the obtained XRD patterns were indexed to NbO (Fig. 5.2S). From the obtained data, it was possible to deduce that the amount of selenium present was not enough hence annealing at high temperatures yielded the same sample.

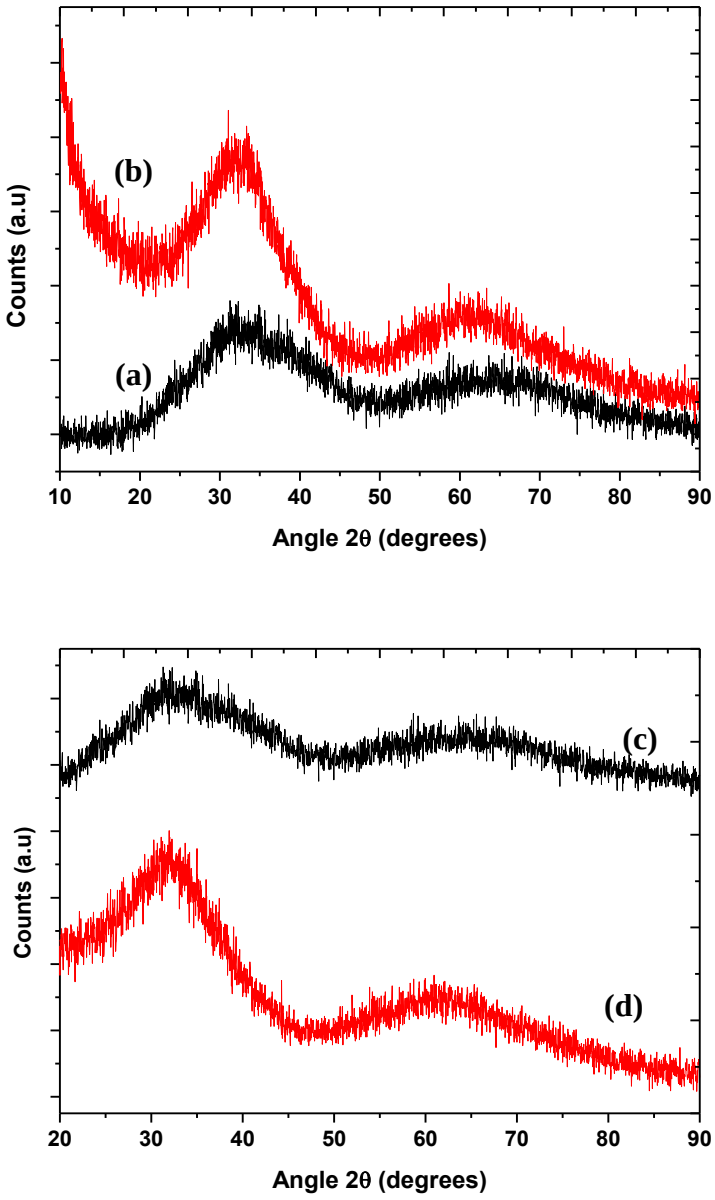

Fig. 5.6: XRD patterns of (a) pristine niobium selenide synthesized at 45 min, (b) annealed 45 min sample at 700 °C for 60 min, (c) pristine niobium selenide synthesized at 105 min, and (d) annealed 105 min sample at 700 °C for 60 min.

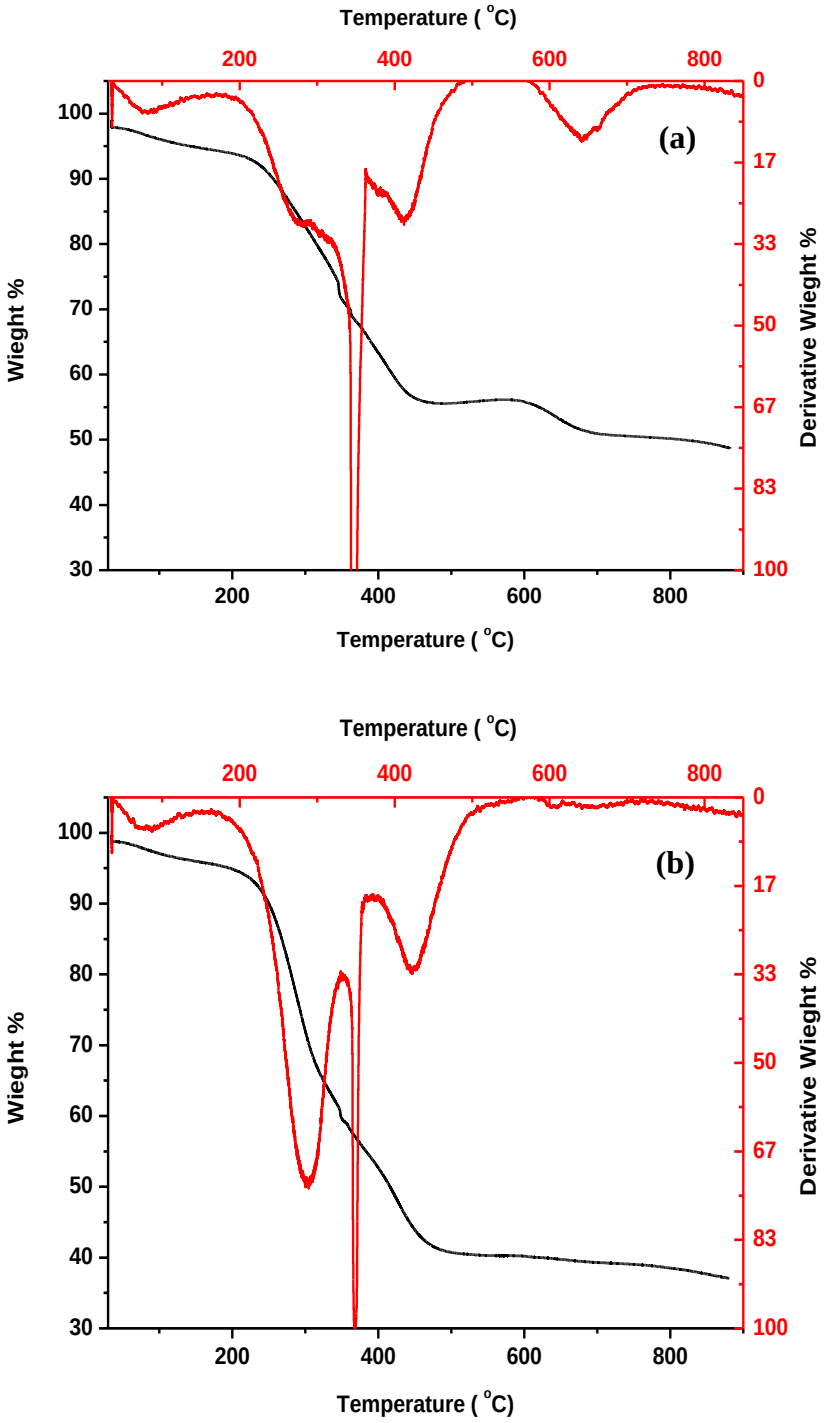

Fig. 5.7: TGA spectra of (a) niobium selenide synthesized at 45 min and (b) niobium selenide synthesized at 105 min done in nitrogen atmosphere.

Nevertheless, thermogravimetric (TGA) analysis was performed to trace the annealing products of the pristine samples. TGA monitors the changes in a substance's mass as a function

of temperature. The TGA spectra are shown in Fig. 5.7. The spectra show similar degradation peaks and this was not surprising as the optical and morphological properties of the two samples were quite similar. The results obtained from the TGA are summarized in Table 5.2.

Table 5.2: Summary of the TGA data

Sample	Temperature (°C)	Weight %	Degradation product
	70	95	CH_3OH
	230	93	$NbCl_5$
45 min	350	72	HDA
	410	56	-
	650	50	Se
	70	97	CH_3OH
	240	92	$NbCl_5$
105 min	350	59	HDA
	420	49	-
	480	42	-

The peak located at 70 °C in both cases is attributed to the removal of methanol, a solvent used in the flocculation and washing of the particles. The boiling point of $NbCl_5$ is about 248.2 °C. The peak located at 230/240 °C can therefore be attributed to the volatility of $NbCl_5$. The surfactant, HDA can sometimes linger on and may not be all removed by the washing with methanol. The boiling point of HDA is reported to be 330 °C therefore it is plausible that the peak at 350 °C can be attributed to the volatility of HDA. The peak at 650 °C can be assigned to elemental selenium. This suggests that unreacted selenium was present. All other peaks cannot be accounted for. From the TGA results, it can be concluded that the samples were

complex with a lot of impurities. Unfortunately, niobium selenide compounds have very high decomposition temperatures, way above the limitation of TGA hence TGA cannot be used to conclusively determine the presence of these compounds. However, it must be noted that in both samples, more than 40 weight% remained above 900 °C suggesting the presence of more stable compounds such as the niobium selenides (melting point of $NbSe_2$ is 1300 °C).

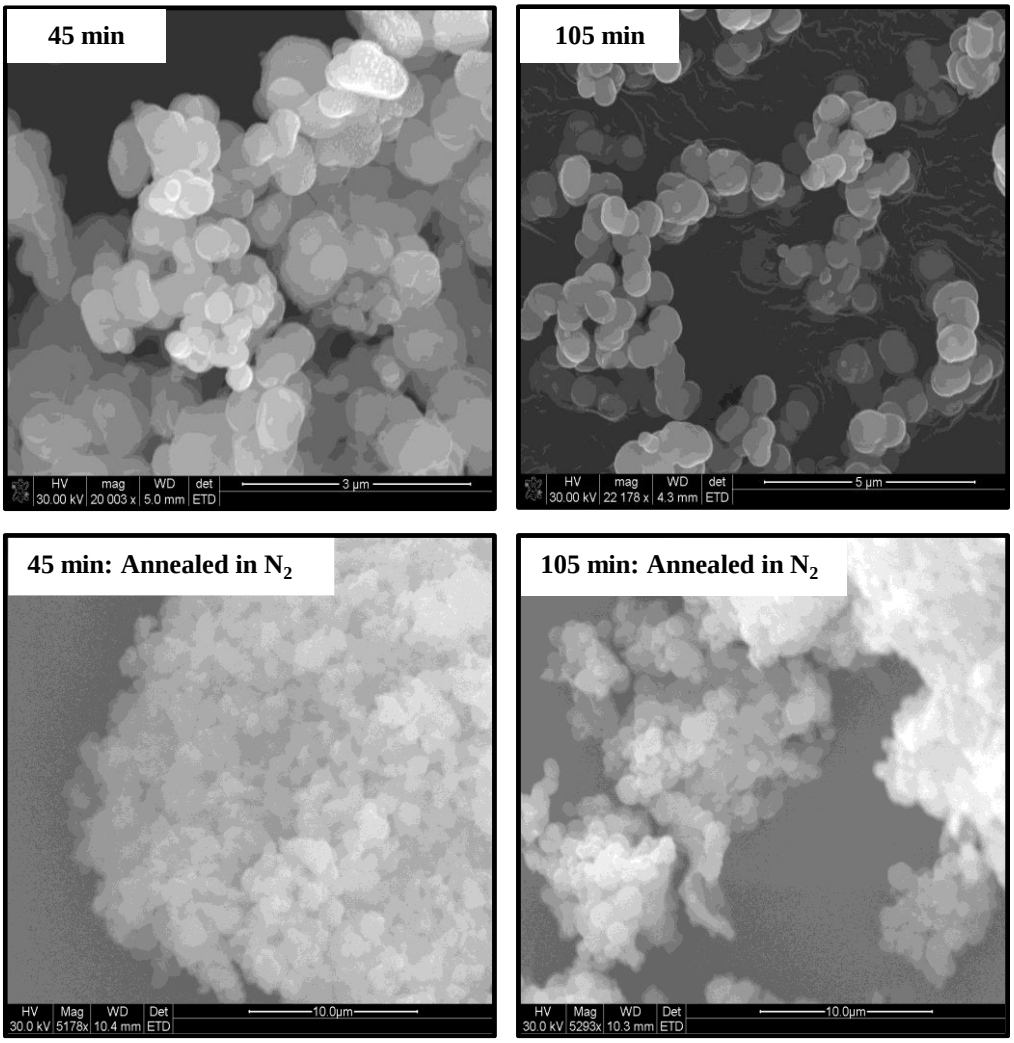

Fig. 5.8: SEM micrographs of the pristine and annealed niobium selenide particles synthesized at 45 min, 105 min and annealed at 700 °C for 60 min respectively.

Fig. 5.8 shows the SEM images of the pristine and annealed samples. Evident from the images is that the annealed samples are more agglomerated. However, no change in morphology is observed.

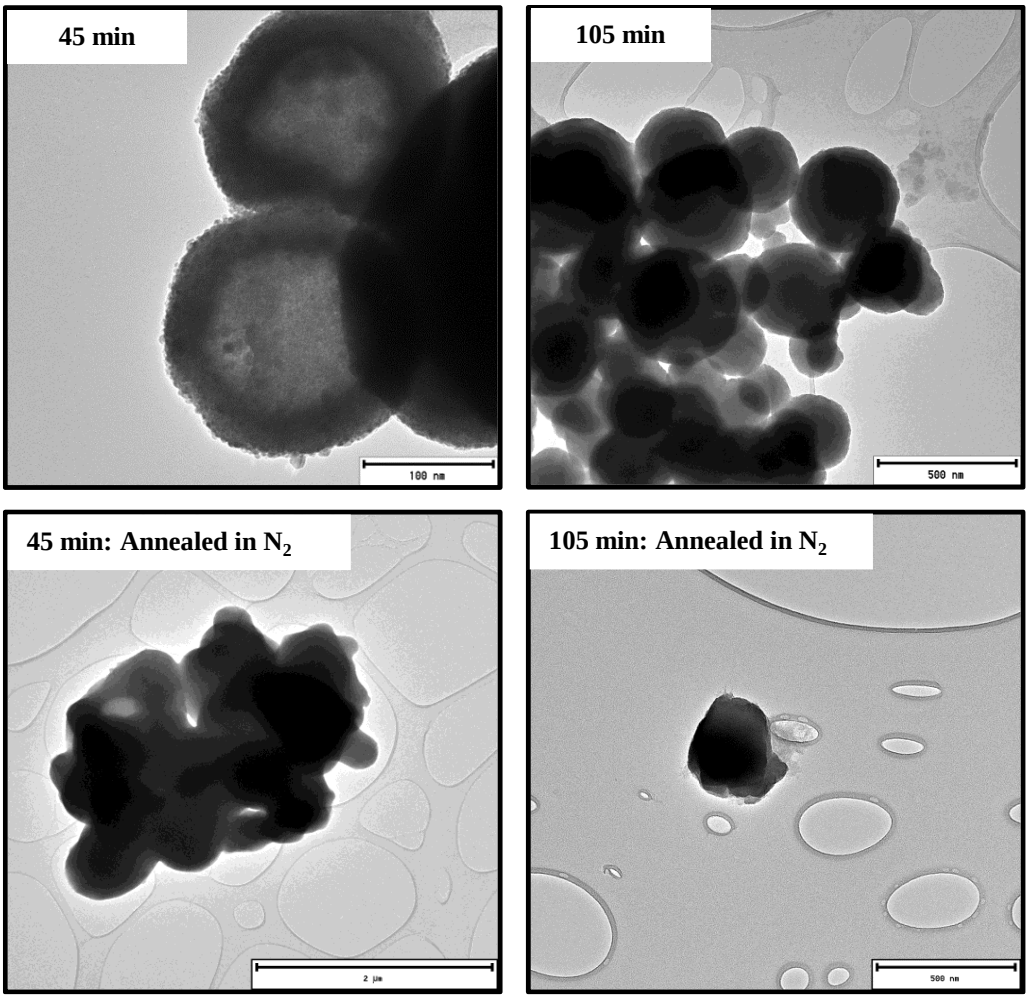

Fig. 5.9: TEM micrographs of the pristine and annealed niobium selenide particles synthesized at 45 min, 105 min and annealed at 700 °C for 60 min respectively.

The TEM images in Fig. 5.9 still suggest agglomeration of the annealed particles. However, some form of deformity is observed. In addition, the hollowness observed in the 45 min sample seems to disappear with annealing.

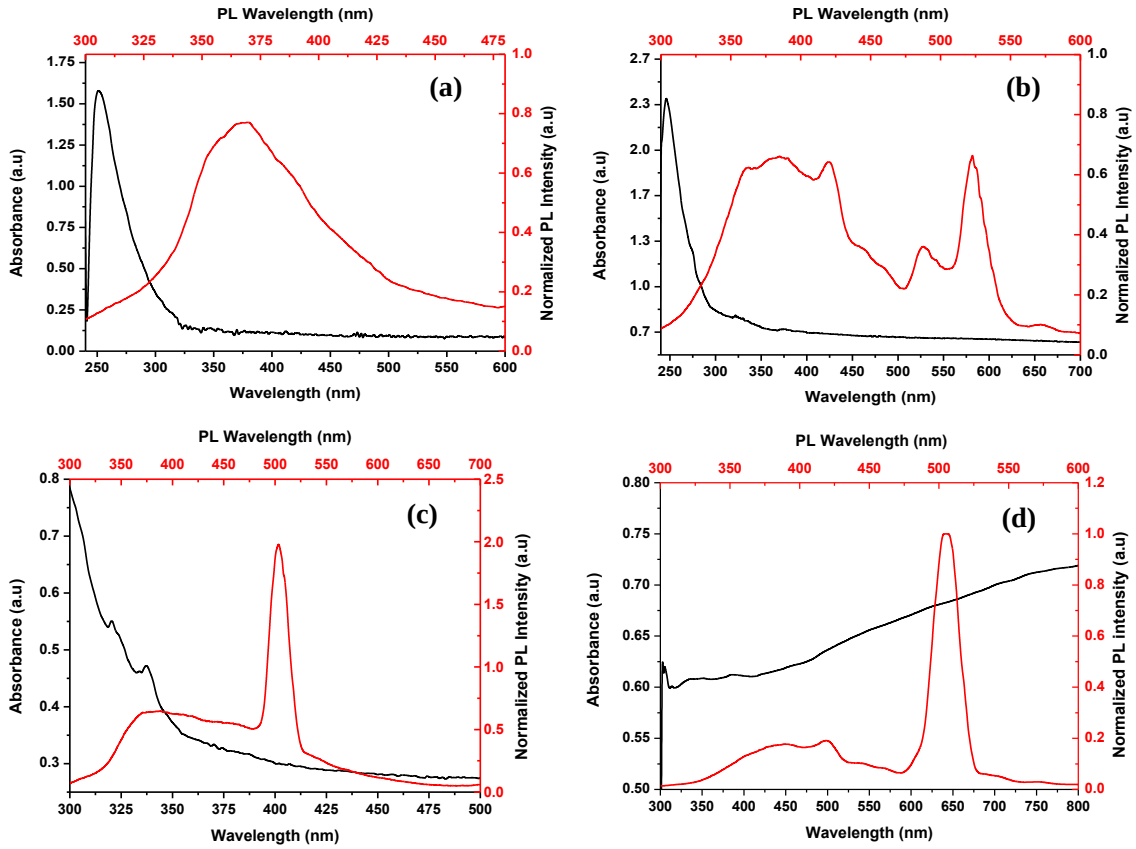

Fig. 5.10: UV-Vis absorption and PL spectra of the pristine and annealed niobium selenide particles, synthesized at (a) 45 min, (b) 105 min and annealed at 700 °C for 60 min (c) and (d) respectively.

The optical properties of the annealed samples are shown in Fig. 5.10. There are noticeable differences between the pristine samples and the annealed samples. Fig 5.10 (a) and (c) represent the 45 min sample before and after annealing. An emergence of two small excitonic peaks is observed for the annealed sample. In addition, there is a slight red-shifting of the absorption band edge to about 400 nm. This suggests a growth in particle sizes. This is attributed to Ostwald ripening where particles grow with increasing temperature. The presence of multiple excitonic peaks might signify that the sample is more polydisperse upon heating. The sharp peak at 500 nm in the annealed sample is the second order excitation peak (excitation was at 250 nm). The remaining peaks are quite similar to the pristine sample suggesting that

the heating did not alter the electronic properties of the sample that much. The peaks may be however much broader suggesting polydispersity. Fig. 5.10 (b) and (d) represents the 105 min sample. The UV-Vis absorption spectrum for the annealed sample is markedly different with strong absorption in the visible and towards the NIR region observed. The change in the absorption spectra may be attributed to the agglomeration as seen on the SEM image. The PL spectrum is like the pristine sample and suggests that there were no changes in the character of the particles. This is quite contradictory to the absorption data and further probing is required.

3.3 Effect of increasing the selenium concentration on the properties of niobium selenide

From the results above, it was clear that the synthesis of niobium (II) selenide was quite complex unlike the oxide counterpart and that a 1:1 $NbCl_5$:Se ratio was perhaps problematic. To synthesize the more common compounds of niobium selenide, i.e. $NbSe_2$ and $NbSe_3$, the mole ratio of selenium was increased accordingly. Fig. 5.11 showcases the absorption and photoluminescence spectra of the different concentration ratios. The UV-Vis absorption spectrum of the 1:1 sample shows an excitonic peak with the band edge located at 325 nm. The 1:2 sample was to try and synthesize $NbSe_2$. As said previously very limited studies have been done on the optical properties of niobium selenide, nevertheless, the UV-Vis absorption spectrum of the 1:2 sample has no excitonic peak, probably signifying a polydispersed sample. The band edge is however located at about 400 nm, like the reported value for $NbSe_2$ [3]. Fig. 5.11 (c) shows a spectrum with a band edge located at 500 nm. This is consistent with the reported results for $NbSe_3$ [3]. From the absorption spectra, it seems that by varying the amount of selenium, it is possible to get the desired products. The PL spectra for all samples were red-shifted from the absorption band edges. The FWHM for 1:1, 1:2 and 1:3 samples were 176 nm, 200 nm and 100 nm respectively. This suggests that the 1:1 and 1:2 samples were fairly polydispersed; with the 1:3 sample the least polydispersed.

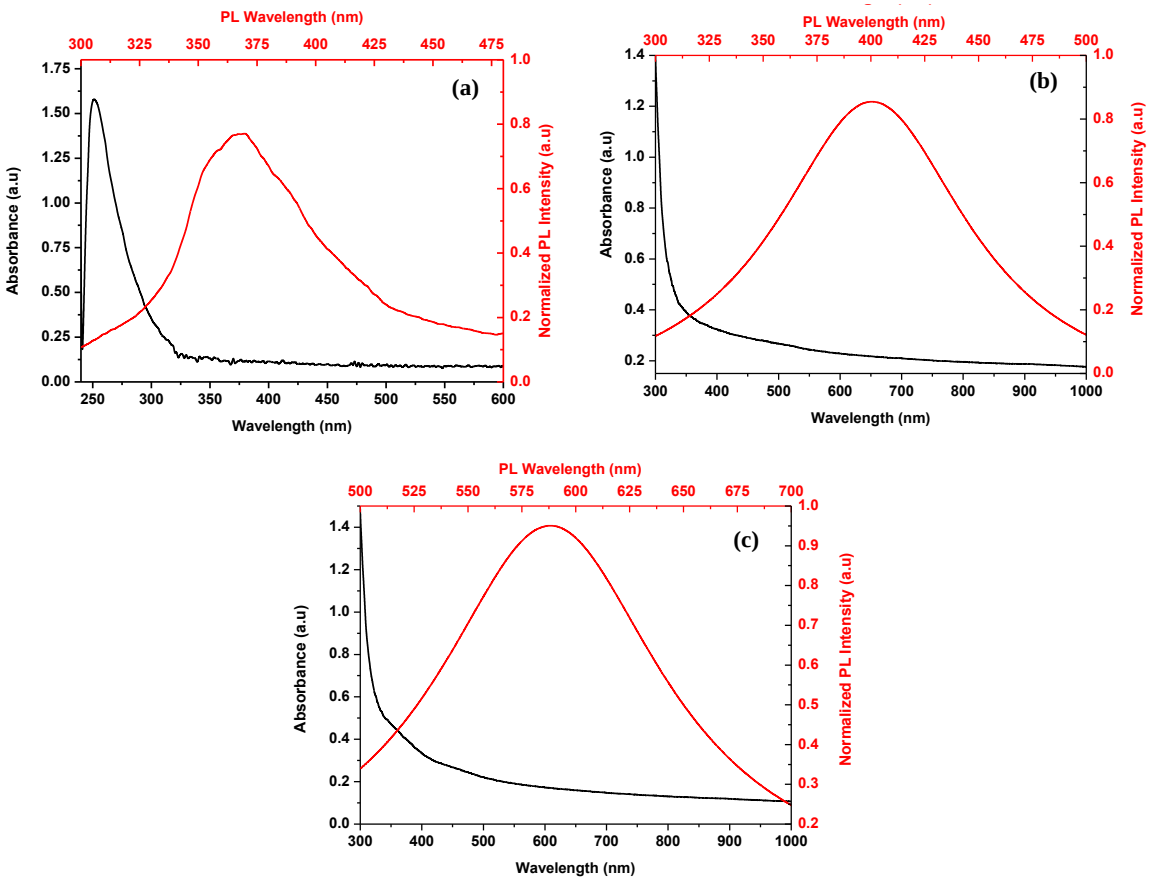

Fig. 5.11: UV-Vis absorption and PL spectra of niobium selenide synthesized at different Nb:Se mole ratios, (a) 1:1, (b) 1:2 and (c) 1:3.

The XRD diffractograms of the as-synthesized samples are shown in Fig. 5.12. The 1:1 sample as stated before shows two broad amorphous peaks and therefore it cannot be confidently assigned to any niobium selenide phase. The 1:2 sample, though showing broad peaks has evidence of crystalline peaks. The XRD pattern was indexed to a hexagonal NbSe2 phase with the peaks at 31°, 37°, 44° and 50° corresponding to the (101), (103), (006) and (105) lattice planes respectively (JCPDS card no.: 65-7464). The 1:3 sample was indexed to a NbSe3 phase with the reflections at 16°, 22°, 35° and 43° corresponding to the (102), (20-3), (20-6) and (213) (JCPDS no.: 34-1106). The other peaks are indexed to Nb_2O_5 suggesting that niobium

selenide is susceptible to oxygen especially since the reaction was carried under a flow of nitrogen.

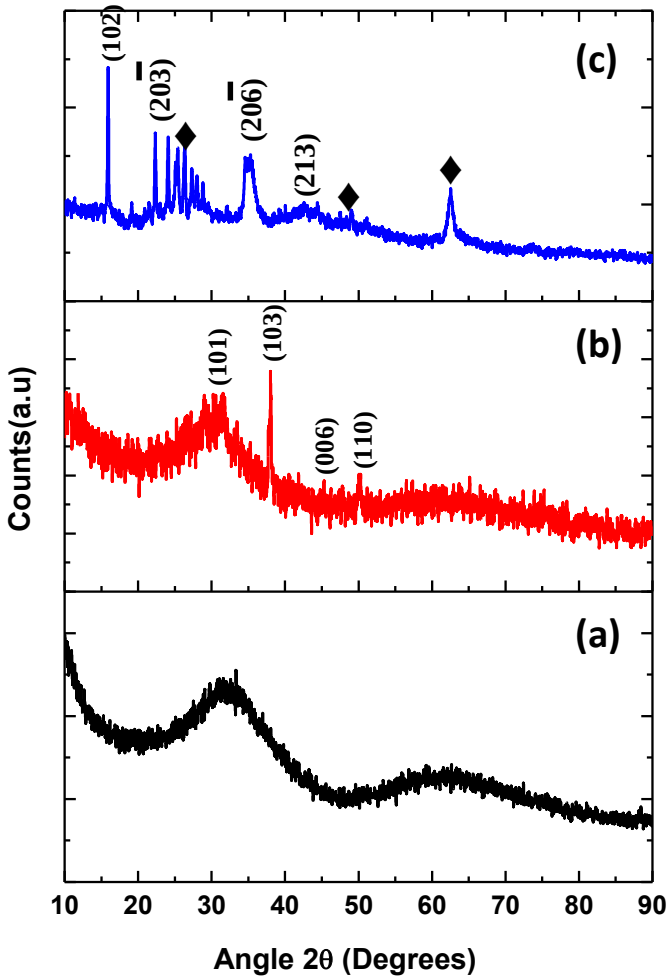

Fig. 5.12: XRD diffractograms of niobium selenide synthesized at different Nb:Se mole ratios, (a) 1:1, (b) 1:2 and (c) 1:3 where ♦ denotes Nb_2O_5.

The SEM images of the as-synthesized particles are shown in Fig. 5.13. The 1:1 mole ratio showed large spherical polydispersed particles. The 1:2 mole ratio showed two populations of particles, one spherical resembling the 1:1 mole ratio particles and the other showing plate-like particles consistent with 2D layered $NbSe_2$ materials.

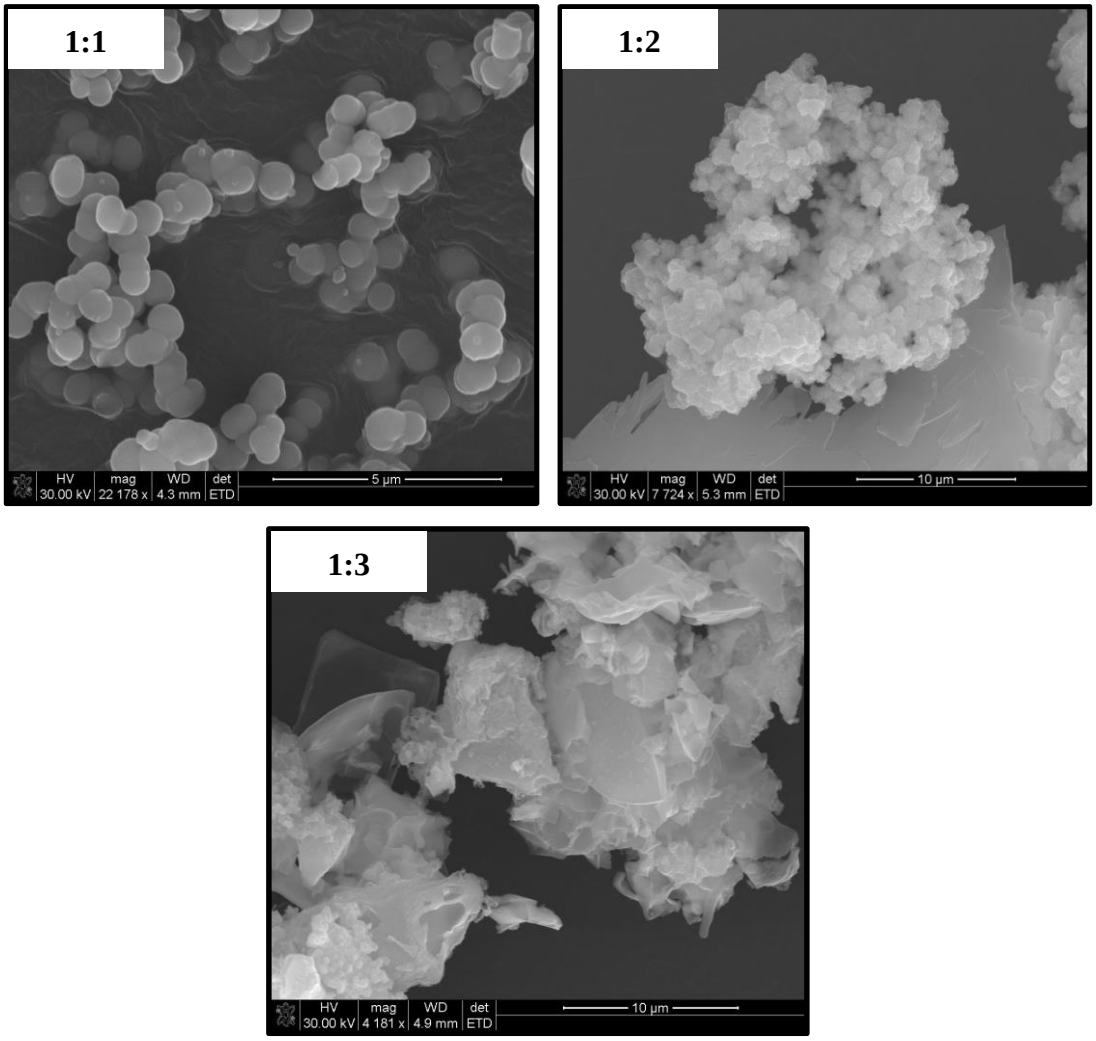

Fig. 5.13: SEM micrograms of niobium selenide synthesized at different Nb:Se mole ratios, 1:1, 1:2 and 1:3.

Shown in Fig. 5.14 are TEM images of the synthesized particles. The 1:1 mole ratio shows spherical particles that are polydispersed as already shown above. As the selenium ratio is increased to 2, there is a change in the morphology of the particles. The particles appear to be deformed suggesting a change in nature of the particles. This is consistent with the observed optical and XRD results hence suggesting that the particles are $NbSe_2$. As the selenium concentration is increased to a mole ratio of 1:3, the morphology of the particles changes to sheet-like structures comparable to what is observed in the SEM. This is not surprising as

$NbSe_2$ and $NbSe_3$ are layered materials that can form sheets. The sheet-like morphology seen in both 1:2 and 1:3 mole ratio samples is consistent with what other authors have observed. Tang et al. reported on the synthesis of $NbSe_3$ nanofibers and $NbSe_2$ microsheets, whilst Sun and co-workers reported on $NbSe_2$ nanoplates [17].

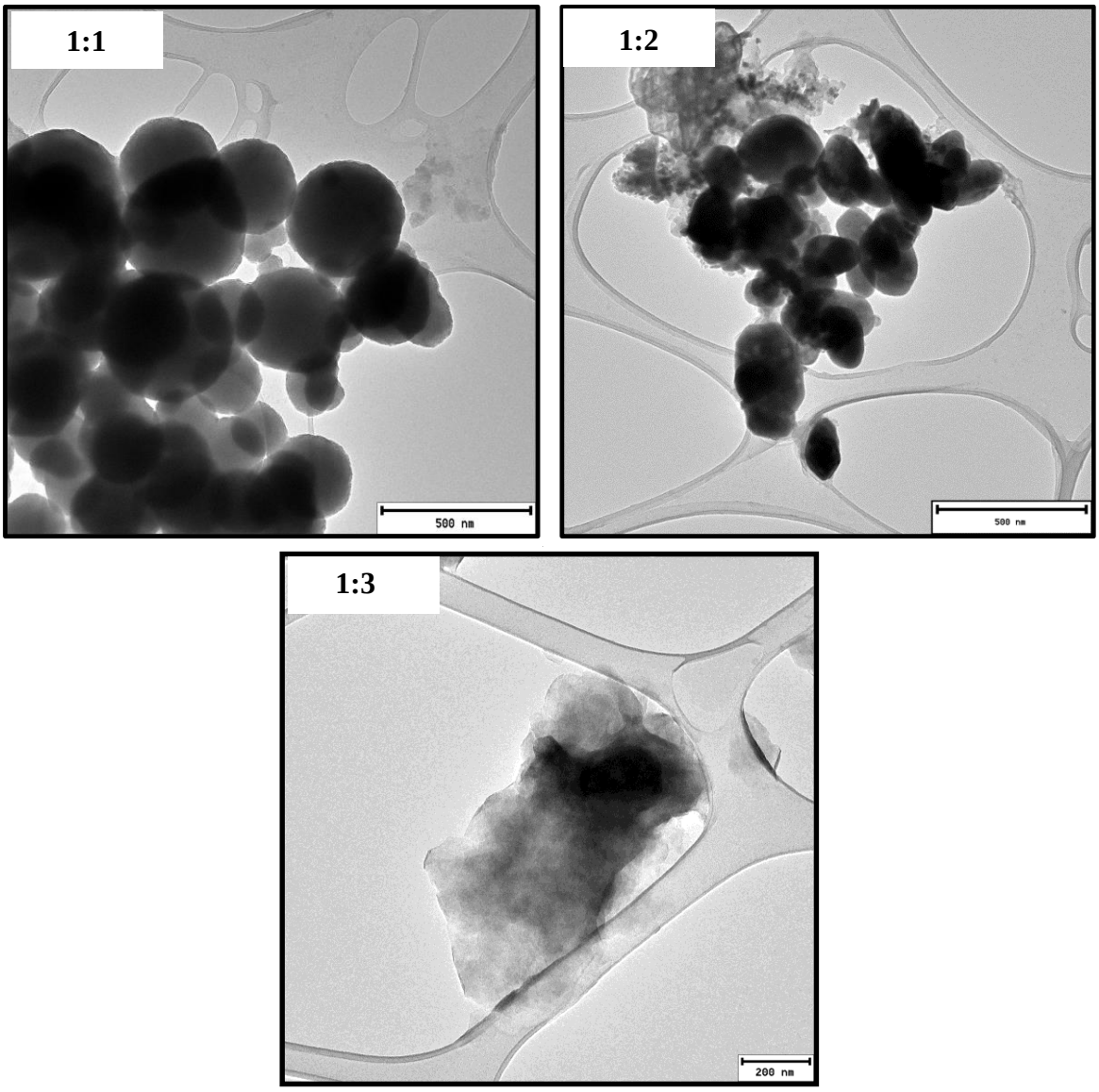

Fig. 5.14: TEM micrograms of niobium selenide synthesized at different Nb:Se mole ratios, 1:1, 1:2 and 1:3.

5.4 Conclusion

Niobium selenide was synthesized via the colloidal method using TOP/HDA combination for the first time. The effect of time on the particles synthesized using a 1:1 mole ratio of Nb:Se was negligible with particles showing similar properties. More concerning, the XRD of the samples were amorphous thus making it difficult to conclusively say that niobium selenide was synthesized successfully. The amorphous samples were then subjected to annealing to improve the crystallinity. Although some improvements were observed, annealing had very little effect on the properties of the particles suggesting a possibility that niobium selenide had not form or had many impurities. The later possibly being the most correct as the EDX spectroscopy did show a presence of Nb and Se albeit O was also present. The concentration of the selenium was then increased in order to form the more common $NbSe_2$ and $NbSe_3$. The XRD showed the formation of $NbSe_2$ and $NbSe_3$ for 1:2 and 1:3 Nb:Se ratios respectively. In addition, the particles resembled 2D nanostructures readily observed in layered materials such as $NbSe_2$ and $NbSe_3$. However, some impurities in the form of oxides were still observed.

References

[1] N. Moloto, H. Puggens, S. Govindraju, B. Rakgalakane, M. Kalenga, Thin Solid Films, 531, **2013**, 466.

[2] C. B. Murray, D. J. Norris, M. G. Bawendi, Journal of American Chemical Society, 115, **1993**, 8706.

[3] S. B. Artemikina, T. Y. Podlipskay, A. I. Bulavchenko, A. I. Komonov, Y. V. Mironov, V. E. Fedorov, Physiochemistry Engineering Aspects, 461, **2014**, 30.

[4] M. H. Van Maaren. G. M. Schaeffer, Physical Letters, 20, **1966,** 131.

[5] T. Tsuneta, T. Toshima , K. Inagaki , T. Shibayama , S. Tanda , S. Uji ,M. Ahlskog , P. Hakonen , M. Paalanen, Current Applied Physics, 3, **2003**, 473.

[6] M. Nath, S. Kar, A. K. Raychaudhuri, C. N. R. Rao, Chemical Physical Letters, 368, **2003**, 690.

[7] D. H. Galva´n, J. H. Kim, M. B. Maple, M. Avalos-Borja, E. Adem, Fullerene Science and Technology., 8, **2000**, 143.

[8] C. M Zelenski, P. K. Dorhout, Journal of American Chemical Society, 120, **1998**, 734.

[9] H. Liao, Y. Wang, S. Zhang, Y. Qian, Chemical Materials, 13, **2001**, 6.

[10] P. Sekar, E. C. Greyson, J. E. Barton, T. W. Odom, Journal of American Chemical Society, 127, **2005**, 2054.

[11] T. Tsunata, T. Toshima, K. Inangaki, T. Shitayama et al., Current Applied Physics, 3, **2003**, 473.

[12] A. Mamakhel, C. Tyrsted, E.D. Bøjesen, P. Hald, B.B. Iversen, Crystal Growth & Design, 1, **2013**, 4730.

[13] Y. Li, H. Liao, Y. Ding, Y. Fan, Y. Zhang, Y. Qian, Inorganic Chemistry, 38, **1999**, 1382.

[14] J. Xu, J.-P. Ge, Y.-D. Li, The Journal of Physical Chemistry B, 110, **2006**, 2497.

[15] H.G. Yang, G. Liu, S.Z. Qiao, C.H. Sun, Y.G. Jin, S.C. Smith, J. Zou, H.M. Cheng, G.Q. Lu, Journal of American Chemical Society, 131, **2009**, 4078.

[16] X. Wang, J. Zhuang, Q. Peng, Y. Li, Nature, 437, **2005**, 121.

[17] H. Tang, C. Li, X. Yang, C. Mo, K. Cao, F. Yang, Crystal Research and Technology, 46, **2011**, 400.

[18] A.A. Stabile, L. Whittaker, T.L. Wu, P.M. Maley et al., Nanotechnology, 22, **2011**, 4852.

[19] N. Moloto, M.J. Moloto, N.J. Coville, S.S. Ray, Journal of Crystal Growth, 324, **2011**, 41.

[20] G. Wang, E. Palleau, T. Amand, S. Tongay, X. Marie, B. Urbaszels, Applied Physical Letters, 106, **2015**, 11210.

[21] M.W. Dlamini, D.O. Kumi, J.N. Phaahlamohlaka, D.S. Lyadov, D.G. Billing, L.L. Jewel, N.J. Coville, Chemical Catalysis Chemistry,18, **2015**, 3000.

[22] E. Revolinsky, G. A. Spiering,D. J. Beerntsen, Journal of Physics and Chemistry of Solids, 26, **1965**, 1029.

[23] M. Fukuto, J. Anderson, M.D. Hornbostel, D.C. Johnson, H. Huang, S.D. Kevan, Journal of alloys and compounds, 248, **1997**, 59.

CHAPTER 6

SYNTHESIS AND CHARACTERIZATION OF NIOBIUM SELENIDE/POLYVINYLCARBAZOLE NANOCOMPOSITES AND THEIR USE AS ACTIVE LAYERS IN HYBRID SOLAR CELLS

6.1 Introduction

Intense pressure has been asserted onto energy research groups to find renewable and green energy sources due to the current climatic state. Since the first silicon based solar cell fabrication, there is a drive to reduce the cost of production and to increase the efficiencies of these cells [1]. Technological advancement has led to a variety of types and generations of solar cells being developed [2-5]. One of these technologies is organic solar cells, which have immense potential to being a low cost effective way of providing energy. The key element to low cost production of organic solar cells is the ability to be manufacture via a solution based roll to roll process [6]. Since the material is light weight and flexible organic based solar cells can be used in a variety of applications [7-8]. Power conversion efficiency (PCE) of just over 10% has been recently reported for bulk heterojunction (BHJ) solar cells, with the general design of using a fullerene as the acceptor and conductive polymer as the donor [9]. Some of the difficulties that these devices face are the low open circuit voltage (V_{OC}), which has contributed to the decrease in growth rates of the PCE of these solar cells [10]. Difference's in mobility of electrons and holes in heterogeneous BHJ solar cells and volume ratios of different material has been reported to impact the V_{OC} [11]. Loss of free chargers due to biomolecular recombination at the interfaces of heterogeneous material due to the difference in work function is another contributing factor for low V_{OC} [12].

In order to bypass some of these challenges facing the V_{OC} researchers try replacing the fullerene with inorganic nanocrystals [13]. Hybrid solar cells have the ability to surpass the PCE of current BHJ solar cells theoretically as the intrinsic properties of nanocrystals such as tunable band gap, high absorption co-efficiencies and high carrier motilities [14]. These properties can be manipulated to suit the needs of the architecture of the devices, as nanocrystals are able to absorb a broader spectrum of solar radiation, branched crystals can be synthesized in order to facilitate improved charge transport [15-16]. Numerous studies have shown the improvement that CdSe has had when adding it to a polymer to form a hybrid CdSe/polymer based solar cell. By varying morphology of the nanocrystals and changing the polymer base PCE have varied in these studies [17-22]. The most effective polymer based has been poly(3-hexylthiophene-2,5-diyl) P3HT but due to its high cost alternative polymers needed to be used hence poly vinyl carbazole seems suitable.

Niobium selenide is a material known for displaying superconductivity. Superconductivity is a phenomenon of zero electrical resistance and expulsion of magnetic flux fields occurring in certain materials when cooled below a characteristic critical temperature. At room temperature it has been shown to behave as a semiconductor. Niobium selenide has been reported to form multilayered structures similar to MoS_2 [23-25]. Sekar et al. reported on the use of a one pot synthesis method which yielded 1D and 2D nanostructures [26]. Layered structures like perovskites have been used in solar cells with some promising efficiencies [27-28]. Since the properties of niobium selenide have exhibited semiconducting characteristics, it is possible to use this material as the active layer in hybrid solar cells. Herein we report on the synthesis and characterization of niobium selenide/polyvinylcarbazole (PVK) nanocomposite where PVK is a conductive polymer that assists in charger transport, it behaves as a hole transporting material. Test on the thermal and structural properties have been conducted to monitor the effect the

nanomaterial has on the polymer. We further report on the use of the polymer nanocomposites as active layers in solar cells.

6.2 Experimental Section

6.2.1 Materials

Niobium (V) chloride, selenium powder, trioctylphosphine (TOP), hexadecylamine (HDA), polyvinyl-9-carbazole (PVK) (MW 1,100,000 $gmol^{-1}$), pyridine, methanol, acetone, isopropanol and poly(3,4-ethylenedioxythiophene)-poly(styrenesulfonate) were all purchased from Sigma-Aldrich.

6.2.2 Synthesis of niobium selenide/PVK nanocomposites

Niobium selenide nanocrystals were synthesized using a method described in Chapter 5. Niobium selenide nanocrystals synthesized in 45 min (1:1), (1:2) and (1:3) mole ratios were used as fillers in polymer nanocomposites. The nanocrystals were first dispersed in pyridine in order to exchange the long-chained HDA with a shorter pyridine ligand. The nanocrystals were then flocculated from the pyridine solution by the addition of methanol and subsequently washed several times with methanol and dried at room temperature. The dried powders were then dispersed in chloroform. PVK was subsequently also dissolved in the common solvent chloroform. The two chloroform solutions were mixed and allowed to stir for 30 min at 70 °C. The resultant composite was flocculated by the addition of methanol and collected through centrifugation. The amount of the nanocrystals was kept at 10 wt. % due to the results obtained for copper selenide in order to give the desired composition of the nanocomposites.

6.2.3 Fabrication of the hybrid solar cells

The structure of the devices consisted of the following layers of films: ITO / PEDOT-PSS / amorphous / crystalline $NbSe_y$-PVK nanocomposite / aluminium. The substrates were routinely cleaned by sequential ultrasonication in acetone, isopropanol, and de-ionized water and then dried in air for 20 min. Aqueous PEDOT-PSS dispersions were spin-coated on the substrates and then annealed at 150 °C for 30 min forming thin films with a thickness of about 55 nm. The nanocomposite layers (25 mg/mL) were spin coated at 3000 rpm, dried and annealed at 150 °C for 30 min resulting in a thin film coating of ~200 nm. The top Al contacts were sputtered through a shadow mask to generate an array of patterned electrodes. The Al was deposited by thermal evaporation in high vacuum of better than 5×10^{-5} Pa at a rate of about 0.2 nm/s. The final area of each device was 0.08 cm^2 and was defined by the overlap between the top ITO and bottom Al electrodes.

6.2.4 Instrumentation

The morphology of the nanoparticles was determined on Technai G2 TEM Spirit operated at 200 kV. SEM analysis was performed on FEI Nova Nanolab 600 FIB/SEM instrument operating at 30 kV. The samples on a carbon tape were coated by a gold-palladium layer before the analysis. A Brüker Tensor 27 Fourier Transform Infrared spectrometer was used to analyze the surface functionalities and the type of functional groups present on the materials. Thermogravimetric analysis (TGA) was performed with a Perkin-Elmer STA6000 using nitrogen as the purge gas and a heating rate of the 10 °$Cmin^{-1}$. The flow rate of the purge gas was kept at 20 $mLmin^{-1}$. A Varian Cary Eclipse (Cary 50) UV-VIS spectrophotometer was used to carry out the absorption measurements. A Varian Cary Eclipse EL04103870 fluorescence spectrophotometer with a medium PMT voltage at an excitation wavelength of 300 nm was used to measure the photoluminescence (PL) of the samples. For both spectral

analyses, the powders were dissolved in chloroform and placed in quartz cuvettes (1cm path length). The thin film thicknesses were determined by a Filmetrics F20 instrument. The device performances were characterized under AM1.5G 100 mW/cm^2 illumination in a laminar flow cabinet.

6.3 Results and discussion

Electron microscopy was used to determine the morphology and the extent of interaction between niobium selenide nanocrystals and the polymer PVK. Fig. 6.1 (a) - (c) shows the SEM micrographs of the synthesized niobium selenide nanocrystals. The nanocrystals range from spherical to a mixture of sphere-like and sheets to complete sheets. More importantly these nanocrystals have been characterized as amorphous $NbSe_y$ to $NbSe_2$ and $NbSe_3$ as shown in Chapter 5. All of the nanocrystals were first dispersed and refluxed in pyridine to strip off the long alkyl chained amine HDA. Pyridine has shown that it is able to form weak and reversible bonds with the surface of the nanocrystals [29]. This process of ligand exchange was carried out to facilitate and allow the polymer and the nanocrystals to interact unhindered and form stable bonds between the two materials. Based on the results obtained for copper selenide (Chapter 4), 10 wt. % was chosen as the optimum loading of the nanocrystals. Fig 6.1 (d) represents the SEM images of the pristine polymer, Fig. 6.1 (e) - (g) represent the amorphous $NbSe_y$, $NbSe_2$ and $NbSe_3$ nanocomposites respectively. The polymer surface showed a smooth morphology consistent with other polymers. The amorphous niobium selenide nanocrystals are encapsulated with the polymer hence showing really good interaction. The crystalline $NbSe_2$ nanocomposite shows blend of nanocrystals with the polymer. Although no distinct feature of the nanocrystals are seen, the texture of the polymer has chanced suggesting that crystalline spherical-like nanocrystals are incorporated. The $NbSe_3$ nanocomposite shows smooth flaky morphology consistent with the nanosheets and polymer blend. The sample seem to be

homogeneous thus suggesting an excellent interfacial interaction between the polymer and the nanosheets.

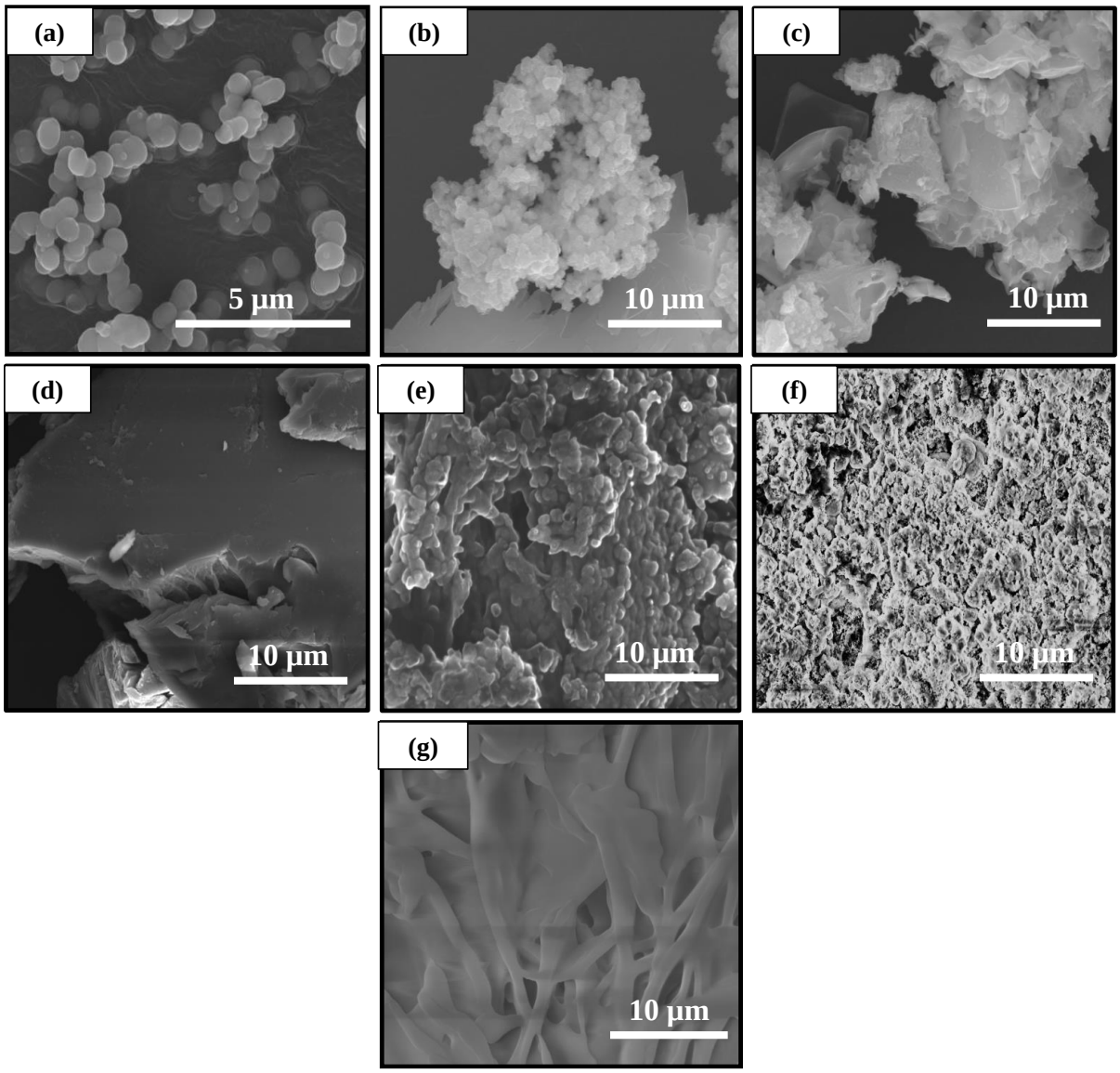

Fig. 6.1: SEM micrographs of (a) amorphous $NbSe_y$ nanospheres, (b) $NbSe_2$, (c) $NbSe_3$ (d) amorphous $NbSe_y$/PVK nanocomposite, (e) $NbSe_2$/PVK nanocomposite and (f) $NbSe_3$/PVK nanocomposite.

Energy dispersive X-ray spectroscopy (EDX) was done to ascertain the presence of niobium selenide nanocrystals within the polymer. The pristine PVK in Fig. 6.2 (a) shows only carbon and nitrogen as expected. Fig. 6.2 (b) - (d) shows the presence of niobium, selenium, carbon

and oxygen. The oxygen is usually an opportunistic contaminant often harvested from the atmosphere. No nitrogen peaks were detected for all the composites; it was probably harder to perturb the nitrogen as it covalently binds to the surface of the nanocrystals.

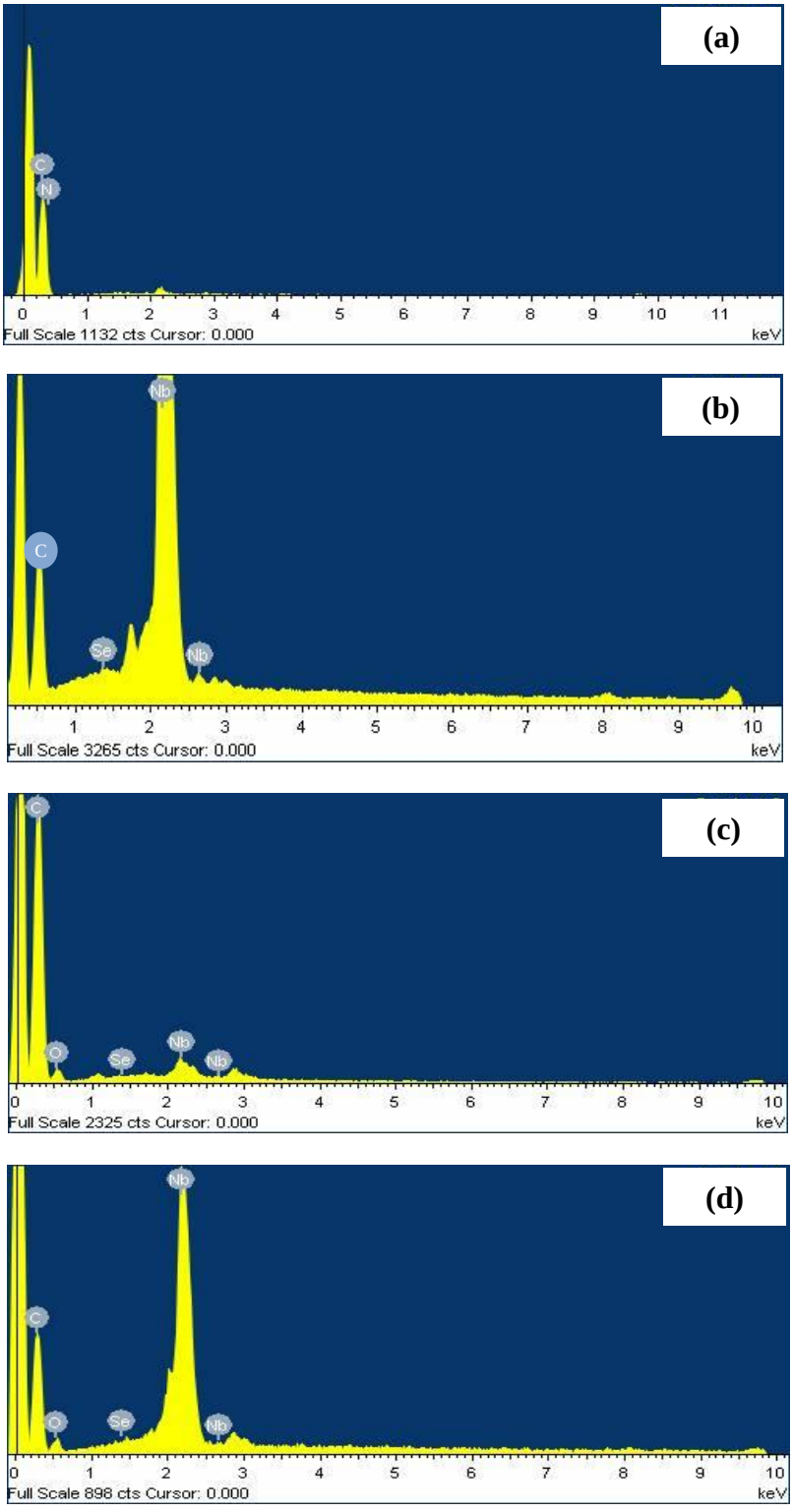

Fig. 6.2: EDX spectra of (a) PVK, (b) amorphous $NbSe_y$/PVK nanocomposite, (c) $NbSe_2$/PVK nanocomposite and (d) $NbSe_3$/PVK nanocomposite.

FTIR spectroscopy is to aid in determining structural changes to the polymer that is caused by the addition of the nanocrystals. This technique can assist in determining the structural interactions between the materials and too what extent. Fig. 6.3 (a) shows the pristine polymer, Fig. 6.3 (b) - (d) shows the respective nanocomposites. The spectra are almost identical except for a slight shift in the finger print stretching frequency in the 1200 cm^{-1} region. In addition, there is a slight decrease on the intensity of the C-H peak located at 1454 cm^{-1} from the pristine PVK to the polymer nanocomposites. From the obtained results, it is clear that the integrity of the polymer is maintained. This is desirable as the aim of forming a polymer nanocomposite is to enhance some of the properties of the native polymer such as electrical conductivity however maintained the structural properties such as flexibility.

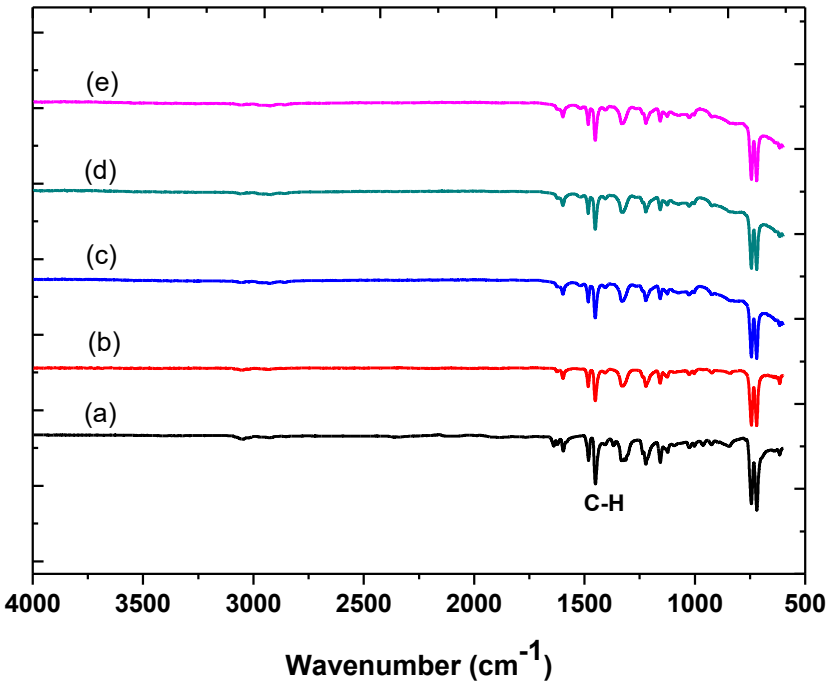

Fig. 6.3: FTIR spectra of (a) PVK, (b) amorphous $NbSe_y$/PVK nanocomposite, (c) $NbSe_2$/PVK nanocomposite and (d) $NbSe_3$/PVK nanocomposite.

To further investigate the structural properties of the nanocomposites, TGA was performed. Fig. 6.4 shows the thermal stabilities of the pristine polymer and the different nanocomposites.

Fig. 6.4 (a) shows the TGA curve of the pristine polymer (PVK) where the first degradation is due to the loss of water and other volatiles that may be present. At 450 °C the polymer degrades to completion which is expected. Fig. 6.4 (b) - (d) represents the different polymer nanocomposites. The nanocomposites show similar curves to the polymer alone however, the nanocrystals clearly degrade at higher temperatures as there is significant material remaining above 600 °C. This is expected as niobium selenide degrades at very high temperatures.

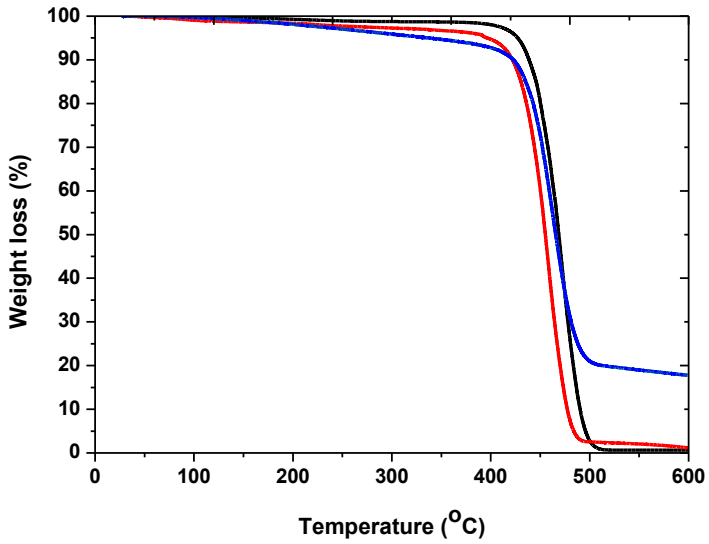

Fig. 6.4: TGA of (a) PVK, (b) amorphous $NbSe_y$/PVK nanocomposite, (c) $NbSe_2$/PVK nanocomposite and (d) $NbSe_3$/PVK nanocomposite.

The optical spectra of the polymer and nanocomposites are shown in Fig. 6.5. The absorption spectrum of the polymer shows a band edge at 374 nm characteristic to PVK. PVK has a very broad emission spectrum covering the entire visible region. The peak at 390 nm originates from low energy inter-chain excimer recombination [30]. The other peaks may be caused by the formation of dimers [31]. The nanocomposite of amorphous $NbSe_y$/PVK nanocomposite shows an absorption spectrum with band edge located at 369 nm. This is slightly blue-shifted from the PVK band edge. This is mostly likely due to the combination of the nanocrystals which

have a band edge of 320 nm as shown in Chapter 5 together with the polymer. The PL shows multiple peaks attributed to the polydispersity of the nanocrystals and the PVK. The $NbSe_2$/PVK nanocomposite has an absorption band edge at 366 nm and a PL spectrum with multiple peaks. This is similar to the amorphous $NbSe_y$/PVK nanocomposite and is to be expected as the properties of the nanocrystals were similar as reported in Chapter 5. The absorption spectrum of $NbSe_3$/PVK nanocomposite is quite weird with a number of small peaks. This is consistent with the UV-Vis spectrum observed for the nanoparticles. The consistency is also observed in the PL spectrum where one broad emission peak is seen that is similar to that of the nanocrystals. Clearly from the optical data, the features of the nanocrystals become stronger as the nanocrystals evolve from spheres to sheets; this is attributed to the expected large surface area of the nanosheets.

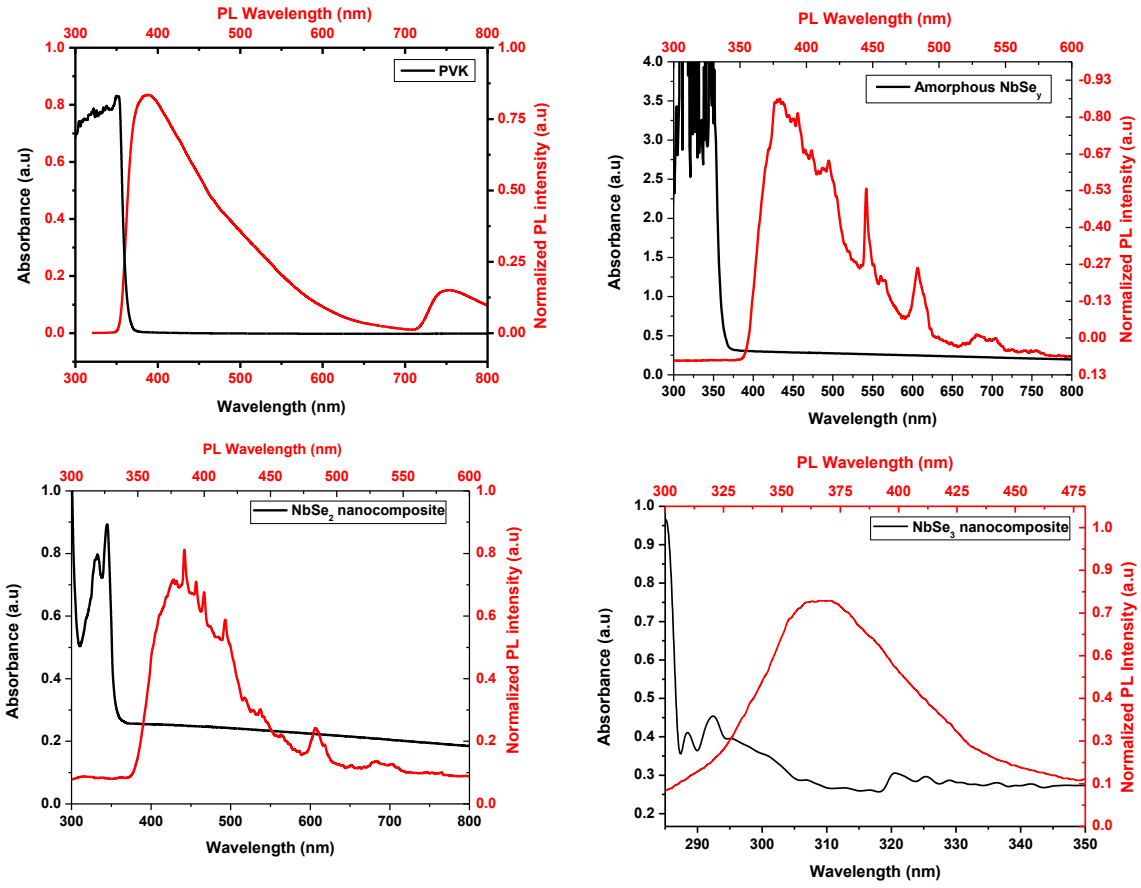

Fig. 6.5: UV-Vis absorption and PL spectra of (a) PVK, (b) amorphous $NbSe_y$/PVK nanocomposite, (c) $NbSe_2$/PVK nanocomposite and (d) $NbSe_3$/PVK nanocomposite (excitation wavelength = 300 nm).

The synthesized nanocomposites were then tested in a simple device configuration depicted in Fig. 6.6. Niobium selenide nanocrystals act as electron acceptors and PVK as a hole acceptor and for a perfect device the bands should offset each other as shown in Fig. 6.6. The HOMO and the LUMO of PVK are well known however for the nanocrystals other techniques were necessary to determine the energy of the two bands. Instead, the bandgap is used extracted from the UV-Vis absorption spectra. The final device assembly is therefore ITO/PEDOT:PSS/$NbSe_y$-PVK/Al. ITO is the transparent conducting oxide and acts as an electrode, PEDOT-PSS is a transparent conductive polymer and act as an electron blocking

layer therefore assisting in the separation of the exciton and transportation of the hole. Aluminium acts as a counter electrode thus completing the circuit.

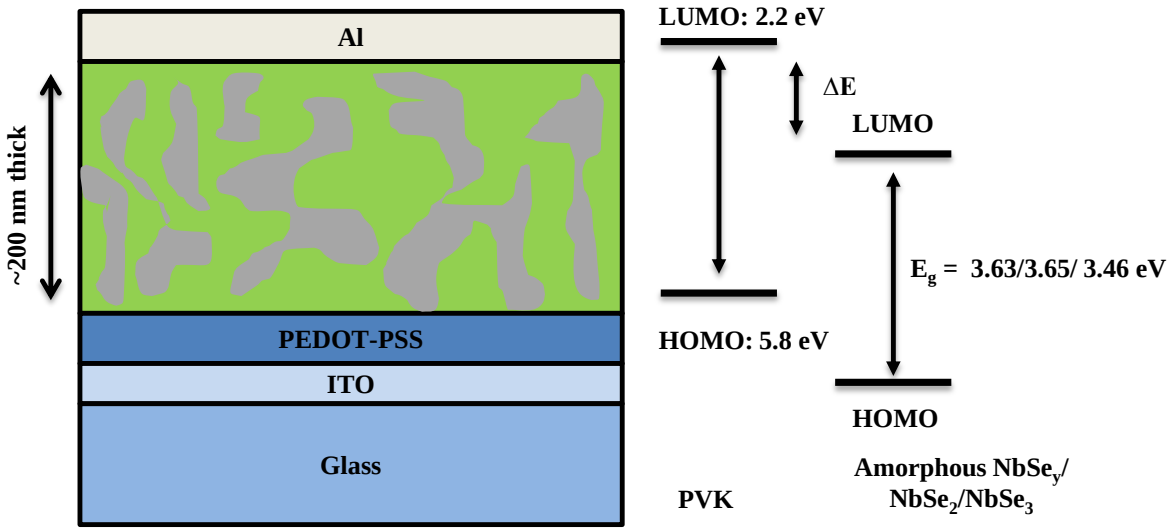

Fig. 6.6: Device architecture and band structure of the hybrid solar cell.

A forward bias voltage was applied to generate the J-V curves. The measurements were first done in the dark in order to determine the diode characteristics of the devices. Fig. 6.7 shows the J-V curves of the nanocomposites under illumination.

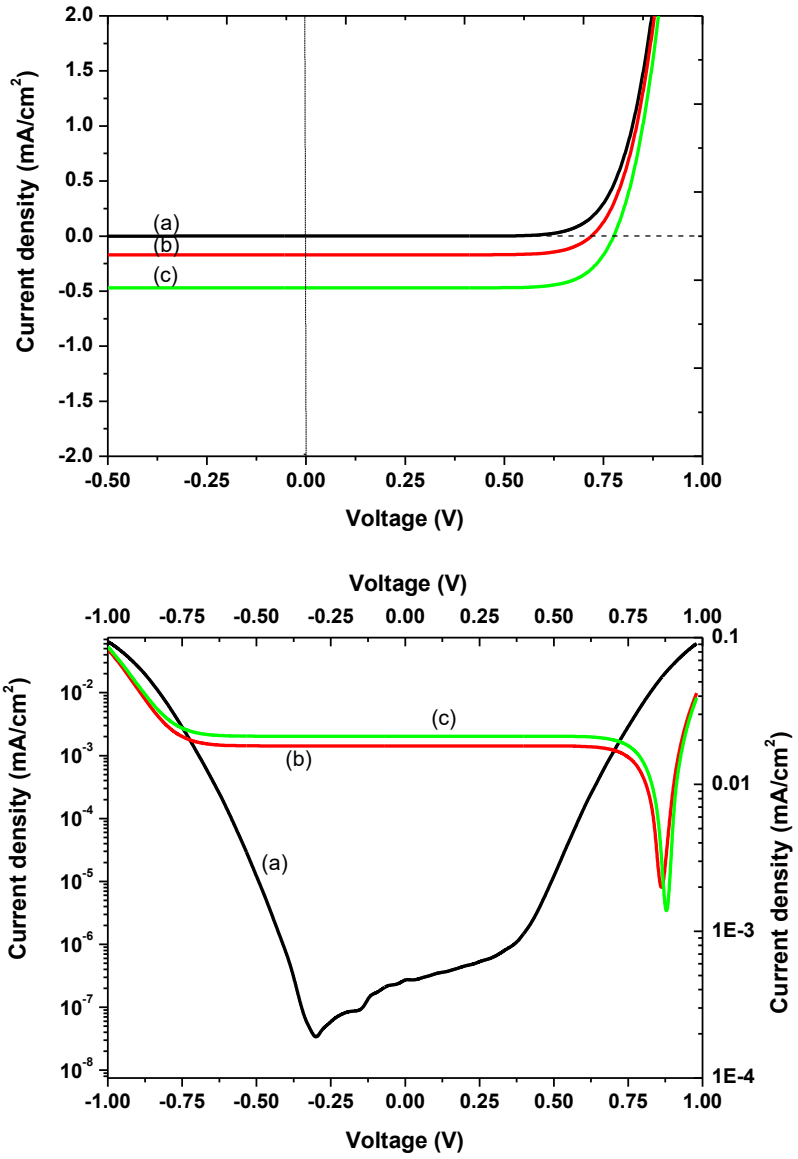

Fig. 6.7: J-V curves of (a) amorphous $NbSe_y$/PVK nanocomposite, (b) $NbSe_2$/PVK nanocomposite, (c) $NbSe_3$/PVK nanocomposite and the corresponding semi-log plot.

The amorphous $NbSe_y$/PVK nanocomposite showed good rectification of the curve implying it behaves like a diode however under illumination, no current was generated. This could most likely be due to nature of the nanocrystals especially since it was hard to definitively identify them using XRD. The solar cell parameters for the other composites are described in Table 6.1. The open circuit voltage (V_{OC}) and the short circuit current (J_{SC}) for the NbSe2/PVK

nanocomposite were 0.86 V and 0.193 mA/cm^2 with the fill factor (FF) of 52%. The power conversion efficiency (PCE) for the device was 1.079%. On the other hand the NbSe3/PVK device produced a V_{OC} of 0.88 V and a J_{SC} of 0.49 mA/cm^2 with a FF of 60% which resulted in a PCE of 3.234%. It must be pointed out that these devices were not optimized and the experiments were merely to prove that niobium selenide can be employed in hybrid solar cells similar to CdSe and PbSe. From the obtained data, it is quite clear that 2D nanostructures such as nanosheets of $NbSe_3$ produced a device that performs much better due to the large surface area which most likely improves the interaction between the nanosheets and the polymer thus improving the charge transfer between the donor polymer and the acceptor nanosheets.

Table 6.1: Device properties of the nanocomposites

Sample	**V_{OC} (V)**	**J_{SC} (mA/cm^2)**	**FF (%)**	**Ƞ (%)**
Amorphous $NbSe_y$/PVK	0.30	0	-	-
$NbSe_2$/PVK	0.86	0.193	52	1.079
$NbSe_3$/PVK	0.88	0.49	60	3.234

6.4 Conclusion

In conclusion, herein we have shown for the first time that niobium selenide nanocrystals can be used in hybrid solar cells as substitute for the commonly used nanocrystals. In order to have an effective hybrid layer great consideration needs to be taken into on the effect the nanocrystals have on the polymer. As shown in this instance the morphology and phase of the nanocrystals does influence the polymers ability to transfer charges through the solar device. As such, the device with the spherical, not quite identified niobium selenide performed the worst with no current generated whilst the polydispersed $NbSe_2$ based nanocomposite had fairly good results with the PCE of 1.079%. The $NbSe_3$ based nanocomposite device performed

the best with the PCE of 3.234% which is even far better than the copper selenide based device reported in Chapter 4.

References

[1] D.M. Chapin, C.S. Fuller, G.L. Pearson, Journal of Applied Physics, 25, **1954**, 676.

[2] D. J. Norris, M.G. Bawendi, Physic Review B, **1996**, 53, 16338.

[3] C.J. Murphy, Peer Reviewed: Optical Sensing With Quantum Dots, 520A, **2002**.

[4] C. Wang, M. Shim, P. Guyoty-Sionnest, Applied Physical Letter, 80, **2002**, 4.

[5] E. Kucur, J. Riegler, G. A. Urban, T. Nann, Journal of Chemical Physics, 119, **2003**, 2333.

[6] W.U. Huynh, J.J. Dittmer, A.P. Alivisatos, Science, 295, **2002**, 2425.

[7] W.U. Huynh, J.J. Dittmer, W.C. Libby, G.L. Whitting, A.P. Alivisatos, Advance Functional Materials, 13, **2003**, 73.

[8] N.C. Greenham, X. Peng, A.P. Alivisatos, Physical Review B: Condense Matter, 54(24), **1996**, 17628.

[9] Y.Y Linag, Z. Xu, J.B. Xia, S.T. Tsai, Y. Wu, G. Li, C. Ray, L.P. Yu, Advance Materials., 22, **2010,** 135.

[10] M.C. Scharber, D. Muhlubacher, M. Koppe, P. Denk, C. Waldauf, A.J. Heeger, C.J. Barbec, Advance Materials,18, **2006**, 789.

[11] V.D. Mihailetchi, L.J.A. Koster, P.W.M. Blom, C. Melzer, B. de Boer, J.K.J van Duren, R.A.J. Janssen, Advance Functional Materials, 15, **2005**, 5.

[12] V.D. Mihailetchi, L.J.A. Koster, J.C. Hummelen, P.W.M. Blom, Physical Review Letter, 93, **2004**, 216601.

[13] Y. Zhou; Solar Energy Materials and Solar Cells, 65, **2011**, 1535.

[14] Y. Zhou, M. Eck, M. Kruegar, Energy Environmental Science, 3, **2010**, 1865.

[15] N. Moloto, H. Puggens, S. Govindraju, B. Rakgalakane, M.P. Kalenga, Thin Solid Films, 531, **2013**, 1851.

[16] M.P Kalenga, S. Govindraju, M. Airo, M.J. Moloto, L.M. Sikhwivhilu, N. Moloto, Journal of Nanoscience and Nanotechnology. 14, **2014**, 1.

[17] J. Bisquert, D. Cahen, G. Hodes, S. Rühle, A. Zaban, Journal of Physical Chemistry. B, 108, **2004**, 8106.

[18] W. Ma, C. Yang, X. Gong, K. Lee, A.J. Heeger, Advance Functional. Materials, 15, **2005**, 1617.

[19] B.C Sihn, M. Wolf, Journal of Physical Chemistry. C, 111, **2007**.

[20] J.S Owen, J. Park, P.E. Trudeau, A.P. Alivisatos, Journal of American Chemical Society, 130, **2008**, 12279.

[21] J.S Liu, T. Tanaka, K. Sivula, A.P. Alivisatos, J.M.J. Frechet, Journal of American Chemical Society, 126, **2004**, 6550.

[22] Y. Wu, G. Zhang, Nano Letters, 10, **2010**, 1628.

[23] S. B. Artemikina, T. Y. Podlipskay, A. I. Bulavchenko, A. I. Komonov, Y. V. Mironov, V. E. Fedorov, Physiochemical and Engineering Aspects, 461, **2014**, 30.

[24] M. H. Van Maaren. G. M. Schaeffer, Physic Letters A, 20, **1966**, 131.

[25] T. Tsuneta , T. Toshima , K. Inagaki , T. Shibayama , S. Tanda , S. Uji ,M. Ahlskog , P. Hakonen , M. Paalanen, Current Applied Physics, **2003**, 473.

[26] P. Sekar, E. C. Greyson, J. E. Barton, T. W. Odom, Journal of American Chemical Society, 127, **2005**, 2054.

[27] M. Petrovic, V. Chellappan, S. Ramakrishna, Solar Energy, 122, **2015**, 678.

[28] B. Bhattacharya, P.K. Singh, R. Singh, Z.H. Zhan, International Journal of Hydrogen Energy 4, **2016**, 2847.

[29] Y. Zhou, M. Eck, M. Kruegar, Energy and Environmental Science, 3, **2010**, 1851.

[30] J.G. Winiarz, L. Zhang, M. Lal, C.S. Friend, P.N. Prasad, Chemical Physics, **1999**, 245, 417.

[31] X. Guo, N. Zhou, S.J. Lou, J. Smith, D.B. Tice, J.W. Hennek, R.P. Ortiz, J.T. Lopez Navarrete, S. Li, J. Strzalka, L.X. Chen, R.P.H. Chang, A. Facchetti, T.J. Marks, Nature Photonics, 7, **2013**, 825.

CHAPTER 7

CONCLUSION AND RECOMMENDATIONS

7.1 Conclusion

7.1.1 Synthesis and characteristic of copper selenide nanocrystals and copper selenide nanocomposites

Copper selenide nanocrystals were successfully synthesized using the conventional colloidal method. Various synthetic parameters were altered to investigate the effect on the structural, optical and electronic properties of these materials. Parameters such as temperature, reaction kinetics, capping agents and precursors were optimized to produce desired products. The optimum conditions were reported earlier in the thesis. Upon varying the time of the reaction, that method produced the first reported case of size dependent colour variation of Cu_2Se nanocrystals. The size of the crystals varied form 2 nm to 10 nm depending on the length of the reaction time. At reduced times the particles showed a bright blue colour with a size of 2 nm but with poor sample distribution resulting in a higher amount of agglomeration. Due to the synthesis being cut off at 2 min this prevented crystal growth. After 10 min the solution became black and all that was observed was an increase in particle size although particle dispersion improved due to improved capping of the nanocrystals. The 10 nm particles showed improved electronic, optical and structural properties. The reaction temperature for the optimized reaction was at 220 °C with a reaction time of 10 min.

Hybrid nanocomposites of different weight percentages using PVK and Cu_2Se were successfully synthesized. The results helped obtain an optimum weight percentage ratio for the Cu_2Se nanoparticles to polymer. The 10% ratio showed the most promising structural and

optical properties as all of the structural integrity of the polymer remained intact. The results show that the increase in nanoparticle addition caused the polymer to break intermolecular bonds and thus degrade the quality of the polymer itself. This trend can be seen in the electrical performance of the solar devices fabricated using this nanocomposite. The results showed that it is of utmost importance for the polymer backbone to remain structurally stable as this helps with the movement of charges through the matrix and the prevention of electron trapping. The 50% nanocomposite synthesized showed significant change in structural properties, to a point where the original polymer structure is completely damaged resulting in poor optical and electronic properties.

7.1.2 Synthesis and characterization of niobium selenide and niobium selenide nanocomposites

Niobium selenide was synthesized using the colloidal method. This method proved to be difficult. Amorphous niobium selenide spherical nanoparticles were obtained at different synthetic times. The amorphous nature of the nanocrystals made it difficult to identify the phase of the nanoparticles. In order to try and improve the crystallinity of the nanoparticles, the particles were annealed under a stream of nitrogen at 700 °C for 60 min. A slight improvement was observed. This probably suggested that the particles had a lot of impurities since EDX did dhow a presence of both niobium and selenium. The effect the selenium concentration was the tested. This proved a little more effective as $NbSe_2$ and $NbSe_3$ were formed after a stoichiometric amount of selenium was added. The resultant particles could be identified using XRD, albeit some impurities were present, niobium pentoxide. Sheet-like morphology emerged for both $NbSe_2$ and $NbSe_3$ which is consistent with reported data. $NbSe_2$ had a mixed morphology with the amorphous spheres still being observed. The nanocomposites of these three observed particles, i.e. amorphous niobium selenide, $NbSe_2$ and $NbSe_3$ were synthesized

with the $NbSe_2$ and $NbSe_3$ showing similar behaviour in many ways however the amorphous spheres also found in the $NbSe_2$ sample did alter the properties. The integrity of the polymer was maintained since only 10 wt. % was used. The SEM showed good interaction between the nanoparticles and the polymer for all the samples.

7.1.3 Fabrication of solar devices using nanocomposites

Cu_2Se nanocomposites demonstrated the photovoltaic effect using a hybrid device. The 10% nanocomposite performed the best due to the high structural integrity of the nanocomposite which allowed for a more efficient charge transport system. Integral parameters were obtained and it showed that a reduction in Cu_2Se nanocrystal addition was beneficial for the device performance although low efficiencies where obtained from all samples. Fabrication of these devices was important in testing the application of the nanocomposites in solar cells and the aim was not to achieve incredible solar efficiencies since the devices were not optimized. That is parameters such as film thickness and roughness were not optimized, other additives were not add which may have improve the device and different electrodes were not tested just to mention a few. Niobium selenide nanocomposites based devices performed much better than the copper selenide based devices. This probably must do with their layered structures resulting in larger surface area compared to spherical nanoparticles. Not much is known about niobium selenide hence making the obtained results quite appealing. The $NbSe_2$ based device achieved a PCE of about 1% whilst the $NbSe_3$ device achieved about 3%.

7.2 Recommendations

There is quite a lot of work that needs to be done on the synthesis of niobium selenide at different stoichiometry especially since they seem to have interesting properties. This can probably be extended to tantalum selenides as they behave in a similar fashion. For future work

a better conductive polymer can be used such as P3HT to test the performance of a nanocomposite. Various device parameters can be altered to improve device performance such as varying electronic contacts. Varying device fabrication techniques to investigate which technique is most suitable for nanocomposite i.e. drop casting vs spin coating vs deep coating etc. A study into electro-spinning of the nanocomposites can be carried out to test the effect of having a different morphology of the nanocomposite on the efficiency of the device. Post treatment of the thin films can also be attempted as it has been shown that this can have quite an effect on the performance of solar cells. Finally, the device architecture can of course be altered.

APPENDIX

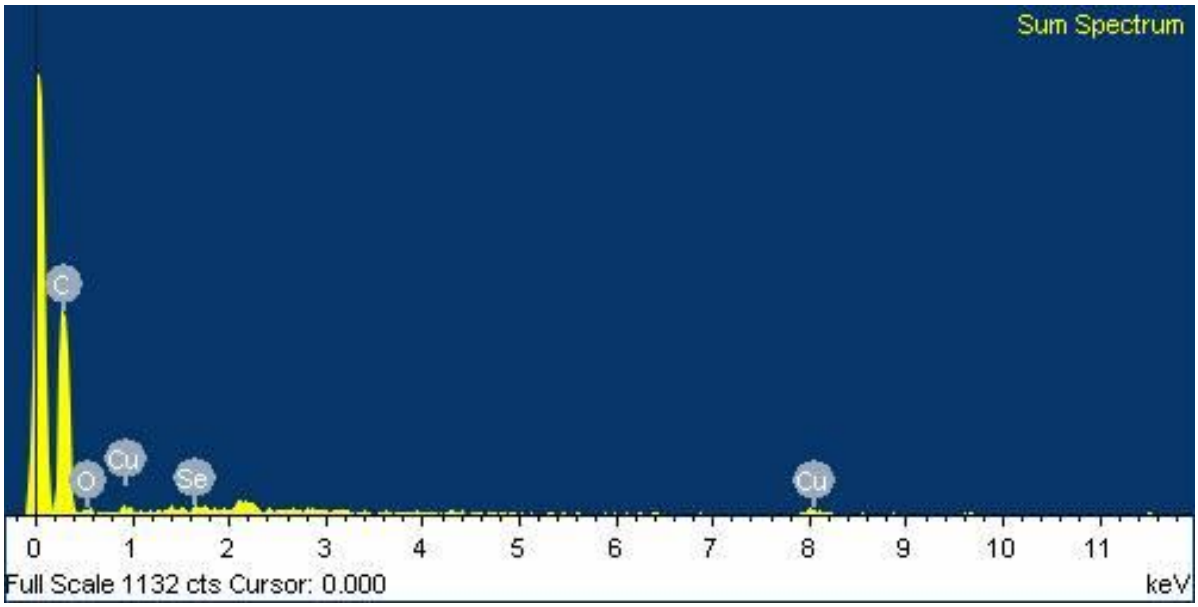

Fig. 3.1S: EDX spectrum of Cu_2Se

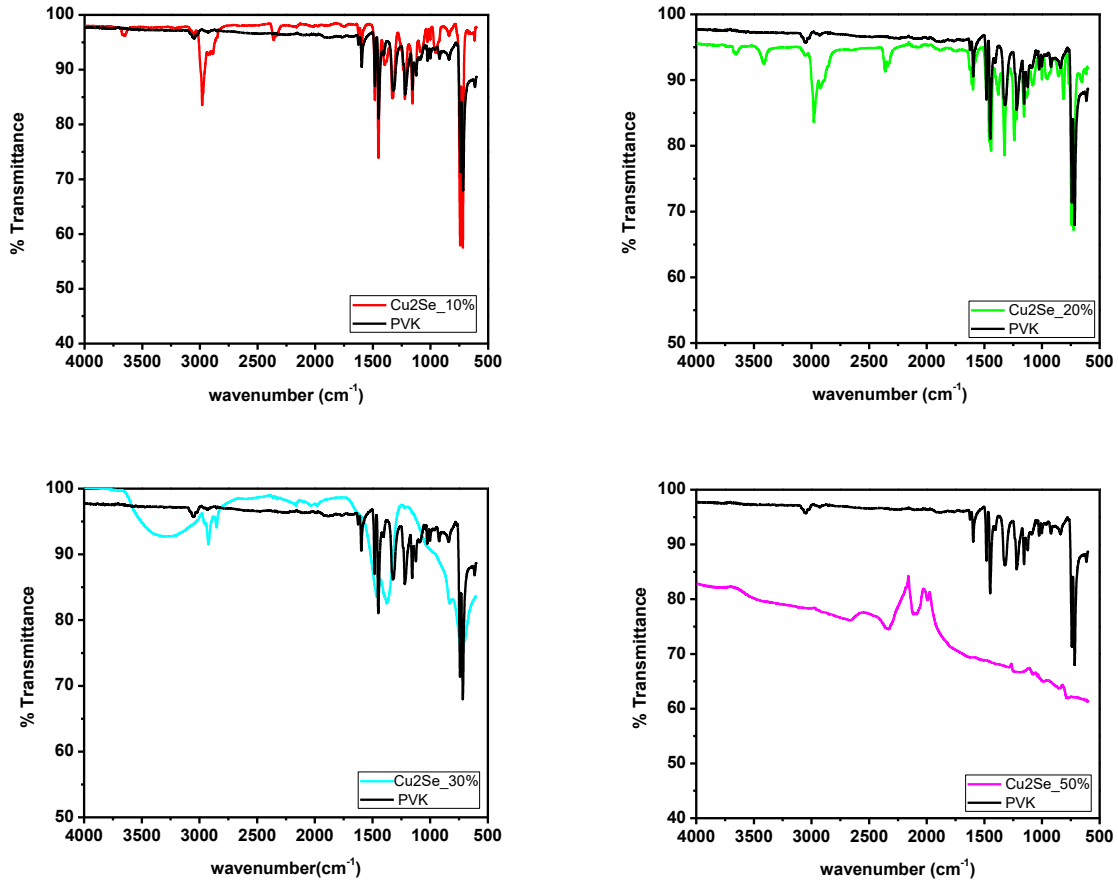

Fig. 4.1S: The IR spectrum of the varying weight percentages of Cu_2Se

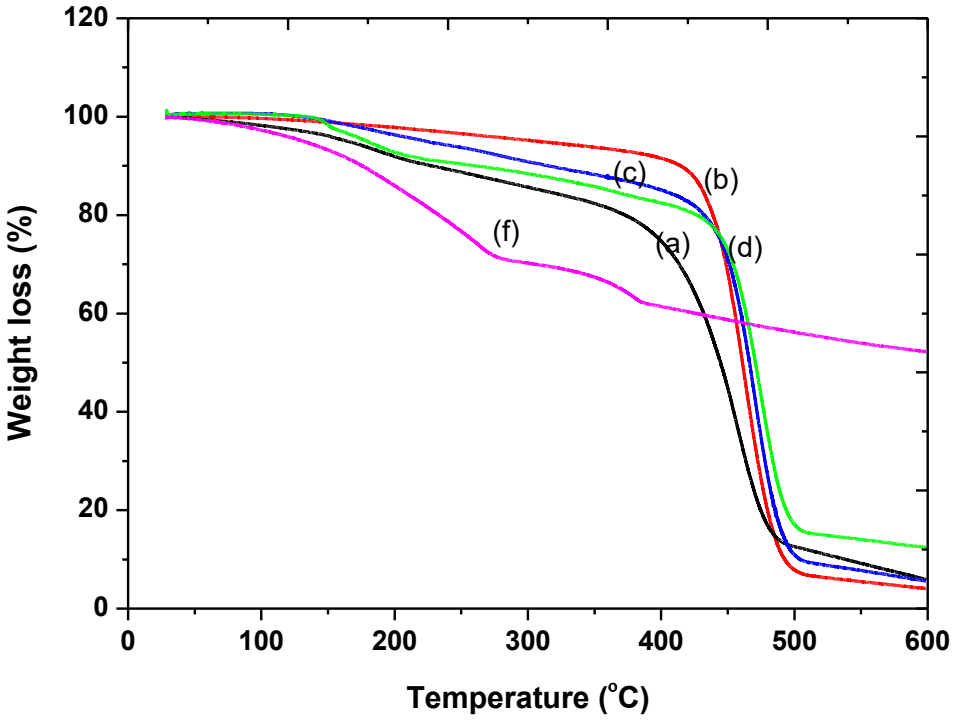

Fig. 4.2S: TGA graph of the different weight percentages of Cu_2Se, (a) PVK, (b) 10 %, (c) 20 %, (d) 30 % and (f) 50 % nanocomposites

The AFM image shows a smooth and even distribution of the hybrid film which has been spin coated on.

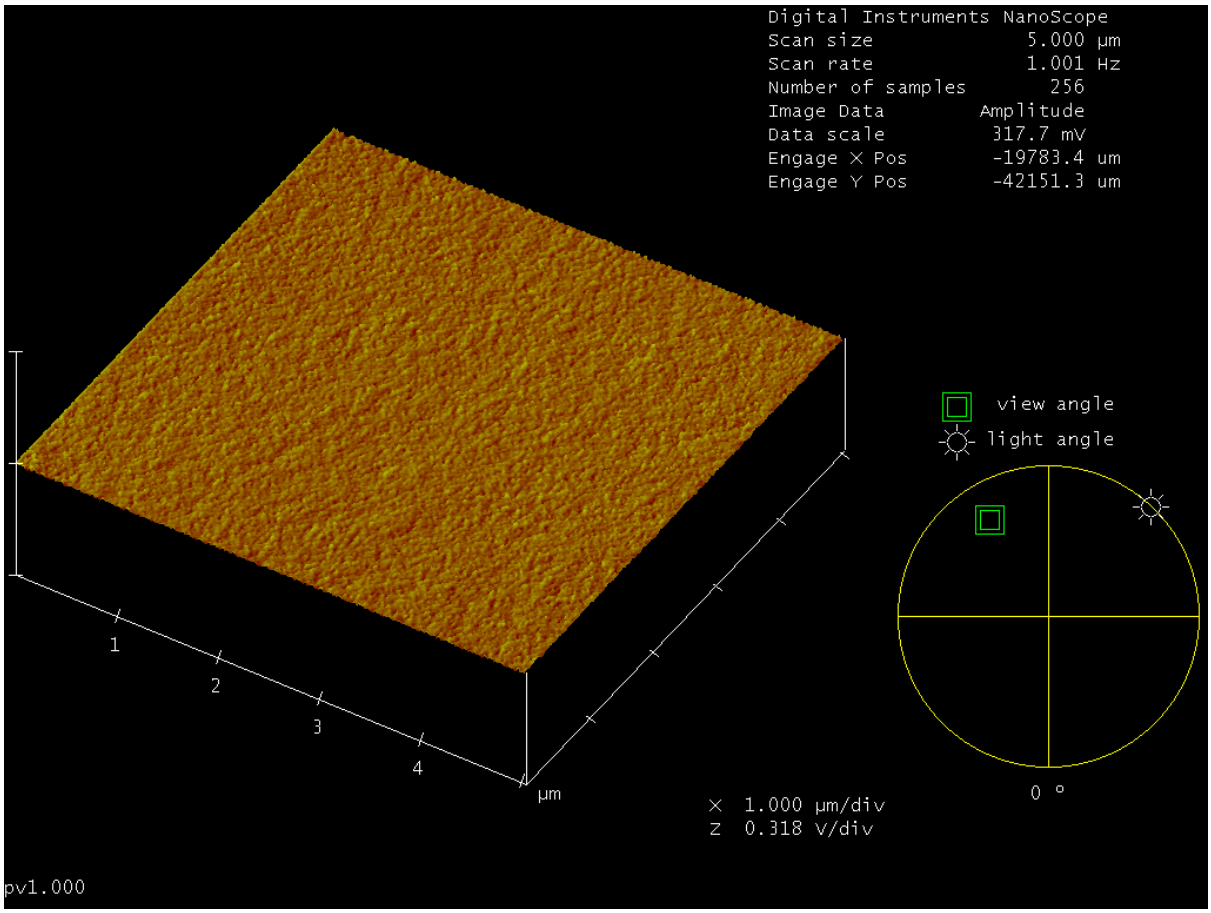

Fig. 4.8S: AFM image of spin coated hybrid material of solar cell

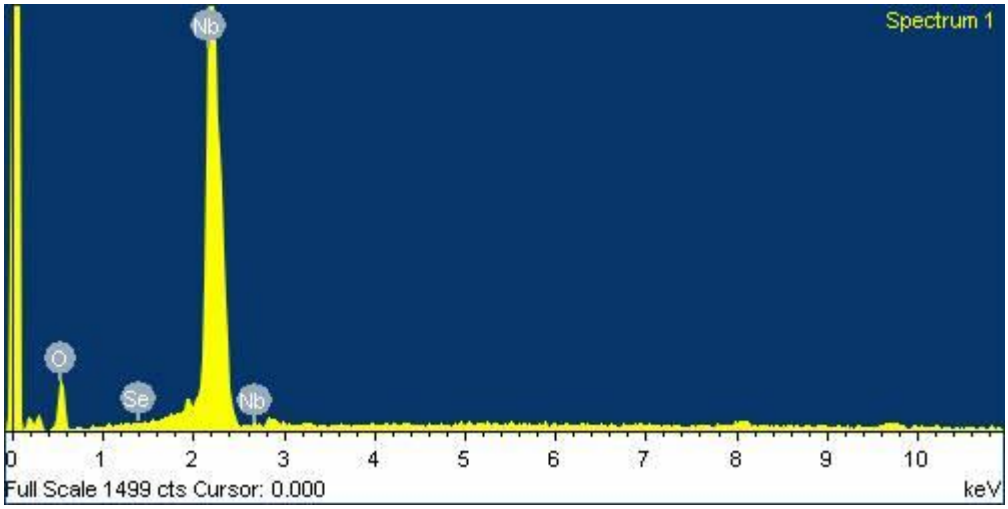

Fig. 5.1S: EDX spectrum of Niobium Selenide